Diss. ETH No. 16087

High–Temperature Series Expansions for Lattice Systems

A dissertation submitted to the

SWISS FEDERAL INSTITUTE OF TECHNOLOGY ZÜRICH
(ETH Zürich)

for the degree of
Doctor of Natural Science

presented by

MATHIAS KÖRNER

Dipl. Phys. ETH
born January 15, 1974
German citizen

accepted on the recommendation of
Prof. Dr. M. Troyer, examiner
Prof. Dr. M. Sigrist, co–examiner

2005

Seite Leer /
Blank leaf

Abstract

The aim of the first part of this thesis is to study strongly–correlated quantum lattice models arising in the description of the copper oxide superconductors with the help of high–temperature series expansions. After a review of the high–temperature series expansion and the methods of analytic continuation that we use to analyze the series, we first study a static nonmagnetic impurity in a quantum critical bilayer antiferromagnet. We examine how the high–temperature series of the susceptibility of a static nonmagnetic impurity can be calculated and determine the low–temperature effective spin of this impurity, which has been predicted to be fractionalized using field theoretical methods. The data obtained from the series expansion is compared to data from quantum Monte Carlo simulations, and both simulation methods yield a non–fractionalized value of the impurity spin. Next, the normal–state properties of the t–t'–J model are studied to gain a better understanding of the asymmetry of this model for different signs of the next–nearest neighbor hopping t', which corresponds to different types of doping experimentally. We confirm that a positive t' enhances the antiferromagnetism in the system and leads to a free electron–like Fermi–surface satisfying Luttingers theorem. A negative t' on the other hand suppresses antiferromagnetism and leads to a complex behavior that can be explained by the presence of a flat band in the dispersion.

In the second part of the thesis we apply techniques used in the construction of the high–temperature series expansion to combine cluster updates with multicanonical updates in the Monte Carlo simulation of continuous spin models. Combining both methods can reduce the critical slowing down of the multicanonical updates and we demonstrate this on two example system. The last part of this thesis studies the limiting form of the ground–state energy distribution of a spin glass. For mean–field spin glasses the limiting distribution is found to be non–Gaussian, while non–mean–field spin glasses are found to have a Gaussian limiting distribution.

Seite Leer /
Blank leaf

Kurzfassung

Das Ziel des ersten Teils dieser Dissertation is die Untersuchung stark korrelierter Quantensysteme auf Gittern, die in der Beschreibung der Kupferoxid Supraleiter vorkommen, mit Hilfe von Hochtemperaturreihenentwicklungen. Nach einem Überblick über die Hochtemperaturreihenentwicklung und die Methoden der analytischen Fortsetzung, die wir verwenden um die Reihen zu analysieren, studieren wir zuerst eine statische, nichtmagnetische Verunreinigung in einem quantenkritischen Zweischichten–Antiferromagneten. Wir untersuchen wie die Hochtemperaturreihe der Suszeptibilität einer solchen Verunreinigung berechnet werden kann und untersuchen das Tieftemperaturverhalten des effektiven Spins dieser Verunreinigung, für den mit Hilfe feldtheoretischer Methoden eine Fraktionalisierung vorhergesagt wurde. Wir vergleichen die Resultate der Reihenentwicklung mit Quanten Monte Carlo Simulationen und beide Simulationsmethoden ergeben einen nichtfraktionalisierten Wert für den effektiven Spin der Verunreinigung. Als nächstes untersuchen wir die Eigenschaften des t–t'–J Modells im Normalzustand, um ein besseres Verständnis der Asymetrie dieses Modelles bezüglich unterschiedlicher Vorzeichen von t', die experimentell unterschiedlichen Typen von Doping entsprechen, zu erreichen. Wir bestätigen, dass ein positives t' zum einen den Antiferromagnetismus verstärkt und zum anderen zu einer freien–Elektronen–artigen Fermifläche führt, die den Satz von Luttinger erfüllt. Auf der anderen Seite unterdrückt ein negatives t' den Antiferromagnetismus und führt zu einem komplexen Verhalten, das durch die Anwesenheit eines flachen Bandes in der Dispersion erklärt werden kann.

Im zweiten Teil der Dissertation wenden wir Techniken, die wir zur Konstruktion der Hochtemperaturreihe benutzten, an um Cluster Updates mit Multikanonischen Updates für die Monte Carlo Simulation von kontinuierlichen Spin Modellen zu kombinieren. Die Kombination beider Methoden führt zu einer Reduzierung der kritischen Verlangsamung, und wir illustrieren dies an zwei Beispielsystemen. Der letzte Teil dieser Dissertation untersucht die Grenzverteilung der Grundzustandsenergie eines Spinglases. Für mean–field Spingläser is diese Grenzwertverteilung eine nicht–Gausssche Verteilung und für nicht–mean–field Spingläser eine Gaussche Verteilung.

Contents

Chapter 1

Introduction

Brought into the spotlight by the discovery of superconductivity in the copper–oxide ceramic LaBaCuO at 30K by Bednorz and Müller in 1986 [1] — at that time a new record for the transition temperature of a superconductor — the study of strongly–correlated electron systems is today one of the most active fields in experimental and theoretical condensed–matter physics. The possible technical applications of superconductors with high transition temperatures quickly lead to a vast experimental and theoretical interest in these materials, and subsequently compounds with transition temperatures as high as 138K at room pressure were found [2]. As the materials are rather poor conductors in their normal state and are obtained by the chemical doping of insulators, it was discussed early that electron–phonon coupling cannot be the mechanism responsible for superconductivity in these materials. Instead Anderson proposed that the behavior of the cuprates can be explained by the doping of a Mott insulator [3]. Mobile holes destroy the long–range order of the antiferromagnetic ground state of the Mott insulator at half–filling and lead to a resonating valence–bond state, a state Anderson originally had in mind for the spin–1/2 antiferromagnet on a triangular lattice and which can be visualized as a state formed by a superposition of local spin singlets. As one of the main topics of the thesis is the study of models originating from these materials using high–temperature series expansions, we here give a brief overview over how these models arise in the description of the cuprates.

To understand why the cuprates are doped Mott insulators we start with their

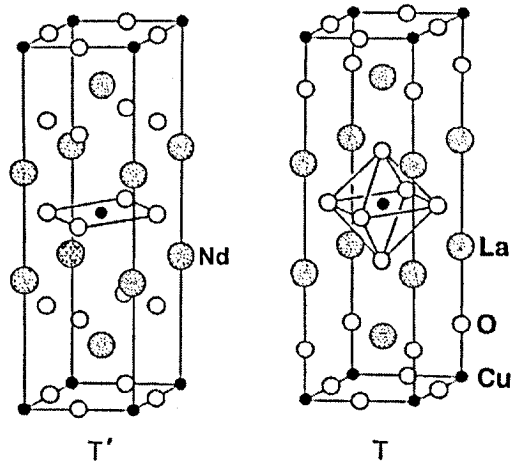

Figure 1.1: The crystal structure of the copper oxide parent compounds Nd_2CuO_4 (T') and La_2CuO_4 (T). The CuO_2 planes of the T' (T) phase can be doped with electrons (holes) by replacing Nd (La) with Ce (Sr). (adapted from Ref. [4])

crystal structure. A common feature of all cuprates is the presence of CuO_2 planes sandwiched by layers acting as a charge reservoir. Figure 1.1 shows the crystal structure of the insulating parent compounds Nd_2CuO_4 and La_2CuO_4. Both materials have a tetragonal crystal structure with single CuO_2 planes running in the so called *ab*–plane. Figure 1.2 shows the arrangement of the copper and oxygen atoms in such a CuO_2 plane. Taking into account the crystal–field splitting of the atomic orbitals one finds that a single CuO_2 plane can be described by a three–band Emery model [5], whose bands are due to the oxygen $2p_x$ and $2p_y$ orbitals and the $3d_{x^2-y^2}$ copper orbital. The parent compounds have two electrons in each of the oxygen $2p_{x,y}$ orbitals (filled band) and one electron in the copper $3d_{x^2-y^2}$ orbitals (half–filled band), so that band theory would predict for the materials to be metallic. However, a strong Coulomb repulsion between electrons in the $3d_{x^2-y^2}$ orbitals renders the electrons in the these orbitals immobile, and the materials become insulating. In terms of bands one speaks of the splitting of the $3d_{x^2-y^2}$ band into a lower and an upper Hubbard band. The lower Hubbard band is completely filled while the upper Hubbard band is empty and separated from the lower band by a gap leading to an insulating state. Such an insulating state is called a Mott insulator and its existence is an electron–electron interaction effect and cannot be understood by a band theory of independent electrons. A simple

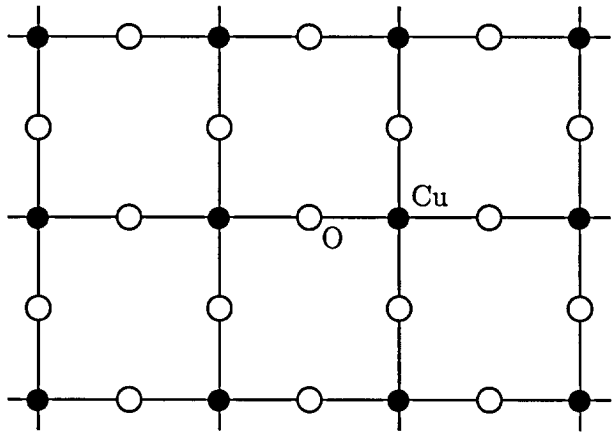

Figure 1.2: Arrangement of the copper and oxygen atoms in a single CuO_2 plane. A single plane can be described by a three–band Emery model, with two bands coming from the oxygen $2p_x$ and $2p_y$ orbitals and one band coming from the copper $3d_{x^2-y^2}$ orbital. The three–band Emery model can be reduced to a single–band Hubbard or t–J model on the square lattice formed by the copper atoms for electron– and hole–doped materials.

model for a Mott insulator that can be obtained as an effective Hamiltonian of the three–band Emery model in the case of electron– and hole–doping [6] is the single–band Hubbard model on the square lattice formed by the copper atoms with the Hamiltonian

$$H = -t \sum_{\langle ij \rangle, \sigma} \left(c^\dagger_{i\sigma} c_{j\sigma} + c^\dagger_{j\sigma} c_{i\sigma} \right) + U \sum_i n_{i\uparrow} n_{i\downarrow}. \tag{1.1}$$

$c^\dagger_{i\sigma}$ is an electron creation operator, $n_{i\sigma} = c^\dagger_{i\sigma} c_{i\sigma}$ the corresponding number operator, and the sums are over the nearest neighbors $\langle ij \rangle$ and the sites i of the square lattice. The first part of the Hamiltonian is the kinetic energy of a tight–binding model of electrons on the square lattice and the second a simplification of the Coulomb repulsion between electrons to an on–site repulsion U between two electrons on the same site. Because most cuprates are charge transfer insulators, the validity of such a single–band Hubbard model for a CuO_2 plane doped with holes is far from trivial. Holes are not doped onto the copper sites but instead into the $2p_{x,y}$ orbitals of the oxygens. Zhang and Rice [7] were able to show that a hole doped into an oxygen orbital spreads onto the four oxygen atoms surrounding a copper atom and forms a singlet with the electron in the copper $3d_{x^2-y^2}$

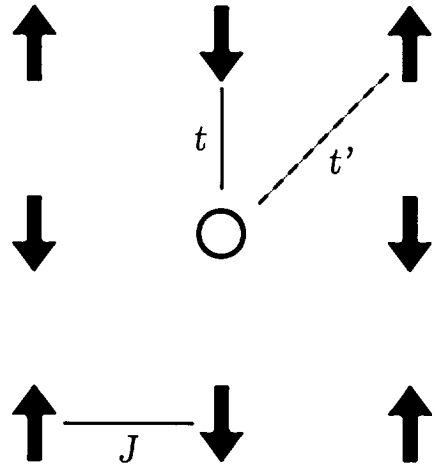

Figure 1.3: Sketch of the hopping (t, t') and antiferromagnetic (J) exchange processes for the t–t'–J model on a square lattice.

orbital, and the movement of this Zhang–Rice singlet from copper atom to copper atom can then be described by a single–band Hubbard model on a square lattice. Typical physical parameter values for hole– and electron–doped cuprates are $t = \pm 400\text{meV}$ and $U = 4\text{eV}$. Assuming that a single–band Hubbard model is a valid description of the CuO_2 planes in the cuprates and taking into account the order of magnitude of the parameters, we see that the relevant region for the cuprates is the strong–coupling limit of the Hubbard model, defined by $U \gg t$. In this limit and at low temperatures doubly occupied sites are unlikely to occur due to the strong on–site repulsion, and we can derive an effective Hamiltonian for the Hubbard model in a basis given by the states $|0\rangle$, $|\uparrow\rangle$, and $|\downarrow\rangle$. The resulting Hamiltonian is the t–J model [8]

$$H_{tJ} = -t \sum_{\langle ij \rangle, \sigma} \mathcal{P} \left(c^\dagger_{i\sigma} c_{j\sigma} + c^\dagger_{j\sigma} c_{i\sigma} \right) \mathcal{P} + J \sum_{\langle ij \rangle} \mathbf{S}_i \cdot \mathbf{S}_j, \tag{1.2}$$

where $c^\dagger_{i\sigma}$ is an electron creation operator, $\mathbf{S}_i$ an electron spin operator, $\mathcal{P} = \prod_i (1 - n_{i\uparrow} n_{i\downarrow})$ a projection operator removing all states with doubly occupied sites, and $J = t^2/U$ an effective antiferromagnetic exchange between the electrons coming from second–order hopping processes via an occupied site in the Hubbard model (for a derivation see for example the book of Fazekas [9]). In Eq. (1.2) we have neglected a nearest neighbor density–density interaction and a three–site next–nearest neighbor hopping term, whose relevance for the physical model

are still an unresolved subject. First principles calculations using the three–band Emery model also indicate that a direct next–nearest neighbor hopping is significant for the cuprates leading to the t–t'–J model

$$H_{tt'J} = H_{tJ} - t' \sum_{\langle\langle ik \rangle\rangle, \sigma} \mathcal{P} \left(c^\dagger_{i\sigma} c_{k\sigma} + c^\dagger_{k\sigma} c_{i\sigma} \right) \mathcal{P}, \tag{1.3}$$

where $\langle\langle ik \rangle\rangle$ denotes next–nearest neighbor sites and t' is typically of the same order as J as shown by Hybertsen *et al.* [6]. A sketch of all processes occurring in the t–t'–J model is shown in Fig. 1.3. At half–filling (one electron per site) the t–t'–J model simplifies to a spin–1/2 Heisenberg antiferromagnet on a square lattice [10] with the Hamiltonian

$$H_{AFM} = J \sum_{\langle ij \rangle} \mathbf{S}_i \cdot \mathbf{S}_j. \tag{1.4}$$

Figure 1.4 shows the combined experimental phase diagram of electron– and hole–doped cuprates as a function of the temperature and the doping. As expected both types of materials are antiferromagnets at half–filling, the finite Neel temperature coming from a weak interlayer coupling between different CuO_2 planes. Chemical doping of the system destroys the antiferromagnetic order and superconductivity sets in close to the point where the antiferromagnetic order vanishes. Except for these basic facts the phase diagram is strongly asymmetric with respect to electron– and hole–doping. While the metallic phase of the electron–doped cuprates shows robust antiferromagnetism and seems to be well described by Fermi–liquid theory, the corresponding phase of the hole–doped compounds already shows unusual behavior in the normal state. At optimal doping the resistivity is proportional to T instead of T^2 for a wide range of temperatures as predicted by Fermi–liquid theory, thus questioning the applicability of Fermi–liquid theory to the hole–doped materials [8]. Furthermore there is a temperature scale T^* — the pseudogap temperature — below which *some* of the excitations in the Brillouin zone are gapped [12]. Understanding the phase diagram of the Hubbard and the t–t'–J model is therefore an essential step in understanding the cuprates and in particular the asymmetry of the phase diagram.

Unfortunately, the Hubbard and the t–t'–J model away from half–filling are difficult to examine using analytical and computational methods. Monte Carlo simulations of these models at finite doping suffer from the sign–problem [8] due to the fermionic nature of the charge carriers so that only small system sizes

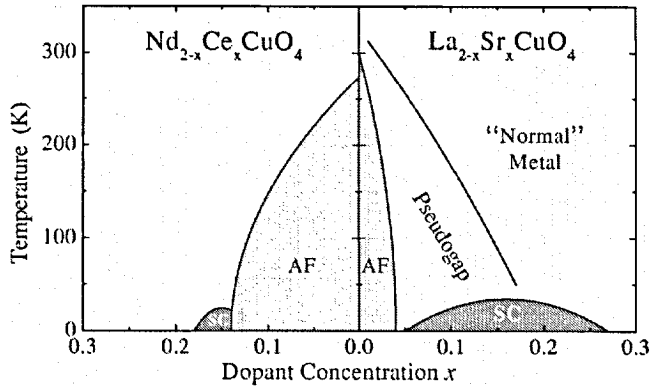

Figure 1.4: Combined phase diagram of electron– ($Nd_{2-x}Ce_xCuO_4$) and hole–doped ($La_{2-x}Sr_xCuO_4$) cuprates as a function of the doping (from Ref. [11]). Though similar in some aspects, the phase diagram is asymmetric with respect to electron– and hole–doping.

can be studied at moderate temperatures. Ground–state expansions [13] on the other hand do not have a well defined state to expand around if a finite density of charge carriers is present, and the density matrix renormalization group has only been applied to the one–dimensional versions of the models with success. Therefore other methods such as dynamical mean–field theory, exact diagonalizations, variational Monte Carlo simulations and high–temperature series expansions have been used to study these models. A somewhat older review of calculations for the t–J model is available in Ref. [8] and a more recent review of the Hubbard model can be found in Ref. [14].

In this thesis we use the high–temperature series expansion to study two models related to the cuprates. The high–temperature series expansion is an unbiased simulation method that does not suffer from the negative–sign problem occurring in Monte Carlo simulations of fermionic models. Its disadvantages are that phases with a broken symmetry are not accessible to the method and that the computational effort of a calculation grows exponentially with the desired order of the expansion. Also high–temperature series have to be analytically continued using approximants to extract information. The method has been applied with success to a wide range of classical and quantum mechanical systems, among them the Heisenberg antiferromagnet (see for example Ref. [15]) and the t–J model (see Ref. [16, 17, 18, 19, 20, 21, 22, 23]).

In chapter 2 we first present a brief derivation of the high–temperature series expansion, and we discuss approximants as a tool to perform an analytic continuation of a high–temperature series in chapter 3. In chapter 4 we use the high–temperature series expansion to study the susceptibility of an impurity in a bilayer antiferromagnet, an extension of the square–lattice antiferromagnet defined in Eq. (1.4), and compare the results to data obtained from quantum Monte Carlo simulations. We then apply the high–temperature series expansion to the t–t'–J model in chapter 5. Our aim is to achieve a better understanding of the effects of the next–nearest neighbor hopping term, a problem that has not been approached before using high–temperature series expansions. We thereby focus on the magnetic structure factor $S(\mathbf{q})$ and the momentum distribution function $n(\mathbf{q})$ of the model. Chapter 6 discusses the combination of multicanonical simulations and cluster algorithms for classical spin models using techniques developed in chapter 2 and chapter 7 contains the results of a study of the the ground–state energy distribution in a spin–glass, a problem not directly related to the physics of the cuprates.

Seite Leer /
Blank leaf

Chapter 2

High–temperature series expansion

High–temperature series expansions are one of the computational methods available to study quantum systems on a lattice, such as the Heisenberg, the Hubbard, or the t–J model introduced in chapter 1. The aim of a high–temperature series expansion is to calculate the power series

$$P(\beta) = \sum_{i=0}^{N} c_P(i)\,\beta^i \tag{2.1}$$

of a thermodynamic property $P(\beta)$ in the inverse temperature $\beta = 1/k_B T$ up to a chosen order N. Different methods to calculate a high–temperature series expansion exist and the goal of the first methods that were developed was to facilitate or simplify the manual calculation of Eq. (2.1). An overview over a number of these early methods with their application can be found in Ref. [24]. The availability of computers profoundly changed the approach to high–temperature series expansions and series expansions in general, and todays methods are tailored for a straightforward implementation on a computer. A series expansion method that is well suited for a computer implementation and that can be used for different types of expansions is the *connected–cluster expansion*. In this chapter we demonstrate how it can be used to calculate a high–temperature series expansion and examine the requirements that a thermodynamic property has to satisfy so that the connected–cluster expansion can be applied. Because we use the connected–cluster expansion only in the context of high–temperature se-

ries expansions, we will use the names synonymously. A thorough review of the connected–cluster expansion in the context of ground–state or $T = 0$ expansions can be found in Ref. [13].

High–temperature series expansions can conveniently be represented by graphs and their extensions such as multigraphs (graphs that can have more than one edge between two vertices) and hypergraphs (graphs whose edges can connect more than two vertices). An overview over the concepts and also the notation used in this thesis can be found in the book by Diestel [25].

2.1 Quantum–lattice models

The Heisenberg, the Hubbard, and the t–J model are *quantum–lattice models*. They are defined on a lattice of sites that can be identified by numbers $i \in \mathbb{N}$, and each of the sites has a fixed position and is associated with a finite dimensional Hilbert space. The Hamiltonian

$$H = \sum_i H_i + \sum_{ij} H_{ij} + \sum_{ijk} H_{ijk} + \cdots \tag{2.2}$$

is a sum of terms that only involve a finite number of sites in the system. In condensed–matter physics such models typically arise when the real–space Schrödinger equation for electrons is simplified by the use of localized Wannier orbitals for the electrons. In the canonical ensemble, thermodynamic properties can be defined with the help of the density matrix [26]

$$\hat{\rho}\left(\beta\right) = \exp\left(-\beta H\right), \tag{2.3}$$

where $\beta = 1/T$ is the inverse temperature, and we have set Boltzmann's constant k_B to one. In the grand–canonical ensemble the density matrix in addition contains the chemical potential coupled to the number of particles in the system. The value of the chemical potential then determines the the average number of particles in the system. As the presence of the chemical potential in the grand–canonical ensemble does not change the derivation of the connected–cluster expansion as a high–temperature series expansion, we assume without any loss of generality that our system can be described in the canonical ensemble in this

chapter. Using the density matrix the thermodynamic average of an operator A is defined by

$$\langle A \rangle = \frac{\mathrm{Tr}\left[A \cdot \hat{\rho}(\beta)\right]}{Z(\beta)}, \tag{2.4}$$

where

$$Z(\beta) = \mathrm{Tr}\left[\hat{\rho}(\beta)\right] \tag{2.5}$$

is the partition function of the system. The traces in Eq. (2.4) and Eq. (2.5) are over all states of the systems Hilbert space. The free energy of the system is given by

$$F(\beta) = -\frac{\log Z(\beta)}{\beta}. \tag{2.6}$$

Often the log–partition function

$$\mathcal{L}(\beta) = \log Z(\beta) \tag{2.7}$$

is more convenient to use than the free energy, as it is nonsingular for $\beta \to 0$. Using an auxiliary field ϕ and the substitution $H \to H - \phi A$ in the definition of the density matrix, the thermodynamic average of an operator A as defined in Eq. (2.4) can also be written as

$$\langle A \rangle = \beta^{-1} \left. \frac{\partial \mathcal{L}(\beta, \phi)}{\partial \phi} \right|_{\phi=0}. \tag{2.8}$$

To simplify our presentation we now assume that the Hamiltonian of the quantum lattice model has only identical two–site interactions H_{ij}. An example of such a model is the spin–1/2 Heisenberg antiferromagnet on a square lattice introduced in chapter 1. The Hamiltonian

$$H = J \sum_{\langle ij \rangle} \mathbf{S}_i \cdot \mathbf{S}_j, \tag{2.9}$$

has a local site basis given by $\{|\uparrow\rangle, |\downarrow\rangle\}$, $\mathbf{S}_i$ is a spin–1/2 operator at site i of the lattice, and the sum is over all nearest neighbor sites $\langle ij \rangle$ of the square lattice. Examples for thermodynamic properties are the internal energy $U = \langle H \rangle$, the specific heat $C_V = \beta^2 \left(\langle H^2 \rangle - \langle H \rangle^2\right)$, and the uniform susceptibility $\chi = \beta \left(\langle M^2 \rangle - \langle M \rangle^2\right)$ with $M = \sum_i S_i^z$.

To define the square lattice Heisenberg Hamiltonian it is not sufficient to specify the positions of the spins in the lattice and the interaction term. In addition we

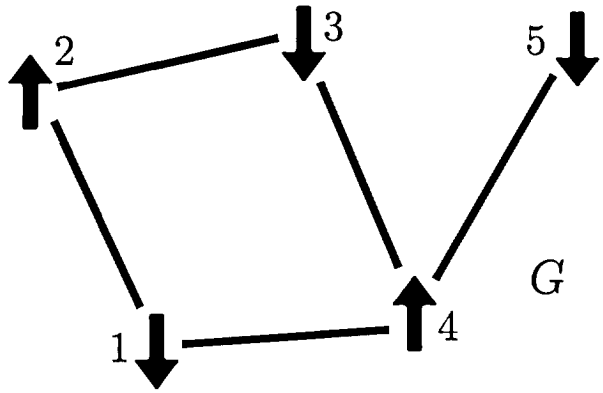

Figure 2.1: Heisenberg antiferromagnet defined on a graph G. Each vertex of G represents a spin and each edge an antiferromagnetic exchange term between the spins connected by the edge.

have to specify which spins interact — such as all nearest nearest neighbor spins $\langle ij \rangle$ in the case of Eq. (2.9) — and it is convenient to encode the information on which spins interact via H_{ij} with a graph G. We define the model on the graph G by the Hamiltonian

$$H_G = \sum_{ij \in G} H_{ij}. \tag{2.10}$$

Each vertex of the graph G corresponds to a site of the system and each edge to an exchange term H_{ij} of the Hamiltonian. We refer to the infinite graph of a quantum lattice model whose vertices are on the sites of a lattice and whose edges represent all interactions in the model via Eq. (2.10) as the lattice graph of the model. Note that models defined on the same lattice such as the square lattice may result in different lattice graphs as different sites of the lattice can interact. Thus we can speak of the spin–1/2 Heisenberg antiferromagnet on a graph G as illustrated in Fig. 2.1 by using

$$H_G = J \sum_{ij \in G} \mathbf{S}_i \cdot \mathbf{S}_j. \tag{2.11}$$

2.2 Connected–cluster expansion

Before presenting a detailed construction of the connected–cluster expansion we briefly summarize the central result: If a connected–cluster expansion for a prop-

erty $P_G(\beta)$ for a quantum–lattice model on a finite graph G exists — we later discuss the requirements that $P_G(\beta)$ has to satisfy — then $P_G(\beta)$ can be written as

$$P_G(\beta) = \sum_{C \subseteq G,\, C \text{ connected}} W_P(C, \beta), \tag{2.12}$$

where the sum is over all distinct *connected* subgraphs C of G. The weight $W_P(C, \beta)$ of a graph, sometimes also referred to as a cluster, C is a polynomial in the inverse temperature β whose lowest order term is $\beta^{||C||}$, where $||C|| = |E(C)|$ is the number of edges in C, and only depends on C but not on G. Thus only the weights of connected clusters with N edges or less have to be calculated to obtain $P_G(\beta)$ to order β^N and as we will later see also the thermodynamic limit of $P(\beta)$ on a lattice graph to order N. If the property P_G only depends on the shape of the graph G then Eq. (2.12) can be simplified to

$$P_G(\beta) = \sum_{C \subseteq G,\, C \text{ connected}} (C \cdot G)\, W_P(C, \beta), \tag{2.13}$$

where the sum is over all different shapes of C that can be embedded into G and $(C \cdot G)$ counts the number of times C can be embedded into G. Figure 2.4 is an illustration of the different viewpoints of Eq. (2.12) and Eq. (2.13). The weights themselves are calculated by inverting Eq. (2.12) to

$$W_P(G, \beta) = P_G(\beta) - \sum_{C \subset G,\, C \text{ connected}} W_P(C, \beta). \tag{2.14}$$

Starting with the smallest clusters and progressively going to larger clusters all weights can be constructed using Eq. (2.14).

2.2.1 Construction of the connected–cluster expansion

We now present a detailed construction of the connected–cluster expansion of a thermodynamic property P_G of a quantum–lattice model on a graph as defined by the Hamiltonian in Eq. (2.10). The construction is based on a multivariable series expansion of the property $P_G(\beta)$ in formal expansion variables x_{ij} assigned to the edges ij of the graph G. The expansion variables allow us to assign the terms of the expansion to different subgraphs of G. $P_G(\beta)$ is a function of the density matrix $\hat{\rho}_G(\beta)$ and we replace βH_G by

$$\beta H_G \to \sum_{ij \in G} x_{ij} H_{ij} \tag{2.15}$$

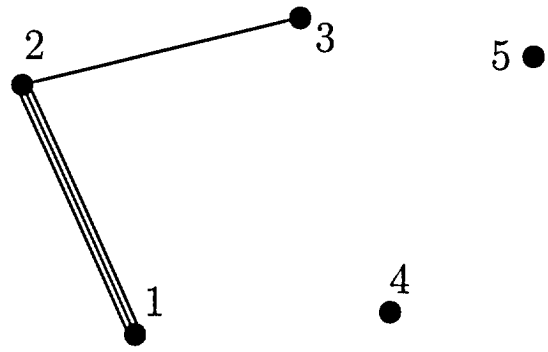

Figure 2.2: Multigraph representing a term $[n_{ij}]$ of the multivariable series expansion as described in the text. The vertices 4 and 5 may be dropped as they do not belong to the subgraph induced by $[n_{ij}]$.

in the definition of the density matrix in Eq. (2.3). We call such an assignment of variables or numbers to the edges a *labeling* of the edges and write $[x_{ij}]_G$. The subscript G can be dropped if the graph that is labeled is obvious from the context. By setting $[x_{ij}] = \beta$ at any point in the calculation we can recover the thermodynamic value of $P_G(\beta)$ and doing so at a later stage allows us to rearrange the terms of the series in a useful way. Using the substitution in Eq. (2.15) the density matrix and the property P_G become functions of the $[x_{ij}]$. Expanding $P_G([x_{ij}])$ in a multivariable series we obtain

$$P_G([x_{ij}]) = \sum_{[n_{ij}]\geq 0} c_{P,[n_{ij}]} \prod_{ij\in G} (x_{ij})^{n_{ij}}\,, \tag{2.16}$$

where $[n_{ij}] \geq 0$ denotes all integer labelings of the edges of G so that $n_{ij} \geq 0$ for all $ij \in G$. The coefficients $c_{P,[n_{ij}]}$ are explicitly given by

$$c_{P,[n_{ij}]} = \left(\prod_{ij\in G} \frac{1}{n_{ij}!} \left(\frac{\partial}{\partial x_{ij}} \right)^{n_{ij}} \right) P_G([x_{ij}]) \Bigg|_{x_{ij}=0}\,. \tag{2.17}$$

Each integer labeling $[n_{ij}]$, its coefficient $c_{P,[n_{ij}]}$, or term $c_{P,[n_{ij}]} \prod (x_{ij})^{n_{ij}}$ can be visualized as a multigraph by drawing n_{ij} edges between vertex i and j as shown in Fig. 2.2. An integer labeling $[n_{ij}]_G$ induces a subgraph G' of G by taking all edges with $n_{ij} > 0$ and removing all isolated vertices. Taking the corresponding $[n_{ij}]_G$ for the edges in G' also induces natural labeling $[n_{ij}]_{G'} > 0$ of G'. P_G has to satisfy two requirements so that a connected–cluster expansion can be constructed:

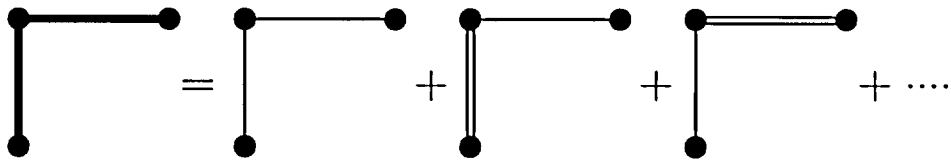

Figure 2.3: Graphic representation of the weight of a cluster C as defined in Eq. (2.21) as the sum over multigraphs that induce C.

1. The coefficient $c_{P,[n_{ij}]}$ defined in Eq. (2.17) may only depend on the subgraph G' and the labeling $[n_{ij}]_{G'}$ induced by $[n_{ij}]_G$, with the exception of $[0]_G$, which is a special case that induces the empty graph (for the moment we assume that $c_{P,[0]_G} = 0$ and later discuss the case $c_{P,[0]_G} \neq 0$). Then $c_{P,[n_{ij}]}$ is independent of the graph G in whose expansion it occurs, and once calculated for one graph it can be used in the expansion of other graphs.

2. $c_{P,[n_{ij}]}$ has to be zero if the induced subgraph G' has more than one connected component. This leads to an expansion of P_G in terms of connected subgraphs of G.

While the first requirement can be checked directly for a given property, a sufficient condition is that for any subgraph G' of G

$$P_G([x_{ij}]_G)|_{x_{ij}=0 \text{ if } ij \notin G'} = P_{G'}([x_{ij}]_{G'}). \tag{2.18}$$

Removing the edge from the density matrix removes any contribution of the edge to the property. To see that Eq. (2.18) is sufficient, we assume that we are given an integer labeling $[n_{ij}]_G$ with an induced subgraph C, and set G' in Eq. (2.18) equal to C. Then $c_{P,[n_{ij}]}$ is a coefficient of the series expansion of $P_C([x_{ij}]_C)$ and can thus only depend on the induced subgraph C. While this property is seldom mentioned it is essential if we want to reuse the expansion coefficients of a small graph for a larger one.

We now turn our attention to the second requirement: $c_{P,[n_{ij}]}$ has to be zero if the subgraph induced by $[n_{ij}]$ has more than one connected component. A sufficient condition on P_G is that for two disconnected graphs G_1 and G_2

$$P_{G_1 \cup G_2}(\beta) = P_{G_1}(\beta) + P_{G_2}(\beta). \tag{2.19}$$

Assume that the induced subgraph C of $[n_{ij}]_G$ consists of two disconnected graphs C_1 and C_2. Using the definition of $c_{P,[n_{ij}]}$ in Eq. (2.17) for

$$P_{C_1 \cup C_2}([x_{ij}]_{C_1 \cup C_2}) = P_{C_1}([x_{ij}]_{C_1}) + P_{C_2}([x_{ij}]_{C_2}). \tag{2.20}$$

and the fact that at least one partial derivative is taken for each x_{ij} of the induced subgraph $C_1 \cup C_2$, we see that $c_{P,[n_{ij}]}$ has to be zero, as derivatives of $P_{C_1}([x_{ij}]_{C_1})$ with respect to $x_{ij} \in C_2$ and derivatives of $P_{C_2}([x_{ij}]_{C_2})$ with respect to $x_{ij} \in C_1$ are taken on the right hand side of Eq. (2.20). Therefore only terms that have induced subgraphs which are connected have to be considered, giving the expansion method its name. Equation (2.19) is sometimes referred to as P being extensive but also holds for physically nonextensive quantities such as two–point correlation functions.

While it is possible to perform a high–temperature series expansion using the connected multigraphs associated with the $c_{P,[n_{ij}]}$, it is convenient to group the terms of Eq. (2.16) into weights assigned to the induced subgraphs. The weight $W_P(C, \beta)$ of a subgraph C of G is the sum of all terms in Eq. (2.16) for which the subgraph induced by $[n_{ij}]$ is equal to C with all x_{ij} set equal to β. Writing $[n_{ij}] \rightarrow C$ for a $[n_{ij}]$ whose induced subgraph is equal to C the weight of a graph C is given by

$$W_P(C, \beta) = \sum_{[n_{ij}] \rightarrow C} c_{P,[n_{ij}]} \prod_{ij \in C} \beta^{n_{ij}}. \tag{2.21}$$

By construction the weight is independent of G and zero if C has two or more connected components. Equation (2.21) is graphically represented in Fig. 2.3. It uniquely assigns each of the terms of the multivariable expansion in Eq. (2.16) to a subgraph of G so that $P_G(\beta)$ can be written as

$$P_G(\beta) = \sum_{C \subseteq G,\ C \text{ connected}} W_P(C, \beta). \tag{2.22}$$

The weight defined by Eq. (2.21) has the following properties: By construction it is a polynomial in β whose lowest order contribution is of order $\beta^{\|C\|}$, because each edge $ij \in C$ has $n_{ij} \geq 1$ and thus contributes at least linearly in β. Furthermore the weight of a disconnected subgraph is zero by construction. To calculate the high–temperature series of $P_G(\beta)$ to order β^N with a connected–cluster expansion, it is thus sufficient to calculate the weights of all connected subgraphs of G with N edges or less.

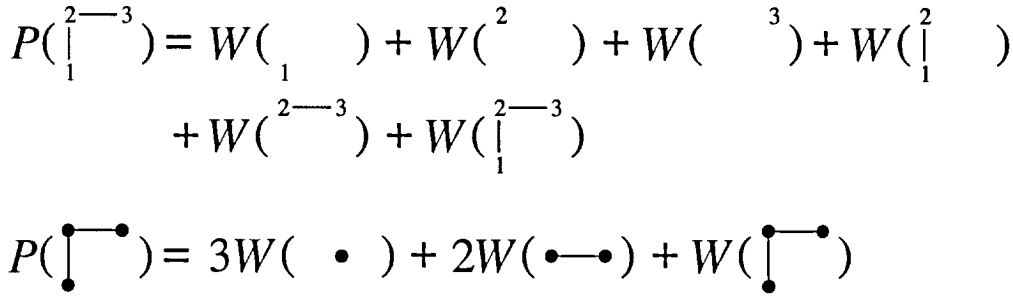

Figure 2.4: Property represented as a sum of labeled subgraphs as in Eq. (2.22) and as a sum of unlabeled subgraphs as in Eq. (2.23).

In Eq. (2.22) each connected subgraph C of G is uniquely defined by its location on G. Many properties and their weights will only depend on the shape of G and the subgraph C. Writing $(C \cdot G)$ for the number of times C can be embedded into G Eq. (2.22) simplifies to

$$P_G(\beta) = \sum_{C \subseteq G,\, C \text{ connected}} (C \cdot G)\, W_P(C, \beta). \tag{2.23}$$

Figure 2.4 shows a graphical representation of Eq. (2.22) and Eq. (2.23). The weight of a graph can be calculated by inverting Eq. (2.23) to

$$W_P(C, \beta) = P_C(\beta) - \sum_{C' \subset C,\, C \text{ connected}} (C' \cdot C)\, W_P(C', \beta). \tag{2.24}$$

Starting with small graphs and progressively going to larger graphs, we can calculate all the weights required for a particular calculation. Before we discuss the thermodynamic limit we briefly return to the case of an induced empty graph. Using Eqn. (2.19) for a quantity that is translationally invariant we obtain that

$$c_{P,[0]} = |G|\, P_S(\beta), \tag{2.25}$$

where $P_S(\beta)$ is the quantity calculated for a single site. Therefore we can simply include the isolated site as a connected subgraph of G with weight $W(S, \beta) = P_S(\beta)$ as done in Fig. 2.4.

2.2.2 The thermodynamic limit

We now take the thermodynamic limit of Eq. (2.23) for a physically extensive quantity with a connected-cluster expansion on a d dimensional lattice L. Let

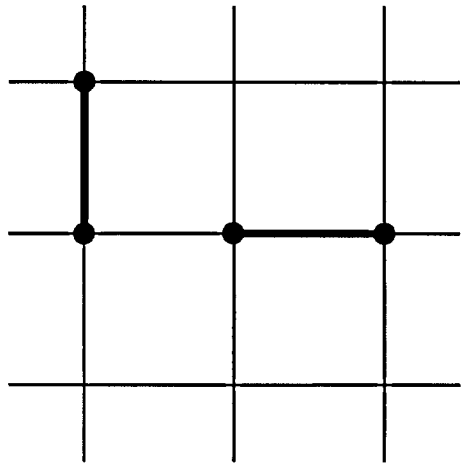

Figure 2.5: The two inequivalent embeddings of a single bond in the square lattice.

G_l be a connected subgraph of the lattice L that contains all sites of the lattice L within a volume l^d. Then the density of P

$$p(\beta) = \lim_{l\to\infty} \frac{P_{G_l}(\beta)}{|G_l|} \tag{2.26}$$

is given by

$$p(\beta) = \sum_{C\subset L,\, C \text{ connected}} L(C)\, W_P(C,\beta), \tag{2.27}$$

where

$$L(C) = \lim_{l\to\infty} \frac{(C\cdot G_l)}{|G_l|} \tag{2.28}$$

is the number of times the graph C can be embedded into the lattice *per site*. Figure 2.5 shows the two inequivalent embeddings of the graph with exactly one edge into the square lattice. Because to a given order only connected graphs with a limited number of edges contribute, Eq. (2.27) is free of any finite–size effects and therefore the connected–cluster expansion allows us to calculate the high–temperature series of a physical property in the thermodynamic limit without any additional extrapolation.

2.2.3 Steps of a calculation

Using the connected–cluster expansion, we now illustrate its application with the calculation of the of the log–partition function $\mathcal{L}(\beta)$ of the spin–1/2 Heisenberg antiferromagnet on a square lattice to order three. The calculation of the high–temperature series expansion is done in the following steps:

1. Determine all connected graphs G that can be embedded into the square lattice with $\|G\| \leq 3$. They are: $\cdot$, $-$, $\wedge$, $\sqcap$, and $\perp$.

2. Calculate $\mathcal{L}(\beta)$ to order β^3 for these graphs:

$$\begin{aligned}
\mathcal{L}_{\cdot}(\beta) &= \log(2) \\
\mathcal{L}_{-}(\beta) &= 2\log(2) + \frac{3J^2}{32}\beta^2 + \frac{J^3}{64}\beta^3 \\
\mathcal{L}_{\wedge}(\beta) &= 3\log(2) + \frac{3J^2}{16}\beta^2 + \frac{J^3}{32}\beta^3 \\
\mathcal{L}_{\sqcap}(\beta) &= 4\log(2) + \frac{9J^2}{32}\beta^2 + \frac{3J^3}{64}\beta^3 \\
\mathcal{L}_{\perp}(\beta) &= 4\log(2) + \frac{9J^2}{32}\beta^2 + \frac{3J^3}{64}\beta^3
\end{aligned}$$

3. Calculate the subclustercounts $(C' \cdot C)$. The only nonzero entries are $(\cdot\cdot G) = |G|$, $(- \cdot G) = \|G\|$, $(\wedge \cdot \sqcap) = 2$, and $(\wedge \cdot \perp) = 3$.

4. Calculate the weights $W_{\mathcal{L}}(G, \beta)$ for all graphs using Eq. (2.24):

$$\begin{aligned}
W_{\mathcal{L}}(\cdot, \beta) &= \mathcal{L}_{\cdot}(\beta) \\
W_{\mathcal{L}}(-, \beta) &= \mathcal{L}_{-}(\beta) - 2\,W_{\mathcal{L}}(\cdot, \beta) \\
W_{\mathcal{L}}(\wedge, \beta) &= \mathcal{L}_{\wedge}(\beta) - 3\,W_{\mathcal{L}}(\cdot, \beta) - 2\,W_{\mathcal{L}}(-, \beta) \\
W_{\mathcal{L}}(\sqcap, \beta) &= \mathcal{L}_{\sqcap}(\beta) - 4\,W_{\mathcal{L}}(\cdot, \beta) - 3\,W_{\mathcal{L}}(-, \beta) - 2\,W_{\mathcal{L}}(\wedge, \beta) \\
W_{\mathcal{L}}(\perp, \beta) &= \mathcal{L}_{\perp}(\beta) - 4\,W_{\mathcal{L}}(\cdot, \beta) - 3\,W_{\mathcal{L}}(-, \beta) - 3\,W_{\mathcal{L}}(\wedge, \beta)
\end{aligned}$$

5. Calculate the lattice counts $L(C)$ for all graphs. They are: $L(\cdot) = 1$, $L(-) = 2$, $L(\wedge) = 6$, $L(\sqcap) = 18$, and $L(\perp) = 4$.

6. Calculate the high temperature series of the log–partition function density $\mathcal{L}(\beta)/N$, where N is the number of sites in the system, using Eq. (2.27).

2.2.4 Computational efficiency

We now discuss why the connected–cluster expansion can be considered an efficient method to calculate the high–temperature series expansion of a thermodynamic property. In principle we can calculate the high–temperature series (2.1) of a property P on a finite graph G to order N by expanding the density matrix (2.3) in a power series in β as

$$\rho_G(\beta) = \sum_{i=0}^{N} \frac{(-\beta)^i}{i!} H_G^i \tag{2.29}$$

by explicitly calculating the H_G^i and all operator averages. The dimension of the Hamiltonian H_G is given by $(d_S)^{|G|}$, where d_S is the dimension of the single site Hilbert space. Therefore the use of Eq. (2.29) is only feasible if $|G|$ is small. As the number of sites in G grows as L^d where L is the linear system size and d the dimension of the system the number of sites in G becomes prohibitively large quite fast if $d > 1$. As we have to perform an extrapolation in the system size to remove finite size effects the connected–cluster expansion becomes more efficient and more convenient quite fast. For a connected–cluster expansion to order N the property has to be calculated for graphs with N edges or less that can be embedded into the lattice. The maximum number of sites such a graph can have is $N+1$ and therefore the maximal dimension of the Hilbert space that occurs in a calculation is given by $(d_S)^{N+1}$ and therefore considerably lower than the effort in the direct calculation if $d > 1$. The number of different connected graphs that can be embedded into a lattice grows exponentially with the number of edges in the graph and therefore the property has to be calculated for an exponentially large number of graphs making high–order expansions using the connected–cluster expansion difficult.

2.3 Extensions

Having discussed the construction of the connected–cluster expansion for quantum lattice models with identical two–site interactions, we present a brief overview of two extensions that will be used in this thesis. One is the presence of different types of two–site interactions such as in the t–t'–J model introduced in chapter 1 and the other the calculation of the high–temperature series of two–point

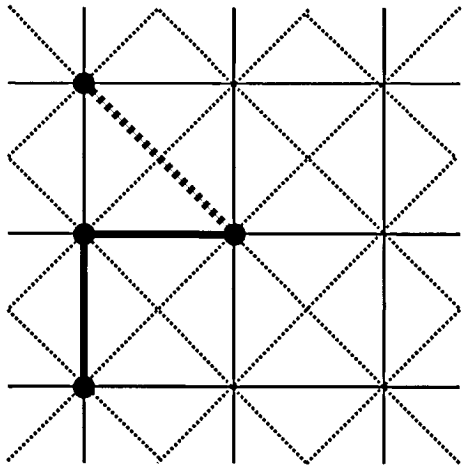

Figure 2.6: Lattice graph of the t–t'–J model as defined in Eq. (1.2) and Eq. (1.3) on a square lattice and a subgraph of the lattice graph. The solid line represents the nearest neighbor hopping (t) and the antiferromagnetic (J) exchange, while the dashed line represents the next–nearest neighbor hopping (t').

correlation functions with the help of the connected–cluster expansion. An additional extension, the calculation of impurity quantities, of the connected–cluster expansion is introduced in chapter 4.

2.3.1 Different two–site interactions

An example of a quantum lattice model with different types of interactions is the t–t'–J model defined in Eq. (1.2) and Eq. (1.3). In addition to the t–J exchange between nearest neighbor sites, it has a t' hopping between next-nearest neighbor sites and to perform a high–temperature series expansion of the model we have to distinguish between these exchange terms. This can be done by coloring the edges of the lattice graph as shown in Fig. 2.6. The graphs representing the terms of the multivariable–expansion now also become colored graphs and thermodynamic properties and all embeddings and lattice counts depend on the coloring of a graph.

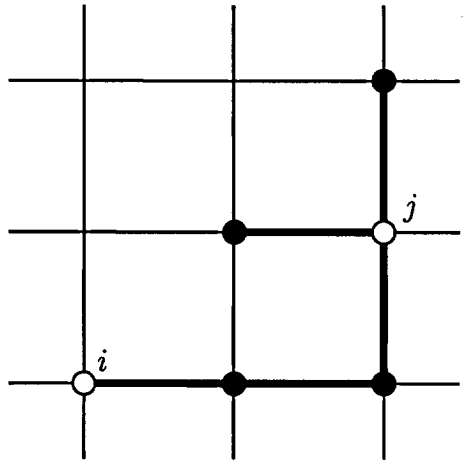

Figure 2.7: Expansion of a two–point correlation function on a (lattice) graph. The open circles in the figure denote the sites i and j for which a two–point correlation function is calculated. Also shown is a connected subgraph connecting the two sites. To obtain a connected–cluster expansion we have to "mark" the two sites in the multivariable expansion, resulting in "marked" subgraphs.

2.3.2 Two–point correlation functions

Another thermodynamic property that sometimes can be expanded in a connected–cluster expansion are two–point correlation functions $\langle A_i A_j^\dagger \rangle$ between sites i and j of the lattice graph or graph as shown in Fig. 2.7. We assume for simplicity that $\langle A_i A_j^\dagger \rangle = \langle A_j A_i^\dagger \rangle$, so that both sites can be considered equivalent, and that $\langle A_i A_j^\dagger \rangle$ satisfies the requirements (2.19) and (2.18). The connected–cluster expansion can again be constructed using a multivariable series expansion. In the multivariable series expansion we have to keep track of the location of the vertices i and j on the subgraphs. This results in embedding counts $(C'_{ij} \cdot C_{kl})$, which count the number of times the graph C' can be embedded into the graph C so that the vertex i lies on vertex k and vertex j lies on vertex l. Similarly the lattice count $L_{ij}(C_{kl})$ is the number of embeddings of C into the lattice graph with vertex k lying on vertex i and vertex l lying on vertex j. If a suitably large subgraph G of the lattice L is chosen, then $L_{ij}(C_{kl}) = (C_{kl} \cdot G_{ij})$. Furthermore the weights are now a function of the sites i and j.

2.4 Summary

In this section we have discussed the connected–cluster expansion as a method to obtain the high–temperature series expansion of a thermodynamic quantity. We have discussed the application of the connected–cluster expansion to different types of quantum–lattice models and how the steps of a practical calculation can be carried out. In the next chapter we will discuss how the series obtained has to be analyzed to extract information.


Seite Leer /
Blank leaf

Chapter 3

Series analysis

Chapter 2 discussed how the high–temperature series expansion of some thermodynamic properties can be obtained with a connected–cluster expansion. Once the series expansion has been obtained, it has to be analyzed further to extract information. For this purpose, we treat the inverse temperature β as a complex variable for this purpose. As the the methods discussed in this chapter are also applicable to other problems and in particular other types of expansions, we denote the expansion variable in which a series has been obtained by z. A series expansion

$$f(z) = \sum_{i=0}^{N} c_i z^i + O(z^{N+1}) \tag{3.1}$$

of a function $f(z)$ has only a limited use, as it is only convergent if z is within the radius of convergence R of the series [27]. If $z > R$ then the sum in Eq. (3.1) diverges when the limit $N \to \infty$ is taken. An example (taken from [28]) is the function

$$f(z) = \sqrt{\frac{1+z/2}{1+2z}}, \tag{3.2}$$

and its series expansion

$$f(z) = 1 - \frac{3}{4}z + \frac{39}{32}z^2 - \frac{267}{128}z^3 + \frac{7563}{2048}z^4 - \cdots \tag{3.3}$$

around the origin. The series expansion given by Eq. (3.3) has a radius of convergence of $1/2$ due to the singularity at $z = -1/2$. Figure 3.1 shows the function $f(z)$ and its series expansion to order 40 and how the values obtained by using

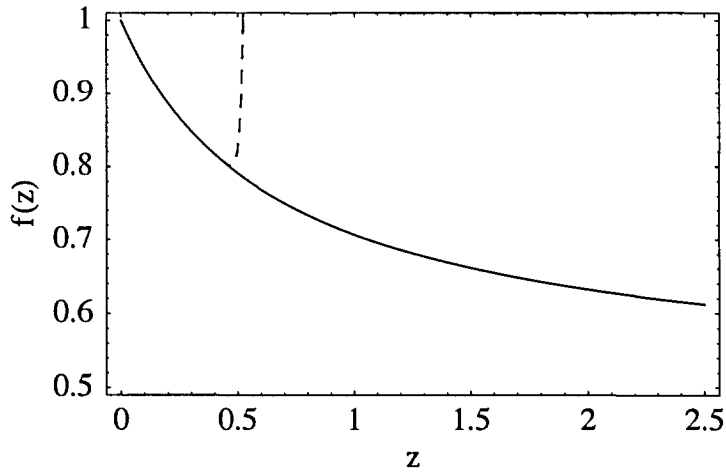

Figure 3.1: Plot of the function $f(z)$ (solid line) given in Eq. (3.2) and of its series expansion to order 40 (dashed line).

Eq. (3.3) differs from the true function value as z approaches $1/2$. To obtain the value of a function given by a series expansion outside of the radius of convergence of the series, we have to perform an *analytic continuation*. The original idea due to Weierstrass can be described as follows: Given a series expansion of a function around a point z_0 with a radius of convergence R_0, we choose a new expansion point z_1 so that $|z_0 - z_1| < R_0$ and reexpand the series expansion around this point. The series expansion obtained in this way has a new radius of convergence R_1 and can converge in a region of the complex plane that was not within the domain of convergence of the original series. This procedure is then repeated until the point of interest is within the radius of convergence.

Putting aside the problem of the uniqueness of this procedure, Weierstrasss idea is not useful in practice to perform an analytic continuation of Eq. (3.1) because all terms of the series expansion have to be known so that the method can be applied. As only a finite number of coefficients of the series expansion is known to us, we need to find alternative methods that can be applied in such a case. This chapter describes how *approximants* can be used to perform the analytic continuation of a series expansion with a finite number of coefficients. We focus on Padé approximants as they are the most widely used type of approximant and as other types of approximants are often generalizations of Padé approximants or can be treated as such. We will neglect most of the mathematical theory of

Padé approximants. Two reviews summarizing this aspect are available in [29] and [28], while an overview over the application of approximants to study critical phenomena using series expansions can be found in [30]. Because the systems to which we apply the high–temperature series expansion often do not have a finite temperature phase transition, we do not discuss the estimation of critical points and exponents using approximants.

3.1 Padé approximants

Padé approximants were first used to study the properties of a second–order phase transition with a high–temperature series expansion by Baker [31] and have been used for other problems such as the analytic continuation of imaginary time correlation functions obtained in quantum Monte Carlo simulations and approximations in engineering applications. Given the series expansion of a function

$$f(z) = \sum_{i=0}^{N} c_i z^i + O(z^{N+1}) \tag{3.4}$$

the $[L/M]$–Padé approximant to $f(z)$ is the rational fraction

$$[L/M](z) = \frac{P_L(z)}{Q_M(z)} = \frac{a_0 + a_1 z + \cdots + a_L z^L}{b_0 + b_1 z + \cdots + b_M z^M} \tag{3.5}$$

whose series expansion agrees with the series expansion of $f(z)$ to an order as high as possible. The $[L/M]$–Padé approximant has $L+1$ numerator and $M+1$ denominator coefficients. A common factor between the numerator and denominator polynomial can be eliminated by setting $b_0 = 1$. This is a natural choice as $b_0 = 0$ would imply that $f(z) \sim 1/z$ as $z \to 0$, contradicting the existence of a series expansion of the form (3.4). Then $L + M + 1$ independent coefficients remain, suggesting that $L + M + 1$ equations are needed to determine the coefficients, and that the series expansion of the $[L/M]$–Padé approximant has to agree with the the series expansion of $f(z)$ up to order $L + M$ or

$$[L/M](z) = \sum_{i=0}^{L+M} c_i z^i + O(z^{L+M+1}). \tag{3.6}$$

By multiplying Eq. (3.5) with $Q_M(z)$ on both sides and matching the coefficients of $z^0, z^1, \ldots, z^{L+M}$ we obtain a linear equation system for the coefficients a_i and

b_i. For Padé approximants this linear equation system has a block form and the denominator coefficients are independent of the numerator coefficients. The b_i are determined by the linear equation system

$$\begin{bmatrix} c_{L-M+1} & c_{L-M+2} & \cdots & c_L \\ c_{L-M+2} & c_{L-M+3} & \cdots & c_{L+1} \\ \vdots & \vdots & & \vdots \\ c_L & c_{L+1} & \cdots & c_{L+M-1} \end{bmatrix} \begin{bmatrix} b_M \\ b_{M-1} \\ \vdots \\ b_1 \end{bmatrix} = - \begin{bmatrix} c_{L+1} \\ c_{L+2} \\ \vdots \\ c_{L+M} \end{bmatrix}, \tag{3.7}$$

where $c_i = 0$ if $i < 0$. Once the denominator coefficients b_i have been determined, the numerator coefficients a_i can be obtained by multiplying $Q_M(z)$ with the series expansion of $f(z)$. If the leading coefficients of the series expansion of f are zero, the problem of constructing the $[L/M]$ approximant is replaced by the construction of a $[L'/M]$ approximant with $L' < L$. Padé approximants are sometimes arranged in a Padé table, where the numerator degree L serves as the column index and the denominator degree M as the row index. The linear equation system (3.7) has a unique solution if the determinant

$$C(L/M) = \det \begin{bmatrix} c_{L-M+1} & c_{L-M+2} & \cdots & c_L \\ c_{L-M+2} & c_{L-M+3} & \cdots & c_{L+1} \\ \vdots & \vdots & & \vdots \\ c_L & c_{L+1} & \cdots & c_{L+M-1} \end{bmatrix} \tag{3.8}$$

is not zero. In the theory of Padé approximants $C(L/M)$ is called the L/M entry of the C–table, and if $C(L/M) = 0$ then the $[L/M]$–approximant is called *defective*. It either reduces to an approximant of lower order or no solution of Eq. (3.7) exists at all. As no new information is gained by a defective approximant they have to be discarded in the analysis.

In practice also some of the approximants with $C(L/M) \neq 0$ have to be considered defective. Assume that we have an $[L/M]$ approximant with $C(L/M) = 0$, which reduces to a $[L-1, M-1]$ approximant so that

$$[L/M](z) = [L-1/M-1](z) \left(\frac{z-\lambda}{z-\lambda} \right). \tag{3.9}$$

In practice it can occur that

$$[L/M](z) = [L-1/M-1](z) \left(\frac{z-\lambda'}{z-\lambda} \right), \tag{3.10}$$

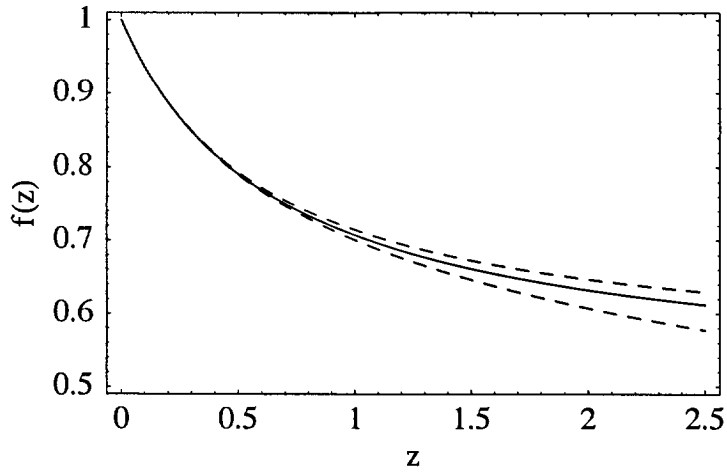

Figure 3.2: Plot of the function $f(z)$ as defined in Eqn. (3.2) and the [1/1] (short dashed line) and [1/2] (long dashed line) Padé approximants.

where $\lambda \approx \lambda'$. This approximant is not defective in the strict sense but still does not provide any new information if λ and λ' are sufficiently close. Such an approximant can for all practical purposes be considered a defective approximant. It is important to note that the occurrence of such a defective approximant is intrinsic to the method of Padé approximants and not necessarily related to any finite precision arithmetic used in the solution of Eq. (3.7).

The linear equation system (3.7) is only one of the possibilities to calculate the $[L/M]$–Padé approximant of a given series expansion. An overview over other algorithms can be found in [29]. The linear equation system is often badly conditioned, so that high–precision arithmetic has to be used to obtain a stable solution. As the series expansions we are analyzing are of moderate order and the coefficients are often rational numbers, solving Eq. (3.7) with a linear solver in a computer algebra system such as `Mathematica` or `Maple` using high–precision arithmetic where necessary is sufficient for our purposes.

The [1/1] and the [1/2] approximant to the function (3.2) are given by

$$[1/1] = \frac{1+\frac{7}{8}z}{1+\frac{13}{8}z} \tag{3.11}$$

$$[1/2] = \frac{1+\frac{29}{28}z}{1+\frac{25}{14}z+\frac{27}{224}z^2}, \tag{3.12}$$

and plotted together with the function $f(z)$ in Fig. 3.2. Neither approximant diverges from the function as $z \to 1/2$ and both give reasonable estimates of the values of $f(z)$ outside of the radius of convergence of the series (3.3). An intuitive view of why Padé approximants can extend the radius of convergence of a series is that the denominator of the Padè approximant can "detect" singularities so that the approximant is valid beyond all singularities the denominator polynomial found. This is nicely illustrated by the following theorem [28]:

> CONVERGENCE IN MEASURE THEOREM: Let $f(z)$ be analytic at the origin and also in the circle $|z| \leq R$ except for m poles, counting multiplicity. Consider a sequence $[L_k/M_k]$ of Padé approximants to $f(z)$ with $M_k \geq m$, and $L_k/M_k \to \infty$ as $k \to \infty$ ($M_k \neq 0$). Let ϵ and δ be arbitrarily small positive, given numbers. Then k_0 exists such that
>
> $$|f(z) - [L_k/M_k]| < \epsilon \tag{3.13}$$
>
> for all $k > k_0$ and for all $|z| < R$ except for $z \in \mathcal{E}$, where $\mathcal{E}$ is a set of points in the z–plane of measure less than δ.

Given a series expansion of a function with a finite number of poles, the theorem states that the Padé approximant will be able to locate those poles using its denominator polynomial and thereby extend the radius of convergence beyond those poles. Of course this is a very restricted class of functions and other results on the convergence of Padé approximants for more general classes of functions are known [28, 29]. Many mathematical results on the convergence are not useful for practical considerations as they do not make any statements about how the approximants converge to the function. In general though theorems as shown above indicate that approximants are best suited for functions they can naturally represent, which are functions with simple poles in the complex plane for the case of Padé approximants. If a function has a kind of singularity that the approximant cannot mode, we can either try to transform the function we are analyzing or use a different type of approximant.

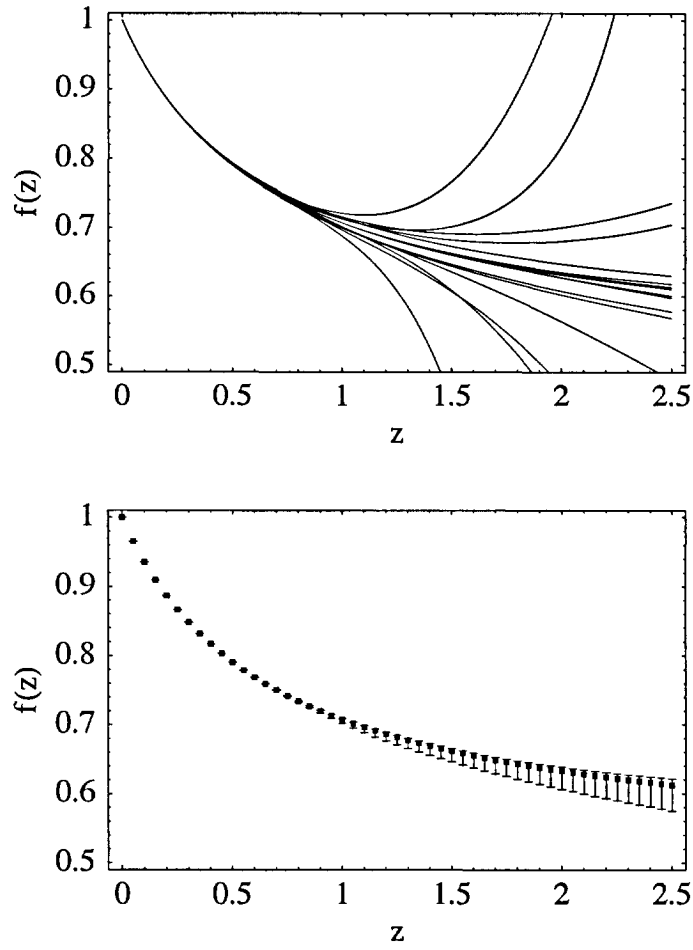

Figure 3.3: *Top*: Different Padé approximants of order 2 to 6 to the function $f(z)$ as defined in (3.2). *Bottom*: The median of the approximants is used as the typical value of f and the quartiles are shown as error bars. Note the asymmetry between error bars in both directions.

3.1.1 Error estimation

As already mentioned, the estimation of the errors of Padé approximants is an unsolved problem. We use an empirical approach that has previously been applied to series expansions by Singh [16]. The resulting error bars are more a visualization than a strict error bar but can help to simplify the presentation of the data without giving a false impression of convergence due to the selection of some particular approximants. The main idea is to visualize the difference between a large number of Padé approximants to a function using the median of all values as an estimate of the function and the quartiles as an estimate of the error. This is shown in Fig. 3.3 for different Padé approximants of order 2 to 6 to the function (3.2). Using the median and the quartiles rather than the average and the standard deviation makes the procedure stable against outliers and the method generally works well unless the resulting distribution of approximants is strongly bimodal or multimodal.

3.1.2 Variable transformations

The location of singularities in the complex plane can influence the convergence of Padé approximants. Therefore a variable transformation can significantly improve the convergence of Padé approximants. One transformation that is often used is the linear transformation of the complex plane, defined by

$$w(z) = \frac{a + b\,z}{c + d\,z} \quad (ad - bc \neq 0). \tag{3.14}$$

We will mostly consider linear transformations of the form

$$w(z) = \frac{z}{f + z} \quad (f > 0). \tag{3.15}$$

The importance of linear transformations for the mathematical theory of Padé approximants comes from the fact that diagonal Padé approximants are invariant under linear transformations as

$$[N/N]_{f(z(w))}(w(z)) = [N/N]_{f(z)}(z) \tag{3.16}$$

provided that both Padé approximants exist. Another transformation that is sometimes used is

$$w(z) = \tanh(fz) \quad (f > 0). \tag{3.17}$$

In contrast to the linear transformation this transformation has an exponential cutoff so that features of the function that we are analyzing cannot be resolved for $z \gg 1/f$. Both transformations have properties that are advantageous for the analysis of functions without a phase transition. They map the open interval $\beta \in [0, \infty)$ of the inverse temperature to a compact interval, so that offdiagonal approximants can be used for functions which are expected to have a finite value as $\beta \to \infty$. Furthermore we can generate a large set of nondefective approximants by varying the transformation parameter f so that more approximants are available for the error analysis described in section 3.1.1. Due to the special property (3.16) that diagonal approximants are invariant under linear transformations, they are often *left out* of the analysis if a large number of different values is used for f to avoid a bias towards the diagonal approximant. A more detailed discussion on desirable properties for a variable transformation can be found in Ref. [30].

3.2 Other types of approximants

Padé approximants are not the only type of approximant available and in this section we will give a brief overview over other types of approximants. All approximants have in common that they are based on a defining equation with polynomial coefficients, and that a solution for the coefficients can be found by solving a linear equation system that is obtained by matching coefficients of the expansion variable.

3.2.1 Multipoint–Padé approximants

Multipoint–Padé approximants are a natural extension of Padé approximants if the series expansion of a function f is given at K different points z_i. Writing

$$f_i(z) = \sum_{j=0}^{N_i} c_{i,j} \, (z - z_i)^j \tag{3.18}$$

for the series of the function around the i–th point, the $[L/M]_f$ multipoint–Padé approximant is the rational fraction

$$[L/M]_f(z) = \frac{P_L(z)}{Q_M(z)} = \frac{a_0 + a_1 z + \cdots + a_L z^L}{b_0 + b_1 z + \cdots + b_M z^M} \tag{3.19}$$

whose series at z_i agrees with f_i up to order N_i. Again we choose $b_0 = 1$ for convenience. As $P_L(z + z_i)$ and $Q_M(z + z_i)$ are also polynomials of degree L and M in z, finding the $[L/M]$ multipoint–Padé approximant can be reduced to the solution of a linear equation system by requiring that

$$P_L(z + z_i) = f_i(z + z_i)\, Q_M(z + z_i) + O(z^{N_i+1}) \tag{3.20}$$

for $i = 1, \ldots, K$ and matching the coefficients. If an approximant is well defined if the matrix defined by Eq. (3.20) is nonsingular and defective approximants can be detected in the same way as discussed for Padé approximants.

3.2.2 Differential approximants

For functions that do not have simple poles but power law singularities of the form

$$f(z) = r(z)(z - z_0)^\lambda, \tag{3.21}$$

taking the derivative of the logarithm of $f(z)$ with respect to z transforms the singularity to a simple pole as

$$\frac{d\log(f(z))}{dz} = \frac{\lambda}{z - z_0} + \frac{r'(z)}{r(z)}. \tag{3.22}$$

Using a Padé approximant on the derivative of the logarithm if equivalent to the equation

$$Q_M(z)\, f'(z) - P_L(z)\, f(z) = 0 \tag{3.23}$$

for the function $f(z)$. The polynomials P_L and Q_M are coefficients of a homogeneous differential equation for f. This can be generalized as follows: A differential approximant to the function f is defined by an ordinary differential equation

$$\sum_{i=0}^{K} Q_i(z)\, \mathcal{D}^i f(z) = R(z) \tag{3.24}$$

where the operator $\mathcal{D}$ can be chosen as $z\partial_z$ or ∂_z. $Q_i(z)$ and $R(z)$ are polynomials whose coefficients can be determined by solving a linear equation system obtained from coefficient matching in Eq. (3.24) as before. Padé approximants can be considered a special case of differential approximants with $K = 0$. A more detailed discussion of differential approximants can be found in Ref. [28] and Ref. [30].

3.3 Conclusion

In this chapter we have introduced approximants as a general tool to perform an analytic continuation of a series expansion. We discussed Padé approximants, how they can be calculated, how defective approximants are detected, and how the error of Padé approximants can be visualized. We have also touched upon other types of approximants and how variable transformations can be helpful in analyzing high temperature series. The most important point of this chapter is that the *type* of approximant chosen is an assumption on the functional form or type of function we are analyzing and can strongly influence the convergence of an approximant.

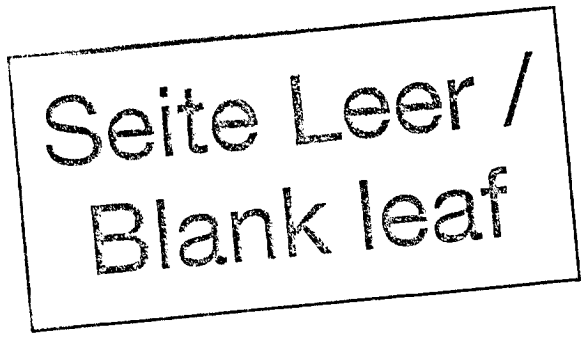
Seite Leer /
Blank leaf

Chapter 4

Impurity in a bilayer antiferromagnet

4.1 Introduction

Phase transitions of quantum–mechanical systems at zero temperature under the change of an external parameter such as the magnetic field, the pressure, or the chemical composition, also called quantum phase transitions, have been a recent subject of interest [32, 33, 34, 35]. Unusual and exotic properties are often seen close to quantum phase transitions in strongly–correlated systems, and a prime example are high–temperature superconductors, for which the onset of superconductivity is in proximity of the quantum–critical point at which the antiferromagnetic order vanishes [36]. While this transition in the high–temperature superconductors is caused by the doping of a Mott insulator as discussed in chapter 1, and is difficult to examine numerically due to the fermionic nature of the problem, the behavior of two–dimensional quantum antiferromagnets at a transition caused by a change of the magnetic coupling constants has been studied extensively using analytic [37, 38, 39] and numerical methods [40, 41, 15, 42, 43, 44, 45]. While initial work focussed on the ground–state properties of the spin–1/2 square–lattice antiferromagnet, the unusual behavior of static impurities doped into such a system has been a subject of recent interest [46, 47]. Novel boundary–critical phenomena associated with new universal exponents, a fractionalization of the

impurity spin, and the complete decoherence of an injected charge carrier were predicted based on field–theoretical arguments. In this chapter we discuss how a high–temperature series expansions of a thermodynamic property associated with such an impurity can be calculated with the connected–cluster expansion as introduced in chapter 2, and apply the method to the susceptibility of a static nonmagnetic impurity doped into a two dimensional spin–1/2 square lattice Heisenberg bilayer antiferromagnet (HBAFM). We study the impurity susceptibility at the quantum critical point using Padé approximants and compare the results to data obtained from quantum Monte Carlo simulations. Although no direct physical realization of such a bilayer system is known, the system is of interest as an effective model of a planar antiferromagnet with a quantum–critical point separating an antiferromagnetic from a quantum–disordered ground state.

4.2 Bilayer antiferromagnet

The two dimensional spin–1/2 HBAFM on a square lattice is defined by the Hamiltonian

$$H = J_1 \sum_{a=1,2} \sum_{\langle ij \rangle} \mathbf{S}_{a,i} \cdot \mathbf{S}_{a,j} + J_2 \sum_i \mathbf{S}_{1,i} \cdot \mathbf{S}_{2,i} \tag{4.1}$$

on the lattice shown in Fig. 4.2. $\mathbf{S}_{a,i}$ is a spin–1/2 operators on site i in plane a of the lattice, $J_1 > 0$ the exchange constant of nearest–neighbor spins $\langle ij \rangle$ in the plane, and $J_2 > 0$ the exchange constant of nearest–neighbor spins in adjacent planes. The strength of the quantum fluctuations in the model can be tuned by changing the dimensionless parameter $g = J_2/J_1$. In practice quantum fluctuations can also be tuned using other parameters such as the magnitude of the spins S. As long as the quantum–phase transition is a transition of a two–dimensional antiferromagnet to a two dimensional quantum disordered magnet, the scaling of various quantities remain valid due to universality.

4.2.1 Bulk properties

For $g \ll 1$ the system is dominated by the in–plane coupling J_1 and we expect the ground state to have long–range Neel order at $T = 0$, while a quantum–disordered

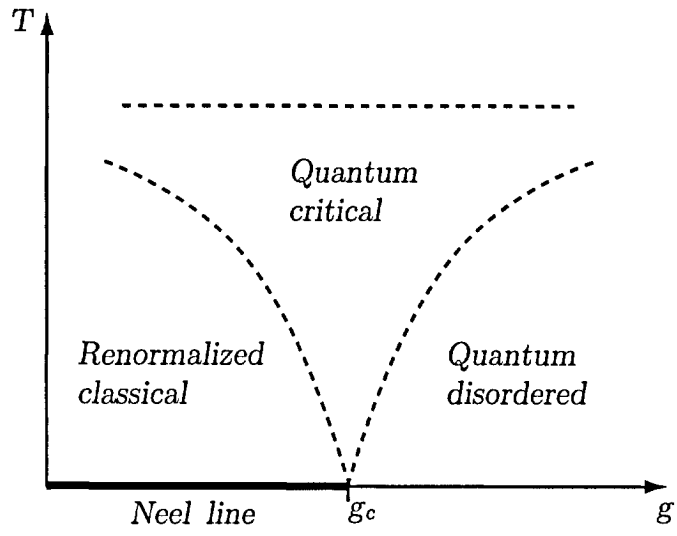

Figure 4.1: Schematic phase diagram of the Heisenberg bilayer antiferromagnet as a function of temperature and quantum fluctuations. The dashed lines do not represent phase transitions, but distinguish regions of different scaling behavior of the system. Due to scaling the quantum–critical point is not only relevant for the zero–, but also for the finite–temperature behavior of the system.

ground state is expected for $g \gg 1$, due to the formation of singlets between spins in adjacent planes. Chakravarty *et al.* [37] argued that this quantum phase transition is described by an effective field theory corresponding to the $2+1$ dimensional $O(3)$ σ model. They examined this field theory using renormalization group methods and obtained the schematic phase diagram shown in Fig. 4.1. The analysis was later extended by Chubukov *et al.* [39], using a $1/N$ expansion of the $O(N)$ σ model. The results of both papers can be summarized as follows: The HBAFM has a second–order quantum–phase transition from a Neel–ordered ground state for $g < g_c$ to a quantum–disordered state for $g > g_c$. For $g < g_c$ and sufficiently low temperatures, the system is in the so called renormalized–classical regime with long–range Neel order at $T = 0$. For $T > 0$ the Neel order is destroyed by thermal fluctuations, and the system behaves like a classical antiferromagnet whose coupling constants have been renormalized by quantum fluctuations. The behavior of the system can be fully described by the spin–wave velocity c, which remains constant as $g \to g_c$, and the spin stiffness ρ_s, which vanishes with a power law $\rho_s \sim (g - g_c)^\nu$. The $1/N$ expansion predicts that the specific heat C_V

and the uniform susceptibility χ behave as

$$C_V = \frac{3\zeta(3)}{\pi}\left(\frac{T}{c}\right)^2 \Psi_1(x_1) \tag{4.2}$$

$$\chi = \frac{T}{c^2}\Omega_1(x_1) \tag{4.3}$$

for $x_1 \ll 1$, where the scaling parameter x_1 is $NT/2\pi\rho_s$, and the scaling functions Ψ_1 and Ω_1 are given by

$$\Psi_1(x_1) = N - 1 \tag{4.4}$$

$$\Omega_1(x_1) = \frac{1}{\pi x_1} + \frac{N-2}{N\pi}. \tag{4.5}$$

Combining Eq. (4.2) and Eq. (4.3) one can see that the Wilson ratio

$$W = \frac{T\chi(T)}{C_V(T)} = \frac{\pi}{3\zeta(3)}\frac{\Omega_1(x_1)}{\Psi_1(x_1)} \tag{4.6}$$

is a universal function of x_1 only. The fact that $\chi \propto T$ at the critical point has been used to determine $g_c = 2.525 \pm 0.002$ using quantum Monte Carlo simulations [40, 45]. For $g > g_c$ the ground state of the system is quantum disordered. Neighboring spins in adjacent planes form singlets in the ground state and the excitations of the system can be described by the spin gap Δ, which is the energy needed to create a spin–1 triplet excitation. The specific heat and the uniform susceptibility both show a gapped behavior at low temperatures. As we approach the quantum–critical point, the spin gap vanishes with a power law $\Delta \sim (g - g_c)^\nu$.

Although the quantum–phase transition in the strict sense occurs at $T = 0$ only, it is relevant for the finite–temperature physics of the system for $g \approx g_c$ due to the scale invariance of the system in the spatial and the time direction. If the temperature is of the order or smaller than the microscopic couplings and the system is sufficiently close to the critical point, quantum–critical fluctuations will dominate the system. Only at very low temperatures a crossover to either the renormalized–classical or the quantum–disordered regime occurs. In the quantum–critical phase, the uniform susceptibility has a universal behavior of the form [39, 42]

$$\chi(T) = \frac{\Omega}{c^2}T, \tag{4.7}$$

with an universal amplitude $\Omega \approx 0.24$ [38, 42].

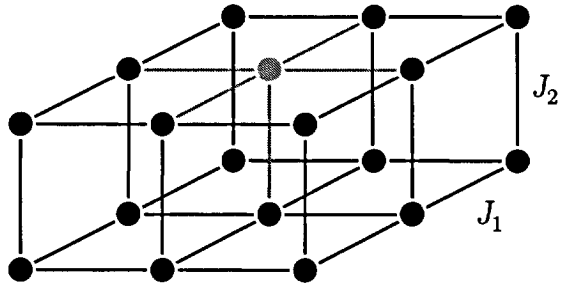

Figure 4.2: Lattice of the Heisenberg bilayer antiferromagnet with a static impurity in one of the layers shown in grey.

4.2.2 Properties of a static impurity

Recent research [46, 48, 49] has studied the effect of a static impurity in such a system close to the quantum phase transition. Examples of static impurities are a spin that is removed from one of the layers as shown in Fig. 4.2 or an additional spin coupled to one of the layers. In an experiment this can be realized by replacing Cu atoms that have spin $S = 1/2$ with magnetically inert Zn atoms in the CuO_2 planes of cuprate materials. The problem of an impurity in a bilayer antiferromagnet is reminiscent of the Kondo problem, where an impurity spin is coupled to a fermionic bath, in the sense that the impurity is coupled to a bosonic bath instead of a fermionic one. An observable sensitive to the magnetic effects of the impurity dopant is the impurity susceptibility χ_{imp}. It is defined as the difference of the uniform susceptibility of the doped system χ_{doped} and the uniform susceptibility of the pure system χ_{bulk}

$$\chi_{\text{imp}}(T) = \chi_{\text{doped}}(T) - \chi_{\text{bulk}}(T). \tag{4.8}$$

Using the mapping of the system to the $O(N)$ σ model, Sachdev *et al.* [46, 48, 49] found that the impurity susceptibility shows the behavior of a single free spin

$$\chi_{\text{imp}} = \frac{S(S+1)}{3T} \tag{4.9}$$

in the quantum disordered phase. In the renormalized classical phase the impurity enhances local antiferromagnetic correlations by suppressing the formation of resonating valence bond type singlets, leading to a

$$\chi_{\text{imp}} = \frac{S^2}{3T} \tag{4.10}$$

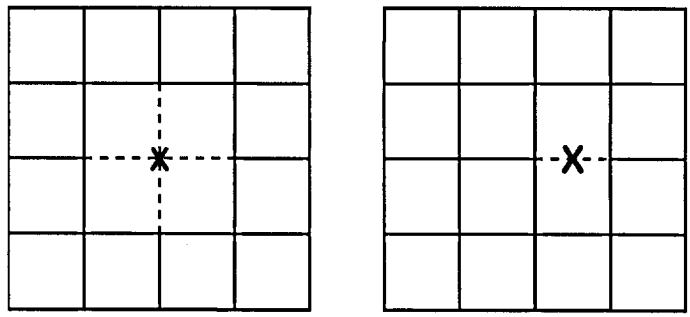

Figure 4.3: A square lattice with a static site impurity shown on the left–hand side and a static edge impurity on the right–hand side.

low–temperature behavior with logarithmic corrections [49, 50]. In Eqn. (4.9) and Eqn. (4.10) S is the quantum number of the spins in the system. At the quantum critical point, the impurity susceptibility is given by

$$\chi_{\text{imp}} = \frac{S_{\text{eff}}(S_{\text{eff}}+1)}{3T}, \tag{4.11}$$

where S_{eff} is an *effective* spin that in contrast to S does not have to be an integer or half–integer due to the absence of any energy scale at the quantum–critical point. We also note that a contradicting theory developed by Sushkov [51] predicts that $S_{\text{eff}} = S$.

As the impurity susceptibility is a microscopic quantity, it is considerably more difficult to calculate in a quantum Monte Carlo simulation than the bulk susceptibility. It has to be measured as the intensive difference of two extensive quantities. The error bars of this difference increase with the system size as L^2 in a quantum Monte Carlo simulation, where L is the linear system size, making systems of size $L > 64$ very hard to study despite the existence of efficient cluster updates for the bulk system. We therefore examine how the high–temperature series expansion of such an impurity quantity can be calculated with a connected cluster expansion and study the impurity susceptibility at the quantum critical point.

4.3 Series expansions for impurity quantities

We now present a method to calculate the high–temperature series of a *general* thermodynamic impurity quantity with a connected–cluster expansion. It can be applied to all quantities for which a connected–cluster expansion of the corresponding bulk quantity exists. We assume that the static impurity in the system can be modeled by a missing site, a missing bond, or a combination of a finite number of both as illustrated in Fig. 4.3, and to simplify the presentation we will focus on the case of a single site removed from the host lattice. We denote the impurity–free lattice graph by L and the lattice graph with the impurity site removed by L^*. To calculate the connected–cluster expansion of the impurity quantity P_I defined by

$$P_I = P_{L^*} - P_L, \tag{4.12}$$

where P_L and P_{L^*} denote the bulk property P for the lattice L and the lattice L^* respectively, we assume that P has a connected–cluster expansion so that P_L and P_{L^*} are according to Eqn. (2.23) in chapter 2 given by

$$P_L = \sum_{C \subset L} (C \cdot L)\, W_P(C) \tag{4.13}$$

and

$$P_{L^*} = \sum_{C \subset L^*} (C \cdot L^*)\, W_P(C). \tag{4.14}$$

As the lattice graphs L and L^* are infinite, Eq. (4.13) and Eq. (4.14) are to be understood in a formal sense. To make matters more precise we should take a large connected subgraph L_V of L that contains a volume V, remove the impurity to obtain a finite graph L_V^*, and then let the volume V grow until no finite–size effects remain. All graphs that can be embedded into L^* can also be embedded into L and we extend the sum in Eqn. (4.14) to all subgraphs of L. Combining Eq. (4.12), Eq. (4.13), and Eq. (4.14) we obtain

$$P_I = -\sum_{C \subset L} L^*(C)\, W_P(C), \tag{4.15}$$

where the impurity lattice count $L^*(C)$ is defined by

$$L^*(C) = (C \cdot L) - (C \cdot L^*). \tag{4.16}$$

The impurity lattice count $L^*(C)$ is the number of times the graph C can be embedded into the lattice L while at the same time touching the impurity site

and is a well–defined finite number in the thermodynamic limit. For some lattices and impurity types $L^*(C)$ is trivial in the sense that it is directly related to the lattice count $L(C)$ of the graph C, which is the number of times the graph C can be embedded per site. An example for such a case is a single site–impurity in a lattice with a simple basis (only one site per unit cell) such as the square or the triangular lattice. For such a lattice the impurity lattice count is given by

$$L^*(C) = |V(C)|\, L(C), \tag{4.17}$$

as can be seen by the following argument: Given an embedding of C into the lattice L we can obtain a distinct embedding by any lattice translation. In this way each site of C can be placed on the impurity site resulting in $|V(C)|$ embeddings of C that can be realized in L but not in L^* for each of the $L(C)$ distinct embeddings that exist per site.

If $L^*(C)$ is not related to $L(C)$ by an argument as above, it has to be calculated explicitly. For this purpose any algorithm that calculates the $L(C)$ by creating all inequivalent embeddings can be used. For each embedding that is generated we have to check how many translations of the embedding touch the impurity site. In the case of the edge impurity in the square lattice shown in Fig. 4.3 the number of edges that are embedded horizontally would have to be counted for each embedding to obtain $L^*(C)$. The weights of the property P are the same in the expansion of the impurity quantity as in the expansion of the bulk quantity so that the only additional computational effort is the calculation of the $L^*(C)$.

4.4 Application to the bilayer antiferromagnet

To apply Eqn. (4.15) to the spin–1/2 HBAFM we note that the impurity lattice count $L^*(C)$ of a graph C for the case of a single–site impurity in a bilayer lattice as shown in Fig. 4.2 is related to the lattice count $L(C)$ by

$$L^*(C) = \frac{|V(C)|\, L(C)}{2} \tag{4.18}$$

due to the mirror symmetry of the lattice with respect to a horizontal plane. This is illustrated in Fig. 4.4 for the case of a two–leg ladder: An embedding of a cluster C can be invariant under the mirror symmetry. Then only the $|V(C)|/2$

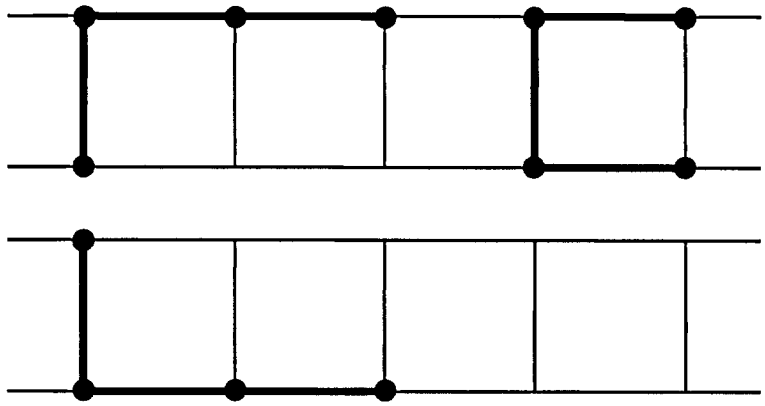

Figure 4.4: Three embeddings of a graph in a one dimensional ladder. Per embedding $|V(C)|/2$ vertices touch one of the legs of the ladder.

vertices occupying one plane can be on the impurity site. If an embedding is not invariant under the mirror symmetry, applying the symmetry will result in a new embedding, which together with the original embedding has $|V(C)|$ vertices that can be placed on the impurity site, leading to a contribution of $|V(C)|/2$ per embedding. We have calculated the weights of the uniform susceptibility of the spin–1/2 square lattice HBAFM to order β^{11} using all connected clusters with 10 edges or less that can be embedded into the bilayer lattice. The calculation of the susceptibility of each cluster was performed with a C++ program, and the weights were calculated using the computer algebra programs `Mathematica` and `Maple`. The resulting series in the inverse temperature β and the coupling constants J_1 and J_2 is given by

$$\chi_{\text{imp}}(\beta) = \beta \sum_{k,l} \chi_{\text{imp}}[k,l]\,(\beta J_1)^k\,(\beta J_2)^l, \tag{4.19}$$

and the coefficients of the series are listed in Table 4.4. To analyze the impurity susceptibility, we fix the coupling constants at the quantum–critical point using values of $J_1 = 1$ and $J_2 = 2.525$ [45], and study the series expansion of

$$C_1(\beta) = \frac{4\,\chi_{\text{imp}}}{\beta}. \tag{4.20}$$

Based on the predictions of Eq. (4.11), we expect $C_1(\beta)$ to go to a positive constant as $\beta \to \infty$. If $S_{\text{eff}} = S$ as predicted by Sushkov, then $C_1(\infty) = 1$, while the fractionalization of S_{eff} as predicted by Sachdev implies $C_1(\infty) \neq 1$.

k	l	$\chi_{\mathrm{imp}}[k,l]$
0	0	$-\frac{1}{4}$
1	0	$\frac{1}{2}$
0	1	$\frac{1}{8}$
2	0	$-\frac{7}{16}$
1	1	$-\frac{3}{8}$
0	2	$\frac{1}{32}$
3	0	$\frac{13}{48}$
2	1	$\frac{17}{32}$
1	2	$-\frac{1}{32}$
0	3	$-\frac{1}{384}$
4	0	$-\frac{35}{256}$
3	1	$-\frac{1}{2}$
2	2	$-\frac{13}{256}$
1	3	$\frac{5}{128}$
0	4	$-\frac{5}{1536}$
5	0	$\frac{23}{320}$
4	1	$\frac{93}{256}$
3	2	$\frac{265}{1536}$
2	3	$-\frac{131}{1536}$
1	4	$\frac{17}{1536}$
0	5	$-\frac{13}{30720}$
6	0	$-\frac{5669}{184320}$
5	1	$-\frac{3533}{15360}$
4	2	$-\frac{1519}{7680}$
3	3	$\frac{2837}{30720}$
2	4	$-\frac{247}{61440}$
1	5	$-\frac{27}{10240}$
0	6	$\frac{77}{368640}$
7	0	$\frac{6383}{860160}$
6	1	$\frac{3067}{23040}$
5	2	$\frac{60721}{368640}$
4	3	$-\frac{3809}{73728}$
3	4	$-\frac{4991}{184320}$

k	l	$\chi_{\mathrm{imp}}[k,l]$
2	5	$\frac{1517}{122880}$
1	6	$-\frac{677}{368640}$
0	7	$\frac{823}{10321920}$
8	0	$-\frac{4223}{1376256}$
7	1	$-\frac{347773}{5160960}$
6	2	$-\frac{2641403}{20643840}$
5	3	$\frac{14393}{1290240}$
4	4	$\frac{61517}{1376256}$
3	5	$-\frac{1829}{86016}$
2	6	$\frac{60017}{20643840}$
1	7	$-\frac{47}{688128}$
0	8	$-\frac{25}{8257536}$
9	0	$\frac{218977}{74317824}$
8	1	$\frac{68519}{2293760}$
7	2	$\frac{3815159}{41287680}$
6	3	$\frac{836327}{123863040}$
5	4	$-\frac{220609}{5160960}$
4	5	$\frac{153961}{10321920}$
3	6	$\frac{27733}{24772608}$
2	7	$-\frac{46903}{41287680}$
1	8	$\frac{7937}{41287680}$
0	9	$-\frac{11593}{1486356480}$
10	0	$-\frac{2077973}{4954521600}$
9	1	$-\frac{3362573}{247726080}$
8	2	$-\frac{147407089}{2972712960}$
7	3	$-\frac{22484627}{1486356480}$
6	4	$\frac{49877111}{1486356480}$
5	5	$-\frac{3170327}{928972800}$
4	6	$-\frac{695789}{99090432}$
3	7	$\frac{1842889}{495452160}$
2	8	$-\frac{122341}{198180864}$
1	9	$\frac{23273}{495452160}$
0	10	$-\frac{37873}{29727129600}$

Table 4.1: Coefficients of the high temperature series expansion of a static impurity site in a two–dimensional square lattice HBAFM.

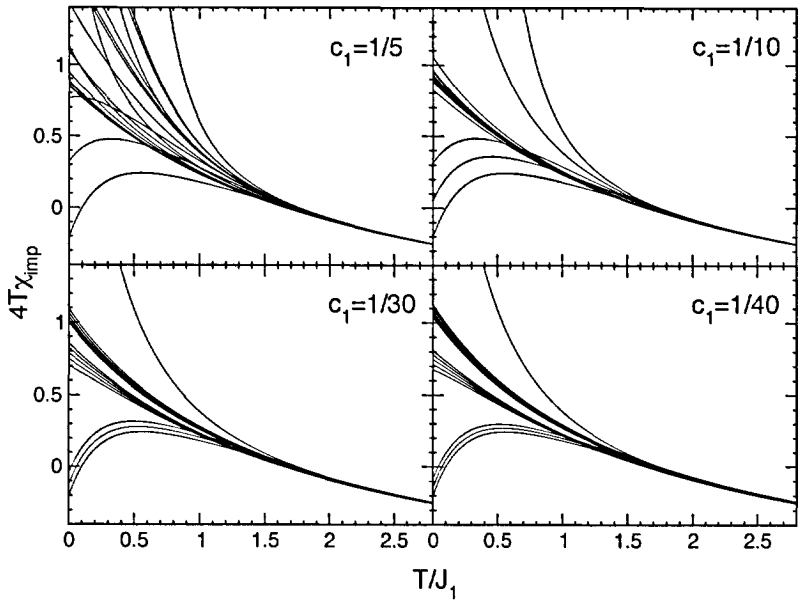

Figure 4.5: Non-defective Padé approximants to $C_1(\beta) = 4T\chi_{\rm imp}$ at the quantum critical point for $c_2 = 1/2$ and different values of c_1. As c_1 becomes smaller the approximants seem to converge to lower temperature but also split into two branches.

To determine the behavior of $C_1(\beta)$ we transform the series from the inverse temperature β to a new variable w with the help of the linear transformation

$$w = \frac{\beta}{c_1 + c_2\,\beta}. \tag{4.21}$$

We form Padé approximants of order 6 and higher to the transformed series for different values of c_1 and set $c_2 = 1/2$. All defective approximants and all approximants that have a pole on the real axis for $w \in [0, 1/c_2]$ are discarded. We designate an approximant as defective if the distance between a numerator and a denominator zero is less than 10^{-6} in the complex w plane. The result of this analysis is shown in Fig. 4.5 for different values of c_1. Starting at $c_1 = 1/5$ we see that the convergence of the approximants improves for smaller values of c_1. For $c_1 = 1/30$ the approximants seem to have split into two different branches and to determine which of the approximants shown in Fig. 4.5 are reliable we examine the location of the zeroes and poles of the Padé approximants in more detail. Figure 4.6 shows the distribution of the zeroes and poles of four different Padé approximants in the complex w-plane for $c_1 = 1/30$. Although the zeroes

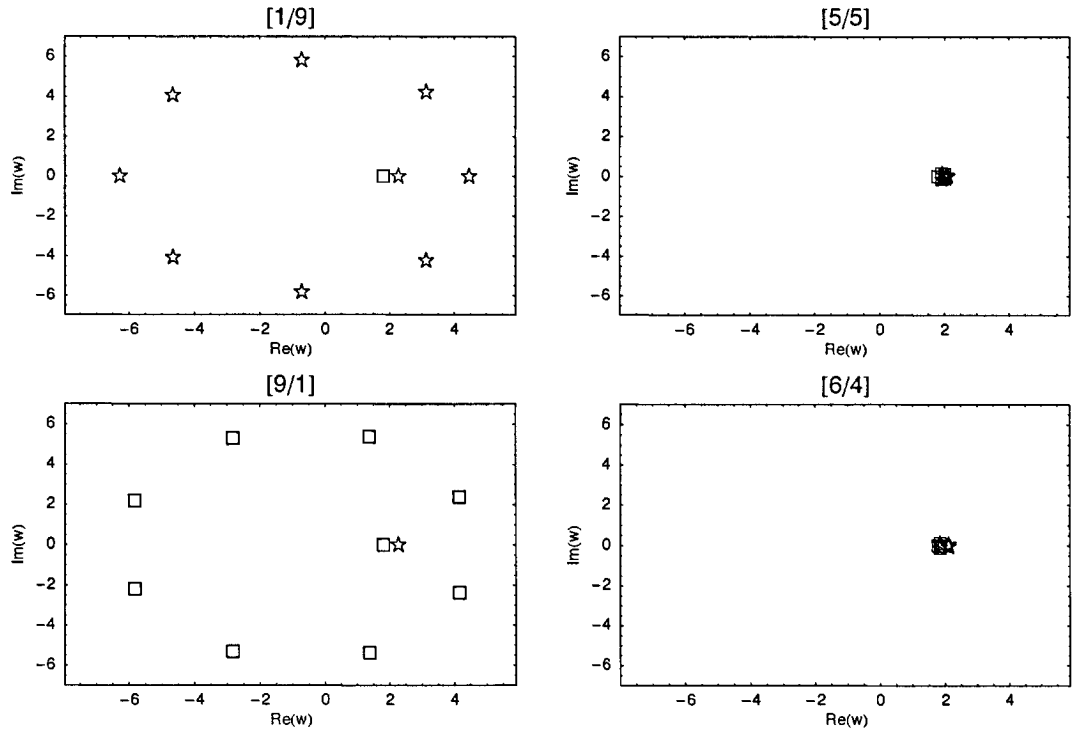

Figure 4.6: Location of the zeroes (□) and poles (⋆) of different Padé approximants for $c_1 = 1/30$. While the zeroes and poles of the [5/5] and the [6/4] approximants have a distance larger than 10^{-6}, the approximants cluster all zeroes and poles close to $w = 1/c_2 = 2$ and we discard them as defective. Note the symmetry of the zero and pole distribution of the [9/1] and [1/9] approximant.

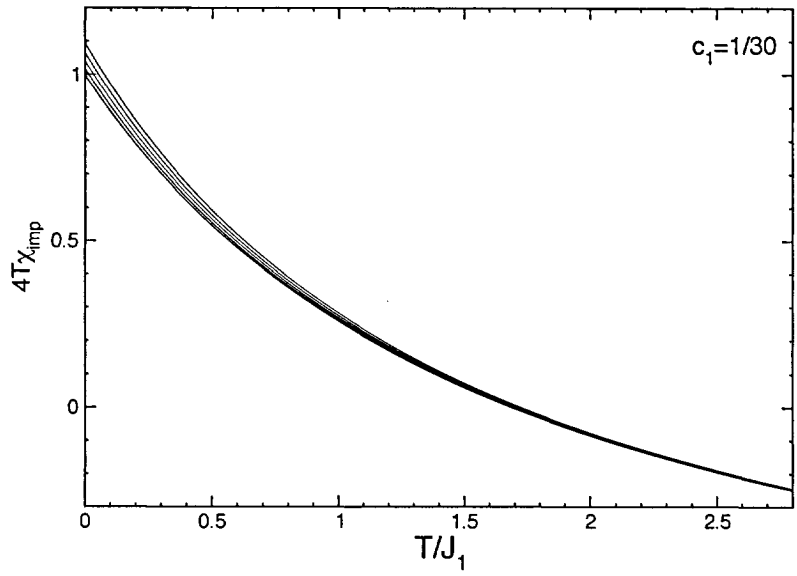

Figure 4.7: The ten $[L/1]$ and $[1/M]$ Padé approximants of order 6 and higher for $c_1 = 1/30$ and $c_2 = 1/2$. The $[N/1]$ and $[1/N]$ approximant overlap and are not distinguishable on the scale shown.

and poles of the [5/5] and the [6/4] approximants have a distance larger than 10^{-6}, they are clustered in the proximity of $w = 1/c_2 = 2$ and we discard them as defective. This is the case for all approximants except for the $[L/1]$ and $[1/M]$ approximants which have a pole and a zero close to $w = 1/c_2$ and either zeroes or poles forming an ellipsoid around the origin. The $[L/1]$ and $[1/M]$ approximants for $c_1 = 1/30$ are plotted in Fig. 4.7 and the extrapolated zero temperature values $C_1(\infty)$ are listed in Table 4.2. Using values of c_1 of 1/5, 1/10, 1/30, and 1/40 we obtain non–defective approximants with values of $C_1(\infty)$ ranging from 0.92 to 1.07. Thus we estimate $C_1(\infty) = 0.99 \pm 0.07$, a result that cannot distinguish between fractionalization of S_{eff} as predicted by Sachdev and $S_{\text{eff}} = S$ as predicted by Sushkov.

The extrapolation of $C_1(\beta)$ to zero temperature using the Padé approximants to the transformed series deserves some further discussion. As the system at the quantum–critical point has only the temperature T as its energy scale if $T < J_i$, we do not have any low energy scales to overcome using the approximants. Thus it is not unexpected that the approximants seem to work to rather low temperatures at the quantum–critical point. On the other hand it is possible

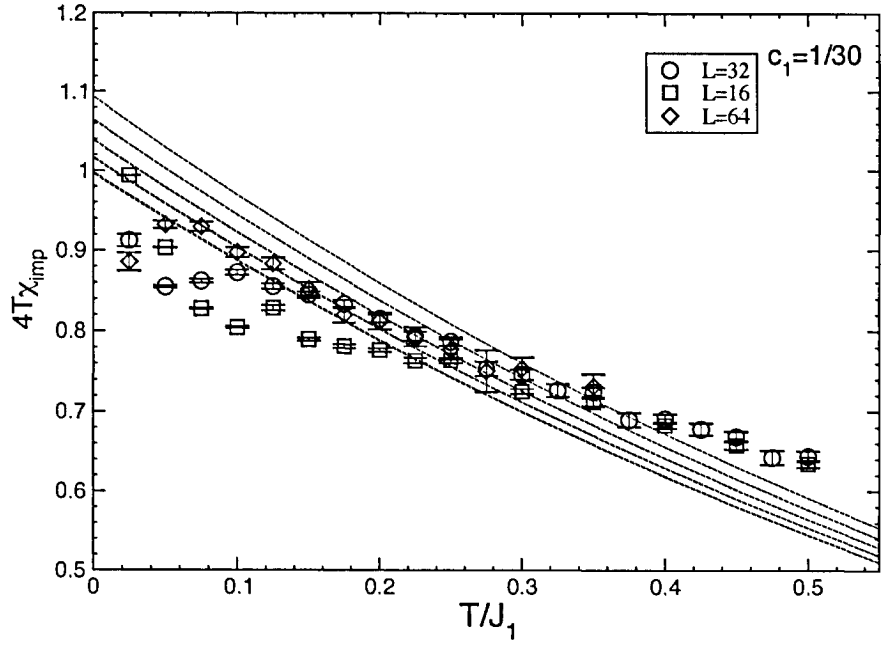

Figure 4.8: Comparison of the results of the Padé analysis described in section 4.4 with QMC calculations.

that Padé approximants are so different from the true functional form of $C_1(\beta)$ that a systematic error is present. Figure 4.8 shows a comparison of the results obtained from a high–temperature series expansion and Padé approximants with results obtained using quantum Monte Carlo simulations of systems of size L=16, 32, and 64. The series expansion data agrees well with the quantum Monte Carlo simulations of the L=64 system, although the general trend seems to be that QMC and series expansion results cross. Unfortunately it is difficult to calculate $C_1(\beta)$ for high temperatures using QMC simulations, so that we cannot determine if the Padé approximant has the wrong functional form.

4.5 Conclusion

In this chapter we have introduced a method to calculate the impurity susceptibility of a static nonmagnetic impurity with a high–temperature series expansion. By applying Padé approximants to the high–temperature series after a linear transformation we determine $C_1(\infty) = 0.99 \pm 0.07$. Thus using the high–

Approximant	$C_1(\infty)$
[1/5]	1.093
[5/1]	1.094
[1/6]	1.064
[6/1]	1.065
[1/7]	1.038
[7/1]	1.040
[1/8]	1.016
[8/1]	1.017
[1/9]	0.996
[9/1]	0.998

Table 4.2: Asymptotic values of the non–defective approximants for $c_1 = 1/30$ and $c_2 = 1/2$ as described in the text.

temperature series expansion, we cannot distinguish between the theoretical predictions of Sachdev *et al.* and Sushkov.

Chapter 5

Normal–state properties of the t–t'–J model

5.1 Introduction

The unusual normal–state properties of the hole–doped copper oxide superconductors mentioned in chapter 1 raised the question if these materials are described by Fermi–liquid theory or not [52]. Transport measurements indicate that the resistivity of the hole–doped cuprates is proportional to the temperature T over a wide range of temperatures at optimal doping, while Fermi–liquid theory predicts that the resistivity should be proportional to T^2. Another example for the unusual behavior are the results of angle–resolved photoemission spectroscopy experiments, which indicate that some of the excitations in the system acquire a gap below the so called pseudogap temperature T^* [11, 12]. This stands in contrast to experiments on the electron–doped copper oxide superconductors, which seem to be well described by Fermi–liquid theory. A large number of different theories have been introduced to explain the breakdown of Fermi–liquid theory in the hole–doped cuprates. An example of such a theory is the opening of the pseudogap due to umklapp–scattering processes proposed by Honerkamp *et al.* [53].

The fact that electron–doped cuprates but not hole–doped cuprates seem to be well described by Fermi–liquid theory is even more surprising when one considers,

that it is today generally accepted that both systems can be modeled as doped Mott insulators with parameters of similar magnitude, as discussed in chapter 1. Understanding the phase diagram of the Hubbard or the t–t'–J model is therefore an essential step in understanding the cuprates and their experimental phase diagram.

In this chapter we study some aspects of the phase diagram of the t–t'–J model with high–temperature series expansions. Due to the nature of the high–temperature series expansion only normal–state properties can be studied, and we will not attempt to determine the low–temperature order in the model and in particular if the model becomes superconducting, a question that has remained controversial [23, 54, 55, 56]. We study the uniform susceptibility χ, the magnetic structure factor $S(\mathbf{q})$, and the momentum distribution function $n(\mathbf{q})$ as a function of the density and the next–nearest neighbor hopping. These quantities were examined for the t–J model in previous studies [16, 17, 21]. Using the t–t'–J model and not the Hubbard model has the advantage that the coupling constants are of the same order of magnitude, so that the extrapolation of the series is stabilized.

The t–t'–J Hamiltonian introduced in chapter 1 is given by

$$H_{tJ} = -t \sum_{\langle ij \rangle, \sigma} \mathcal{P} \left(c^{\dagger}_{i\sigma} c_{j\sigma} + c^{\dagger}_{j\sigma} c_{i\sigma} \right) \mathcal{P} + J \sum_{\langle ij \rangle} \mathbf{S}_i \cdot \mathbf{S}_j \tag{5.1}$$

and

$$H_{ttJ} = H_{tJ} - t' \sum_{\langle\langle ik \rangle\rangle, \sigma} \mathcal{P} \left(c^{\dagger}_{i\sigma} c_{k\sigma} + c^{\dagger}_{k\sigma} c_{i\sigma} \right) \mathcal{P}, \tag{5.2}$$

where the sums run over all all nearest neighbor pairs $\langle ij \rangle$ and over all next–nearest neighbor pairs $\langle\langle ik \rangle\rangle$ of the square lattice. $c^{\dagger}_{i\sigma}$ is an electron creation operator, $\mathbf{S}_i$ an electron spin operator, and $\mathcal{P} = \prod_i (1 - n_{i\uparrow} n_{i\downarrow})$ is a projection operator removing all states with doubly occupied sites. The density of particles in the system is

$$\rho = \frac{1}{N} \sum_i n_i, \tag{5.3}$$

where N is the number of sites in the system and is related to the doping x by $x = 1 - \rho$. The magnetic structure factor is defined by

$$S(\mathbf{q}) = \sum_j e^{i\,\mathbf{q}\cdot(\mathbf{r}_0 - \mathbf{r}_j)} \langle S^z_0 S^z_j \rangle, \tag{5.4}$$

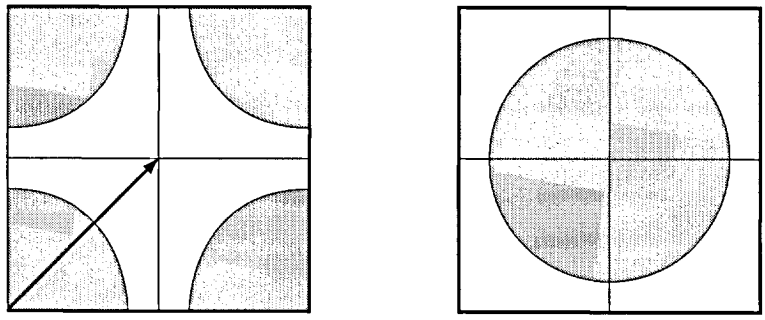

Figure 5.1: Change of the Fermi surface after a momentum shift by $\mathbf{Q} = (\pi, \pi)$ for the electron–doped cuprates as described in the text. The Fermi volume is shaded in grey. The momentum shift changes the sign of the nearest–neighbor hopping term t in the t–t'–J model, so that the differences between electron– and hole–doped cuprates can be discussed as a change of the next–nearest neighbor hopping parameter t'.

and the momentum distribution function by

$$n(\mathbf{q}) = \sum_j e^{i\,\mathbf{q}\cdot(\mathbf{r}_0 - \mathbf{r}_j)} \langle c^\dagger_{0\sigma} c_{j\sigma} \rangle, \tag{5.5}$$

where $\langle S^z_i S^z_j \rangle$ and $\langle c^\dagger_{i\sigma} c_{j\sigma} \rangle$ are thermodynamic equal–time two–point correlation functions on the square lattice, and $\mathbf{r}_i$ is the position of site i in the lattice. The uniform susceptibility can be calculated from the magnetic structure factor as

$$\chi = \beta\, S(\mathbf{0}). \tag{5.6}$$

All quantities are defined in the grand–canonical ensemble at fixed fugacity or respectively at a fixed chemical potential. Using Eq. (5.3), we can change variables from the chemical potential to the density.

First principles calculations [6] and comparison of spectra obtained from angle–resolved photoemission spectroscopy with exact diagonalization results show that typical parameter values for the t–t'–J model in the cuprates are given by $t \sim$ 400meV, $t' \sim -125$meV, and $J \sim 125$meV for the hole–doped cuprates and by $t \sim -400$meV, $t' \sim 125$meV, and $J \sim 125$meV for the electron–doped cuprates. To compare the effects of electron– and hole–doping in a high–temperature series expansion, it is convenient to shift the momentum in the electron–doped cuprates by the antiferromagnetic ordering vector $\mathbf{Q} = (\pi, \pi)$. The square lattice is a

bipartite lattice with two sublattices and by using the transformation $c^\dagger_{i\sigma} \rightarrow -c^\dagger_{i\sigma}$ for the sites in one of the sublattices, the parameters of the t–t'–J model transform as $t \rightarrow -t$, $t' \rightarrow t'$, and $J \rightarrow J$. This leads to a momentum shift $\mathbf{Q}$ for the momentum distribution function $n(\mathbf{q})$ as illustrated in Fig. 5.1, while the magnetic structure factor $S(\mathbf{q})$ remains invariant. After the momentum shift the nearest–neighbor hopping of both types of cuprates has a positive sign so that differences between electron– and hole–doping can be studied as a function of the next–nearest neighbor hopping parameter t' which is positive for electron–doped compounds and negative for hole–doped compounds. For the rest of this chapter we take the physically realistic values $t = 1$ and $J = 1/3$ for the nearest–neighbor hopping and the antiferromagnetic exchange coupling. The next–nearest neighbor hopping parameter is varied from $t' = 1/3$ for the electron–doped compounds to $t' = -1/3$ for the hole–doped compounds.

5.2 High–temperature series and analysis

The high–temperature series expansions of the equal–time correlation functions $\langle S^z_i S^z_j \rangle$ and $\langle c^\dagger_{i\sigma} c_{j\sigma} \rangle$ were calculated in the grand–canonical ensemble. First the high–temperature series expansion of the grand–canonical log–partition function density

$$\mathcal{L}(\beta, z) = \frac{1}{N} \log \left(\mathrm{Tr}\, e^{-\beta H_{tt'J} + \log(z)\, n} \right) \tag{5.7}$$

is calculated as a function of the fugacity z. $n = \sum_i n_i$ the number operator and N the number of sites in the system. Because the t–t'–J Hamiltonian conserves the total number of particles, $\mathcal{L}(\beta, z)$ is also a polynomial in the fugacity z. The high–temperature series of the density $\rho = \sum_i n_i / N$ can be calculated from Eq. (5.7) via

$$\rho(\beta, z) = z\, \partial_z\, \mathcal{L}(\beta, z). \tag{5.8}$$

By inverting Eq. (5.8) we obtain the fugacity $z(\beta, \rho)$ as a power series in the inverse temperature β and the density ρ. In the practical implementation it is advantageous to perform a change of variables from the fugacity z to the variable $g = z/Z_0$, where $Z_0 = 1 + 2z$ is the single–site partition function of the noninteracting system. The power series of $\mathcal{L}$, ρ and the equal–time correlation functions are by construction polynomials in the variable g. In the next step

the high–temperature series expansions of the equal–time two–point correlation functions $\langle S_i^z S_j^z \rangle$ and $\langle c_{i\sigma}^\dagger c_{j\sigma} \rangle$ are calculated. Using the power series of the fugacity in β and ρ obtained by inverting Eq. (5.8) they can be expressed as power series of the inverse temperature and the density so that the fugacity has been eliminated from all quantities.

All series are calculated to order β^8 by using the 16457 distinct clusters with 8 edges or less that can be embedded into the lattice graph of the t–t'–J model. After the series have been transformed from the fugacity to the density, the parameters ρ, t, t', J, and $\mathbf{q}$ are fixed, and the resulting high–temperature series is analyzed with Padé approximants as described in chapter 3. Using a linear transformation of the form

$$w = \frac{\beta}{f + \beta} \tag{5.9}$$

with values of f ranging from 1/20 to 2, we change to a new variable w and apply offdiagonal Padé approximants of order 7 and 8 to the series. We do not use diagonal approximants as they are invariant under the transformation in Eq. (5.9). In general we aim to obtain at least 50 approximant per data point. Defective approximants, here taken to be approximants whose smallest distance between a numerator and denominator zero in the variable w is smaller than 10^{-4}, are discarded. Furthermore approximants which have a pole for $\beta \in [0, \infty)$ are discarded, as the system is not expected to have a phase transition in the temperature ranges considered here. Choosing a lower limit on the numerator–denominator zero distance of 10^{-6} and including the diagonal approximants in the analysis did not change the qualitative and quantitative results of the analysis. The results of this analysis are summarized by the median as an estimate of the function value and the quartiles as estimates of the error bars.

5.3 The uniform susceptibility χ

We begin our analysis with the magnetic properties, and study the uniform susceptibility $\chi = \beta\, S(\mathbf{0})$ as a function of the doping $x = 1 - \rho$ and the next–nearest neighbor hopping t'. Figure 5.2 shows a plot of χ and $S(\mathbf{0})$ for the half–filled system ($\rho = 1$), corresponding to the spin–1/2 Heisenberg antiferromagnet on the square lattice. The susceptibility has a peak at temperature $T \sim J$ and then

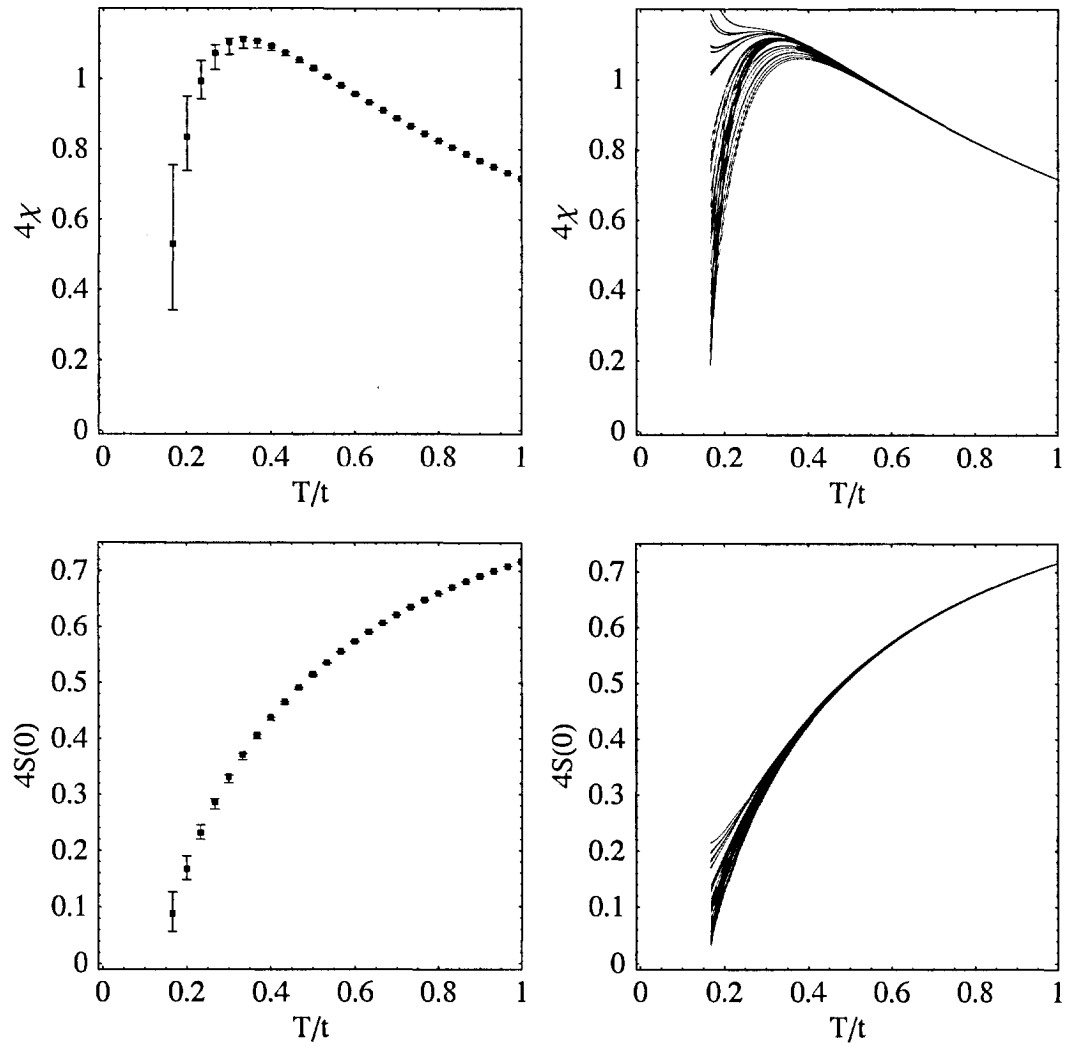

Figure 5.2: Uniform susceptibility χ and magnetic structure factor $S(\mathbf{0}) = T\chi$ for the spin–1/2 Heisenberg antiferromagnet on a square lattice with $J = 1/3$ ($t = 1$). The plots on the left hand side are obtained from the approximants on the right hand side by taking the median as an estimate of the function value and by taking the quartiles as error bars.

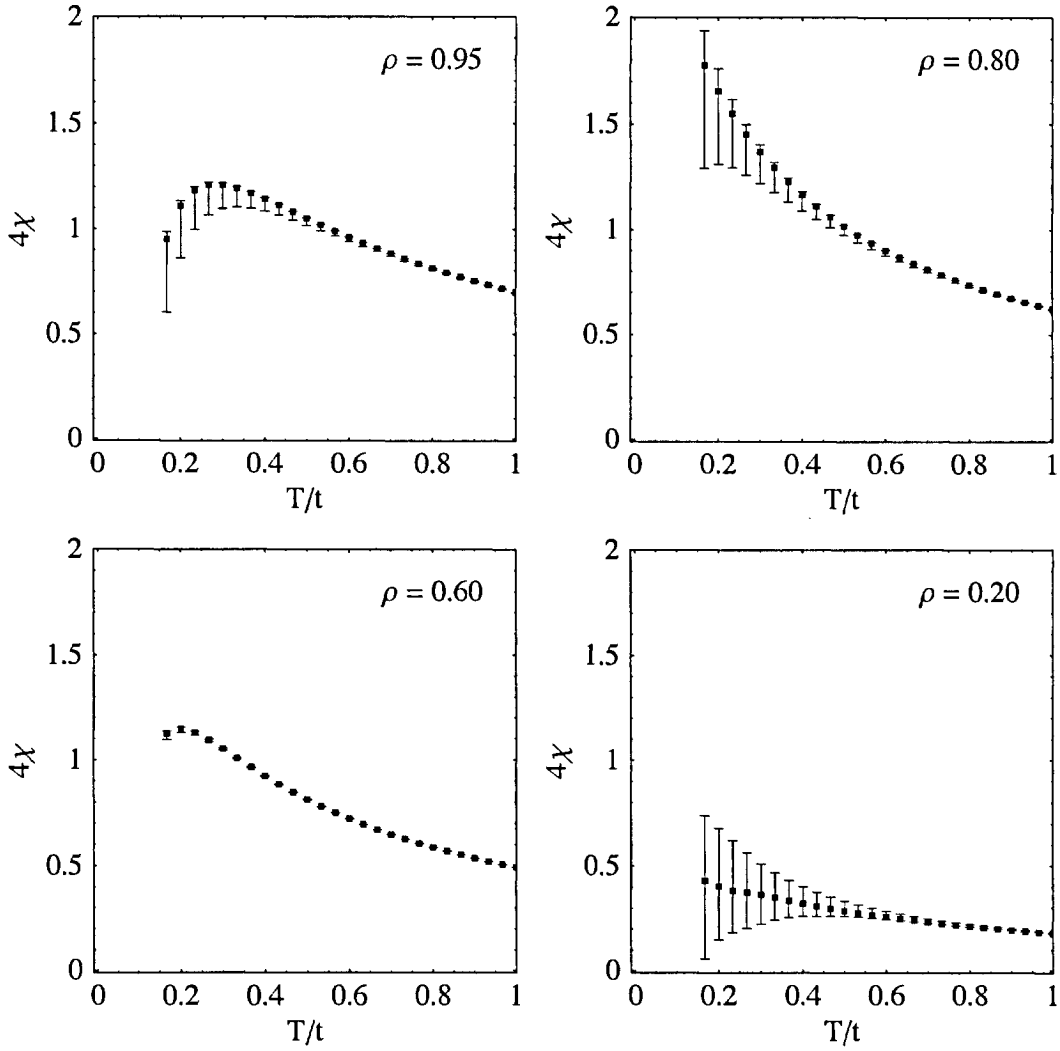

Figure 5.3: The uniform susceptibility χ of the t–J model ($t = 1$, $J = 1/3$, $t' = 0$) for densities $\rho = 0.95$, 0.80, 0.60, and 0.20. Upon doping the susceptibility is at first enhanced before approximately becoming proportional to the density ρ.

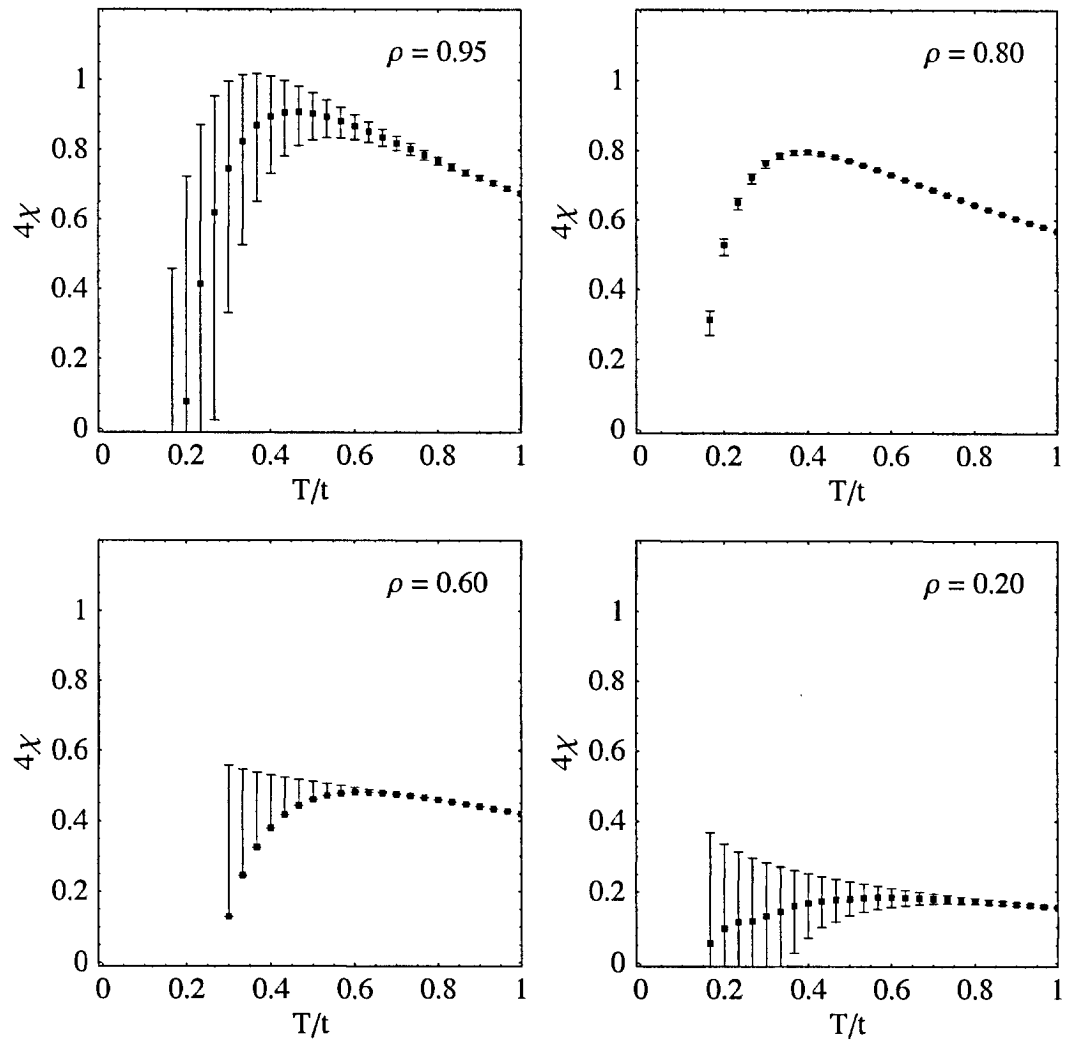

Figure 5.4: The uniform susceptibility χ of the t–t'–J model for $t' = 1/3$ ($t = 1/3$, $J = 1/3$, corresponding to electron–doping) for densities $\rho = 0.95$, 0.80, 0.60, and 0.20. For all levels of doping the susceptibility retains the characteristic shape of an antiferromagnet and its maximum seems to be proportional to the density ρ for the whole doping range.

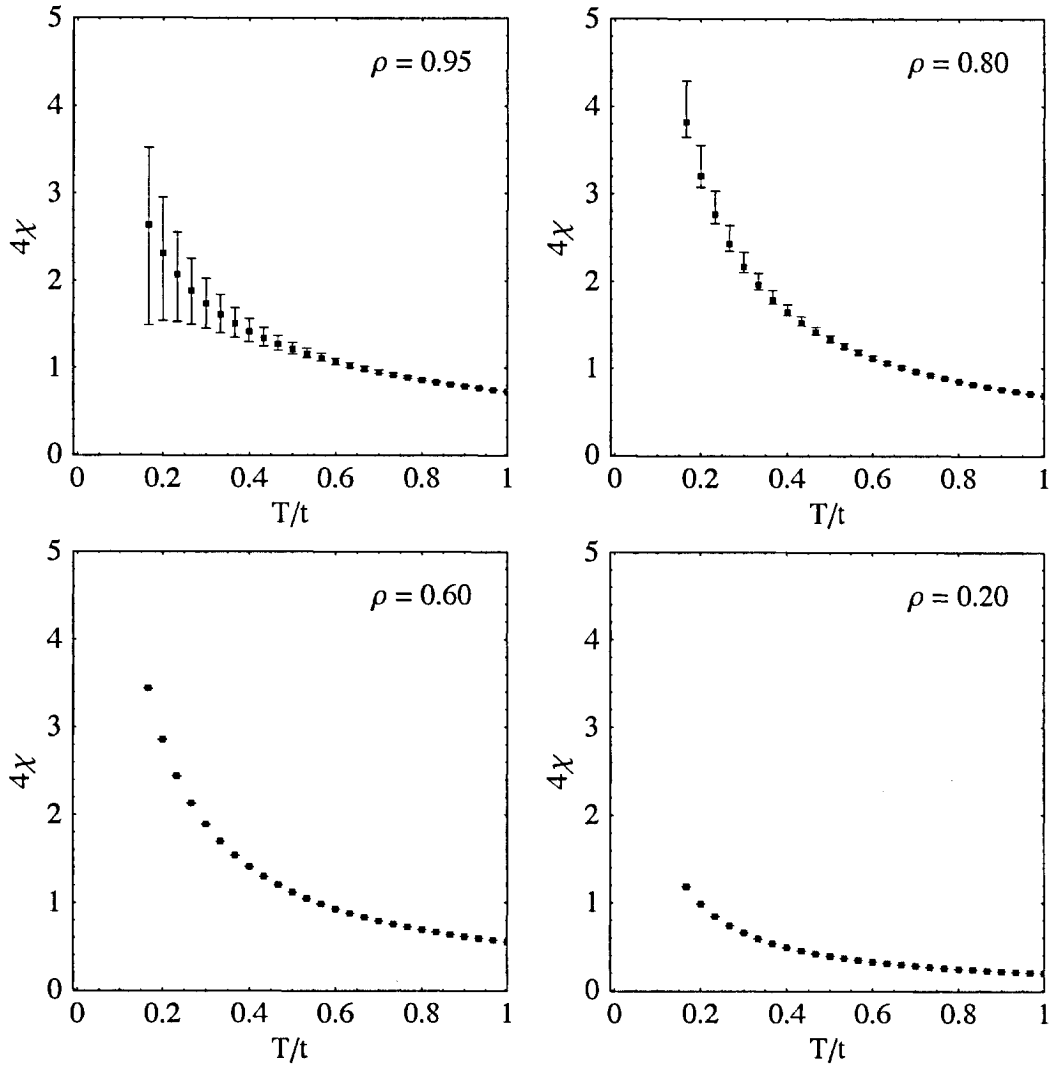

Figure 5.5: The uniform susceptibility χ of the t–t'–J model for $t' = -1/3$ ($t = 1/3$, $J = 1/3$, corresponding to hole–doping) for densities $\rho = 0.95$, 0.80, 0.60, and 0.20. Even for extremely weak doping the susceptibility loses the shape characteristic for an antiferromagnet. The susceptibility is strongly enhanced at $\rho = 0.80$ before and becomes proportional to ρ for larger ρ.

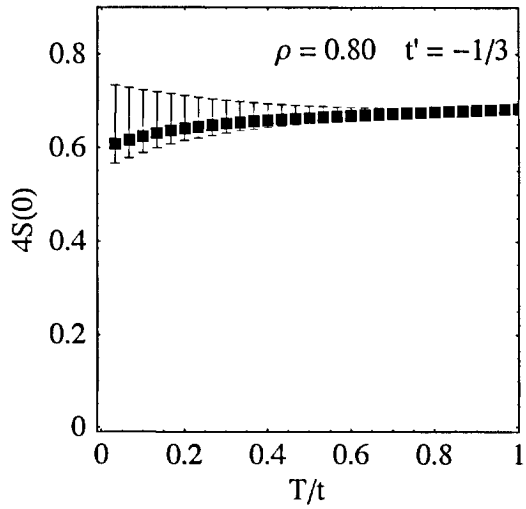

Figure 5.6: $S(\mathbf{0}) = T\chi$ for the t–t'–J model with parameters $t = 1$, $t' = -1/3$, $J = 1/3$, and $\rho = 0.80$ (corresponding to hole–doping). The susceptibility is that of a free spins with a renormalized spin value compared to high–temperatures. The poles of the Padé approximants to the series do not indicate any ferromagnetic transition at low temperatures.

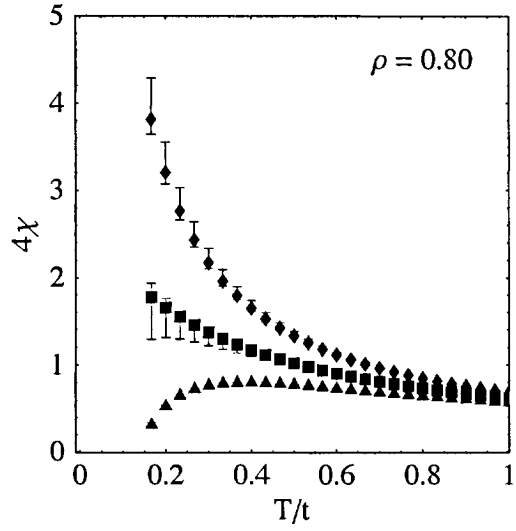

Figure 5.7: Uniform susceptibility for different values of the next–nearest neighbor hopping parameter $t' = 1/3$ (triangles), 0 (squares), and $-1/3$ (diamonds). A change of the next nearest–neighbor hopping strongly changes the behavior of the uniform susceptibility.

drops to a finite value for $T \rightarrow 0$ (see also chapter 4). Using Padé approximants we can extrapolate the series of the susceptibility to temperatures of the order $T \sim J/2 = t/6$. Below a temperature of the order $J/10$ the approximants to $S(\mathbf{0})$ become negative, an unphysical behavior as $S(\mathbf{q}) \geq 0$ for all temperatures and $\mathbf{q}$. The convergence of the susceptibility for the undoped antiferromagnet can be significantly improved by using differential approximants. For the doped system however no consistent improvement of the results could be observed and therefore only the results obtained with Padé approximants are reported here.

If the t–J model is doped weakly ($x = 0.05$) the susceptibility retains the shape typical for an antiferromagnet and its maximum increases as shown in Fig. 5.3. Upon further doping ($x = 0.20$) the antiferromagnetic peak vanishes or is located below temperatures that can be reached with our high–temperature series while the peak value of the susceptibility increases at the same time. For higher doping levels ($x = 0.40,\ 0.80$) the susceptibility becomes flat as a function of the temperature and its magnitude is essentially proportional to the carrier density ρ. These results agree qualitatively with the results of Singh [16], although we do find quantitative differences depending on the variable transformation used. We also cannot exclude the possibility that the differences are due to the higher order of the series used by Singh.

The electron–doped t–t'–J model represented by $t' = 1/3$ shows a qualitatively different behavior when compared to the t–J model. The shape of the susceptibility seems to remain similar to that of an antiferromagnet for all dopings as shown in Fig. 5.4. As the doping is increased the peak value of the susceptibility decreases proportional to the doping and the temperature at which the peak occurs gradually increases. This agrees well with the fact that a robust antiferromagnetism is observed for the electron–doped cuprates.

In contrast the susceptibility of the hole–doped t–t'–J model represented by $t' = -1/3$ does not retain its shape for any value of the doping as shown in Fig. 5.5. It is strongly enhanced for any value of the doping and no antiferromagnetic peak can be resolved for any value of the doping. To examine this in more detail, we study $S(\mathbf{0})$ for $\rho = 0.80$ and $t' = -1/3$ in Fig. 5.6. $S(\mathbf{0})$ remains flat for the whole temperature range accessible although its value is reduced from the high–temperature value. It is important to note that the poles of the Padé approximants do not indicate any low–temperature divergence of $S(\mathbf{0})$ corre-

sponding to true ferromagnetism. That the hole–doped system does not show an antiferromagnetic peak at all would be a premature conclusion. However if the hole–doped system becomes antiferromagnetic for any of the dopings considered here, it has to happen on a very small temperature scale when compared to the t–J model and a higher–order series would be required to resolve such a feature. We will return to the fact that the hole–doped t–t'–J model seems to acquire a small energy scale especially when compared to the electron–doped system later.

To conclude Fig. 5.7 compares the susceptibility at $\rho = 0.80$ for different values of the next–nearest neighbor hopping t'. It clearly shows that antiferromagnetism is strongly enhanced or suppressed as a function of the next–nearest neighbor hopping t', and although the $t' = -1/3$ result is consistent with the susceptibility of a free spin we have discussed, that this may be interpreted as a suppression of the energy scale of antiferromagnetism below our resolution. In this context it is important to consider the possibility, that if a variable transformation such as the linear transformation is used, the result might seem well converged to extremely low temperatures as in Fig. 5.6, although the approximant has simply saturated after using all available information, and would change qualitatively if the series was known to higher order.

5.4 The magnetic structure factor $S(\mathbf{q})$

A more detailed picture of the magnetic excitations in the system can be obtained by studying the magnetic structure factor $S(\mathbf{q})$. Figures 5.8–5.14 show the result of the analysis of $S(\mathbf{q})$ for different values of the parameters and temperatures $T = 2t$, t, $t/3$, and $t/6$. An exception is the electron–doped t–t'–J model for which reliable results for $S(\mathbf{q})$ can only be obtained down to temperatures $T \sim J = t/3$ using our series. Therefore we plot the results for $t' = 1/3$ only in comparison to the results for $t' = 0$ and $t' = -1/3$ at $T = t/2$. We study $S(\mathbf{q})$ along the path $\mathbf{0} \rightarrow \mathbf{Q} \rightarrow \mathrm{M} = (\pi, 0) \rightarrow \mathbf{0}$ in the Brillouin zone.

Figure 5.8 shows $S(\mathbf{q})$ of the spin–1/2 Heisenberg antiferromagnet. At high temperatures $S(\mathbf{q})$ is flat. As the temperature is lowered, $S(\mathbf{q})$ becomes more structured and develops a delta peak at the antiferromagnetic ordering vector indicating antiferromagnetic long–range order. Its $\mathbf{q}$–dependence going from $\mathbf{0}$ to

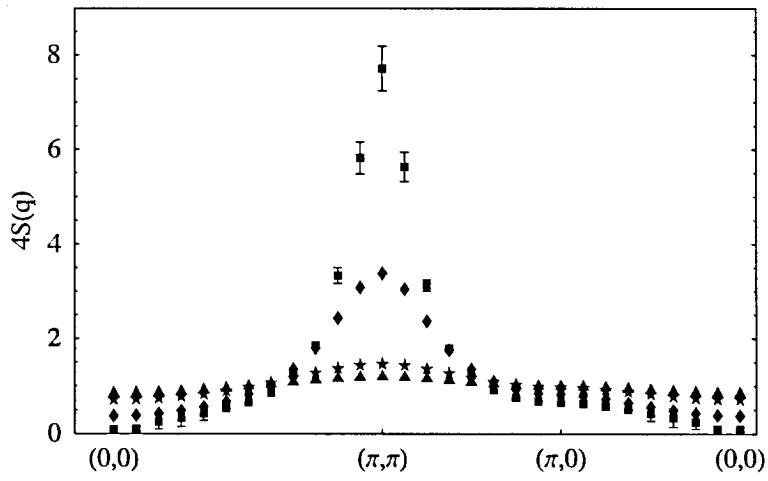

Figure 5.8: $S(\mathbf{q})$ of the spin–1/2 Heisenberg antiferromagnet on a square lattice for $J = 1/3$ ($t = 1$) and temperatures $T = 2t$ (stars), t (triangles), $t/3$ (diamonds), $t/6$ (squares). Error bars are only shown for the lowest temperature.

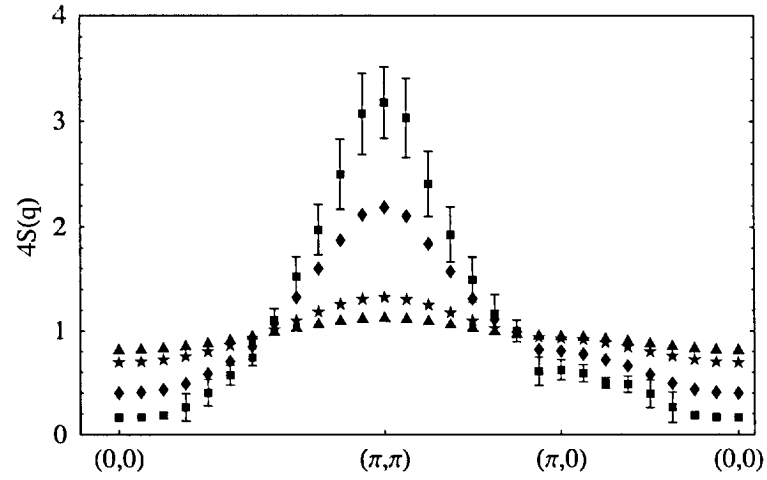

Figure 5.9: $S(\mathbf{q})$ of the t–t'–J model for $t' = 0$ and $\rho = 0.95$ ($t = 1$, $J = 1/3$) for temperatures $T = 2t$ (stars), t (triangles), $t/3$ (diamonds), $t/6$ (squares). Error bars are only shown for the lowest temperature.

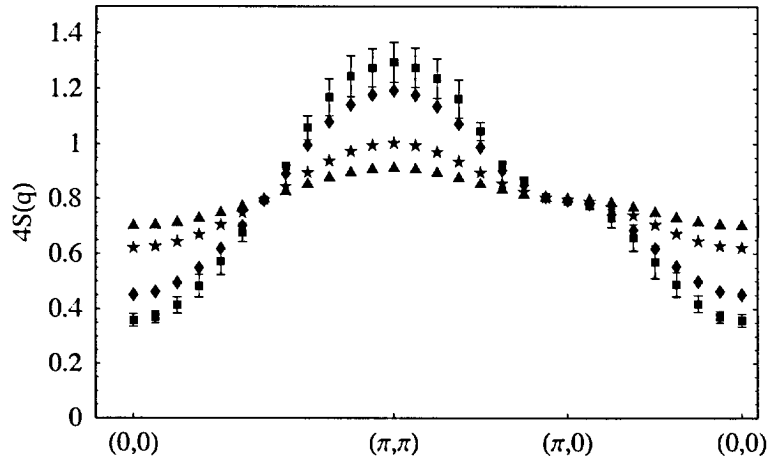

Figure 5.10: $S(\mathbf{q})$ of the t–t'–J model for $t' = 0$ and $\rho = 0.80$ ($t = 1$, $J = 1/3$) for temperatures $T = 2t$ (stars), t (triangles), $t/3$ (diamonds), $t/6$ (squares). Error bars are only shown for the lowest temperature.

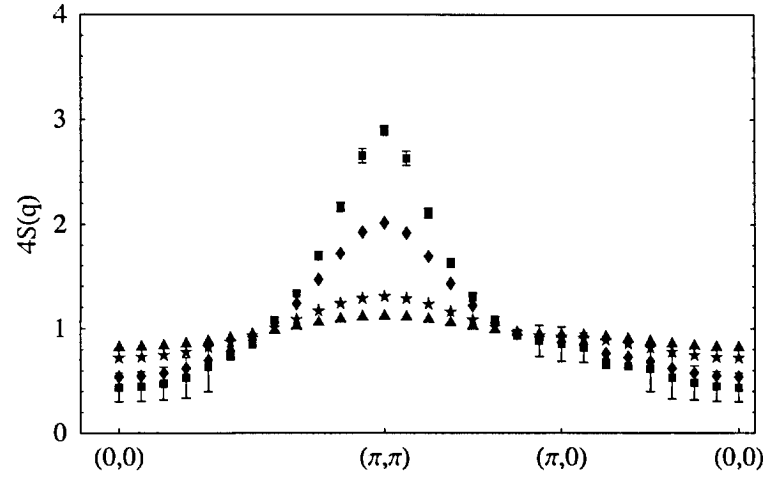

Figure 5.11: $S(\mathbf{q})$ of the t–t'–J model for $t' = -1/3$ and $\rho = 0.95$ ($t = 1$, $J = 1/3$) for temperatures $T = 2t$ (stars), t (triangles), $t/3$ (diamonds), $t/6$ (squares). Error bars are only shown for the lowest temperature.

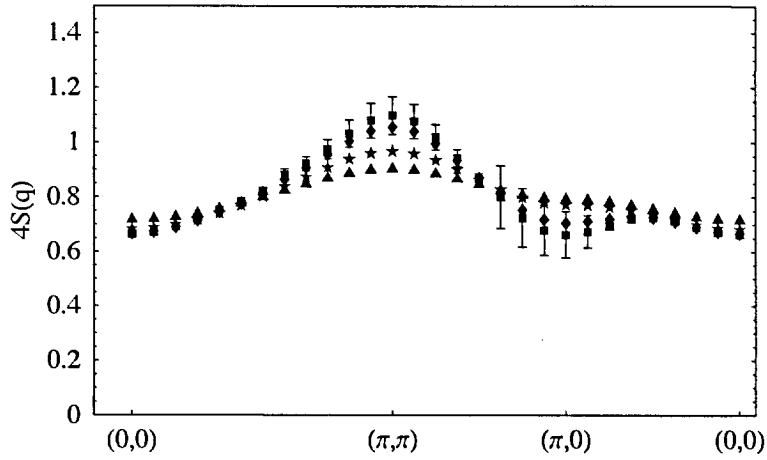

Figure 5.12: $S(\mathbf{q})$ of the t–t'–J model for $t' = -1/3$ and $\rho = 0.80$ ($t = 1$, $J = 1/3$) for temperatures $T = 2t$ (stars), t (triangles), $t/3$ (diamonds), $t/6$ (squares). Error bars are only shown for the lowest temperature.

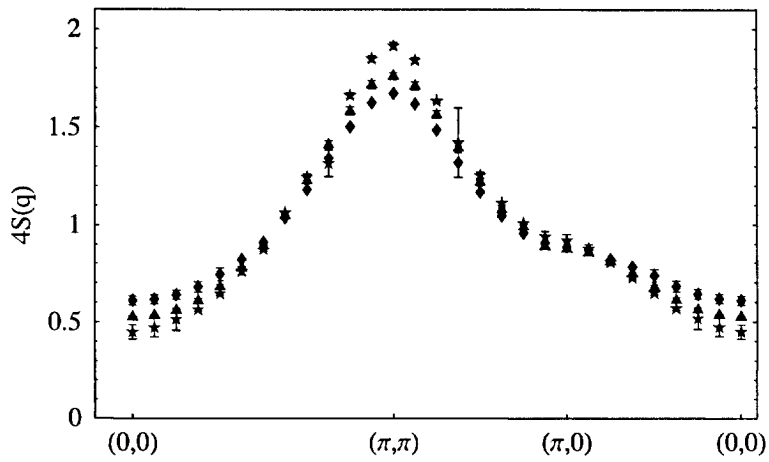

Figure 5.13: Comparison of $S(\mathbf{q})$ of the t–t'–J model for $\rho = 0.95$ ($t = 1$, $J = 1/3$) at temperature $T = t/2$ for $t' = 1/3$ (diamonds), $t' = 0$ (triangles), and $t' = -1/3$ (stars).

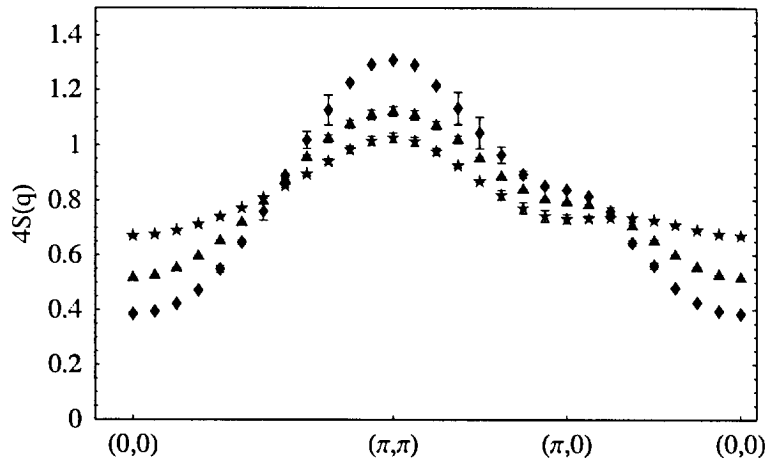

Figure 5.14: Comparison of $S(\mathbf{q})$ of the t–t'–J model for $\rho = 0.80$ ($t = 1$, $J = 1/3$) at temperature $T = t/2$ for $t' = 1/3$ (diamonds), $t' = 0$ (triangles), and $t' = -1/3$ (stars).

M is much weaker than the dependence going from M to Q, though present. As the system is weakly doped ($t' = 0$, $x = 0.05$, Figure 5.9), the height of the antiferromagnetic peak at Q weakens and broadens. Still the difference $S(\mathbf{Q}) - S(\mathbf{M})$ remains much larger than $S(\mathbf{M}) - S(\mathbf{0})$. Upon further doping ($x = 0.20$, Figure 5.10) the peak continues to broaden the differences of the magnetic structure factors $S(\mathbf{Q}) - S(\mathbf{M})$ and $S(\mathbf{M}) - S(\mathbf{0})$ have become of equal magnitude, consistent with the destruction of antiferromagnetism on these temperature scales observed in the analysis of the susceptibility.

For a next–nearest neighbor hopping $t' = -1/3$ and weak doping shown in Fig. 5.11, the shape of $S(\mathbf{q})$ is very similar to the shape observed for the t–J model at the same doping, although the features have broadened in comparison. As the doping is increased to $x = 0.20$ the magnetic structure factor has acquired a qualitatively different shape when compared to $t' = 0$. Magnetic excitation have strongly spread in the Brillouin zone as indicated by the fact that $S(\mathbf{0}) \approx S(\mathbf{M})$. Along the line from $\mathbf{0}$ to $\mathbf{M}$ the magnetic structure factor is essentially flat although a weak peak at $(\pi/2, 0)$ is visible. Due to the size of the errors at $T = t/6$ we are not able to determine if this peak is a physical feature of the model itself or an artifact of the analysis.

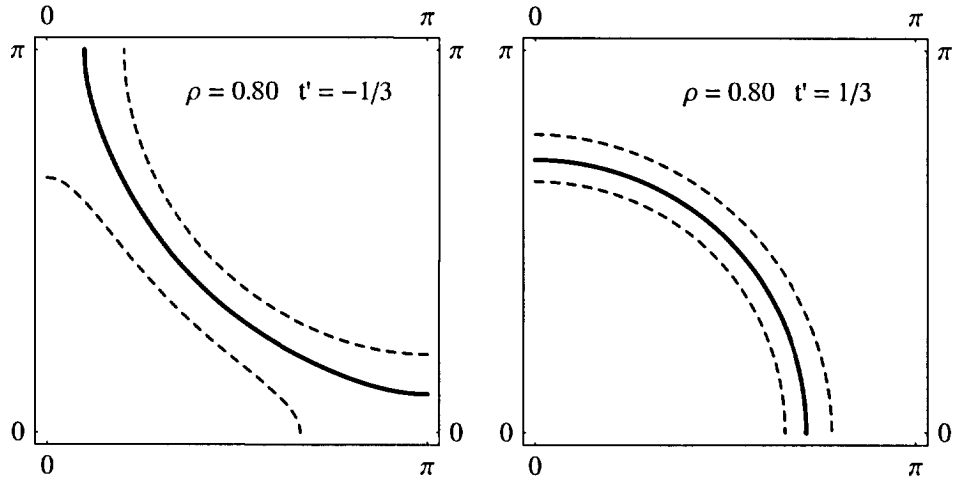

Figure 5.15: Fermi surface of a free–electron tight–binding model on a square lattice as a function of the next–nearest neighbor hopping t' at density $\rho = 0.80$ ($t = 1$). The dashed line is an estimate of the width of thermal broadening due to thermal excitations at the temperature $T = t/2$.

As already mentioned the Padé approximants to the series for a positive next–nearest neighbor hopping $t' = 1/3$ converge only down to temperatures $T \sim t/3$ in the whole Brillouin zone. Therefore we compare $S(\mathbf{q})$ at a fixed temperature $T = t/2$ for different t' and dopings $x = 0.05$ and 0.20 in Fig. 5.12 and Fig. 5.13. For both values of the doping a positive t' enhances antiferromagnetic correlations without changing the structure of $S(\mathbf{q})$ significantly from the case of $t' = 0$ consistent with our observations for the susceptibility.

5.5 The momentum distribution function $n(\mathbf{q})$

We now study the momentum distribution function $n(\mathbf{q})$ of the t–t'–J model. For a system of free electrons with a dispersion relation $\epsilon_{\mathbf{q}}$ such as a tight–binding model, $n(\mathbf{q})$ is given by the Fermi–distribution

$$n(\mathbf{q}) = \frac{e^{-\beta(\epsilon_{\mathbf{q}}-\mu)}}{1+e^{-\beta(\epsilon_{\mathbf{q}}-\mu)}}. \tag{5.10}$$

The chemical potential μ is chosen so that the density of particles in the system is equal to ρ. The Fermi energy ϵ_F is defined to be the zero temperature chemical

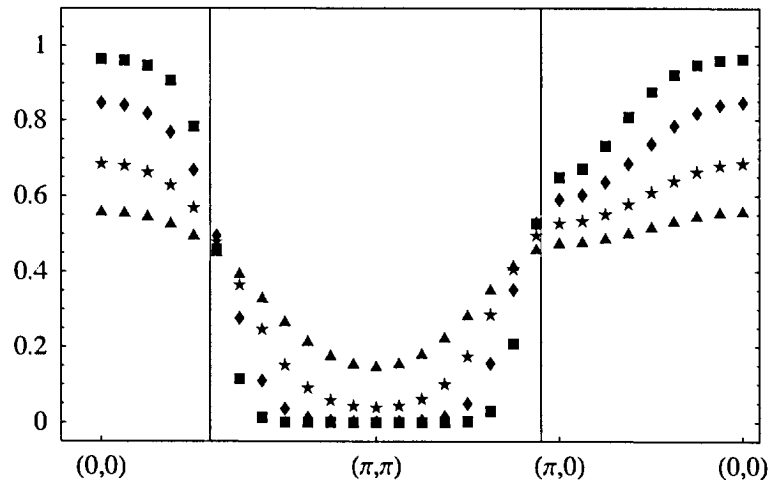

Figure 5.16: Plot of the momentum distribution function $n(\mathbf{q})$ for a tight–binding model with $\rho = 0.80$, $t = 1$, and $t' = -1/3$ for temperatures $T = 4t$ (triangles), $2t$ (stars), t (diamonds), and $t/2$ (squares). The vertical lines denote the location of the Fermi surface.

potential, and we denote by $q < q_F$ all momentum vectors $\mathbf{q}$ with an energy $\epsilon_{\mathbf{q}}$ smaller than the Fermi energy. q_F is called the Fermi momentum and its magnitude depends on the direction considered. At at zero temperature $n(\mathbf{q}) = 1$ if $q < q_F$ and $n(\mathbf{q}) = 0$ if $q > q_F$. For finite temperatures the Fermi step is smeared out on an energy scale $\sim k_B T$. Figure 5.15 shows the Fermi surface of a tight–binding model with nearest and next–nearest neighbor hopping for different values of the next–nearest neighbor hopping t' and Fig. 5.16 the momentum distribution function for $\rho = 0.80$ and $t' = -1/3$ ($t = 1$). Starting from an essentially flat $n(\mathbf{q}) = \rho/2$ at very high temperatures, $n(\mathbf{q})$ drops to zero fast outside of the Fermi surface shown by the lines the momentum distribution while it increases within the Fermi surface.

Interactions in a Fermi liquid renormalize the momentum distribution function. If Fermi–liquid theory is applicable to the interacting system then the momentum distribution function acquires an incoherent background and the Fermi step is renormalized to a height $Z_{\mathbf{q}}$, where $Z_{\mathbf{q}}$ is called the quasiparticle weight of an excitation in the system with momentum $\mathbf{q}$. Furthermore, if Fermi theory is applicable to an interacting Fermi system, then the volume enclosed by the Fermi surface is conserved, a fact known as Luttingers theorem. As the existence of a

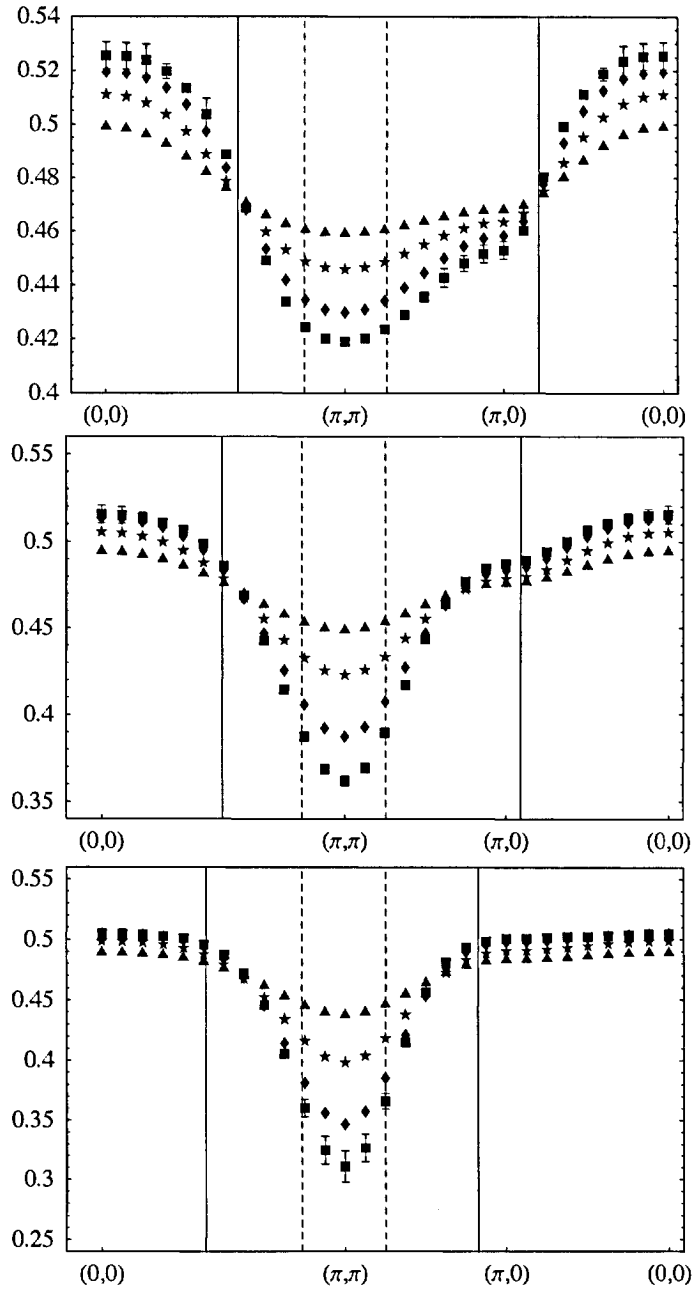

Figure 5.17: Plot of the momentum distribution function $n(\mathbf{q})$ at $\rho = 0.95$ for next–nearest neighbor hopping parameters $t' = 1/3$ (top), $t' = 0$ (middle), and $t' = -1/3$ (bottom). The data points shown are for temperatures $T = 4t$ (triangles), $2t$ (stars), t (diamonds), and $t/2$ (squares). The vertical solid (dashed) lines are the Fermi surface of a system of tight–binding electrons (spinless fermions) with the same parameters.

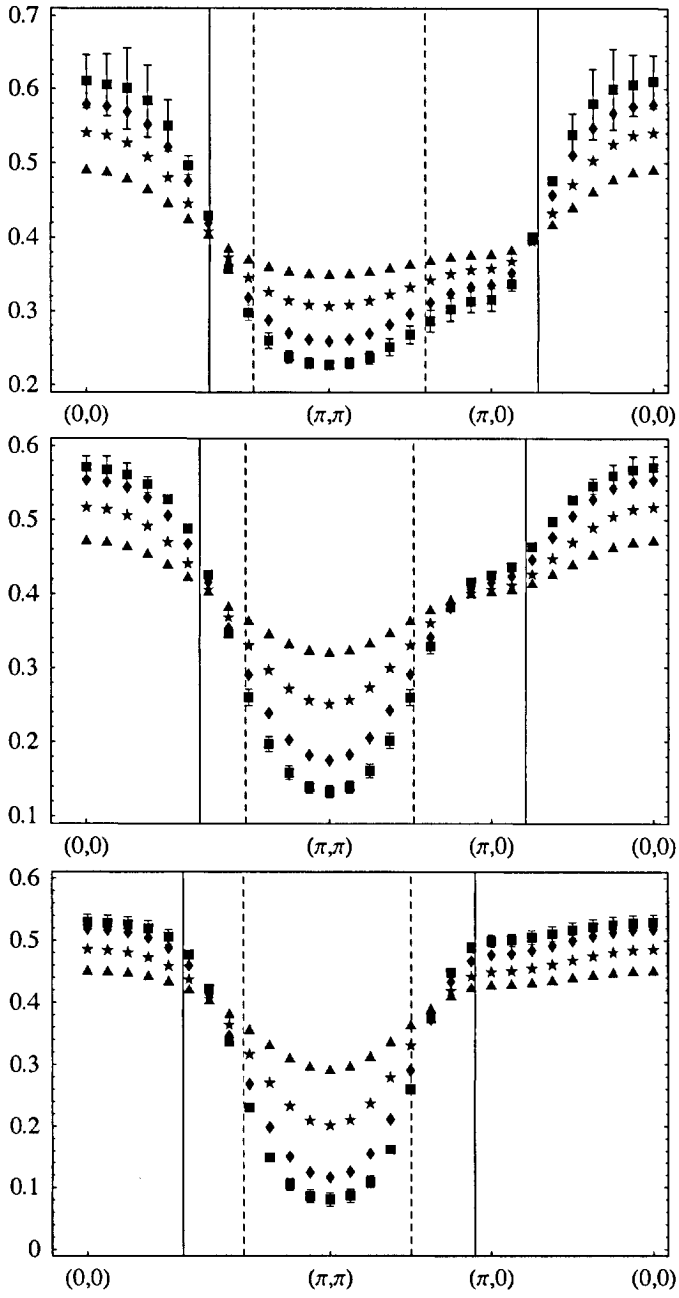

Figure 5.18: Plot of the momentum distribution function $n(\mathbf{q})$ at $\rho = 0.80$ for next–nearest neighbor hopping parameters $t' = 1/3$ (top), $t' = 0$ (middle), and $t' = -1/3$ (bottom). The data points shown are for temperatures $T = 4t$ (triangles), $2t$ (stars), t (diamonds), and $t/2$ (squares). The vertical solid (dashed) lines are the Fermi surface of a system of tight–binding electrons (spinless fermions) with the same parameters.

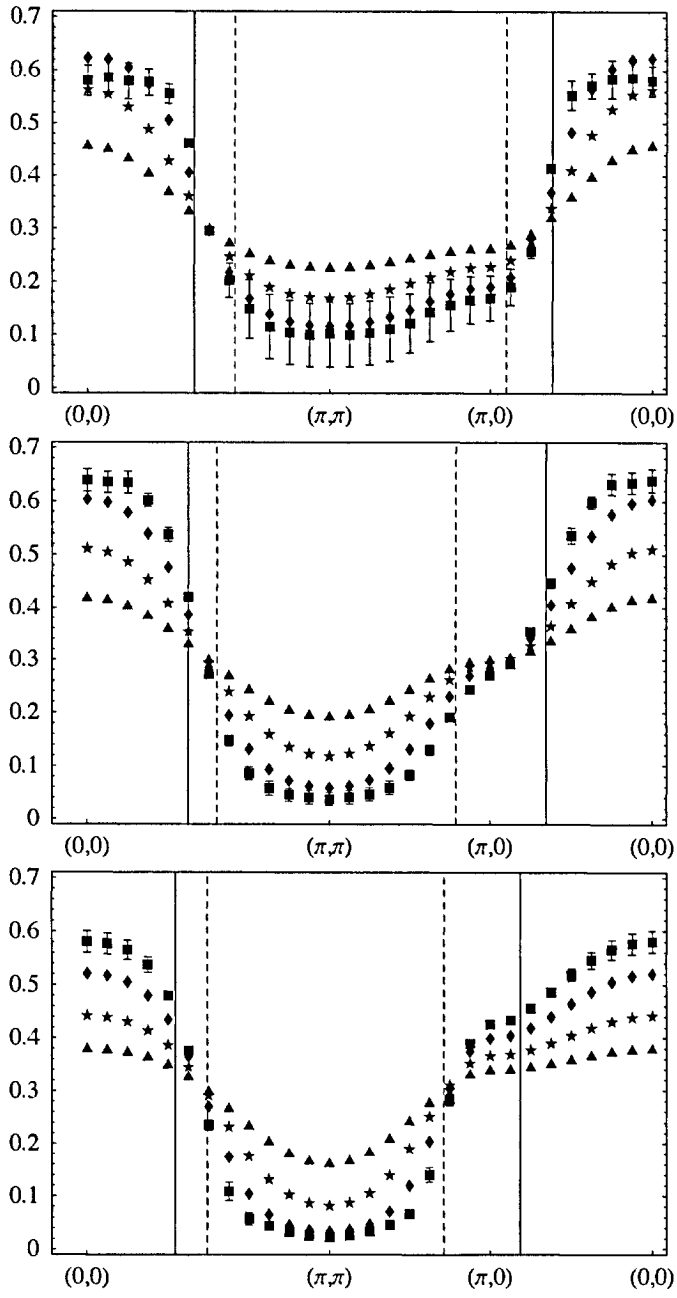

Figure 5.19: Plot of the momentum distribution function $n(\mathbf{q})$ at $\rho = 0.60$ for next–nearest neighbor hopping parameters $t' = 1/3$ (top), $t' = 0$ (middle), and $t' = -1/3$ (bottom). The data points shown are for temperatures $T = 4t$ (triangles), $2t$ (stars), t (diamonds), and $t/2$ (squares). The vertical solid (dashed) lines are the Fermi surface of a system of tight–binding electrons (spinless fermions) with the same parameters.

Fermi surface is a zero temperature property, it is not directly accessible by a high–temperature series expansion. If we assume that the features of $n(\mathbf{q})$ are only smeared out due to thermal excitations in the system, we can however try to infer the Fermi surface and its location by using different criteria at finite temperatures. One criterion is that $n(q_F) = 1/2$ for a system with particle–hole symmetry. Although the t–t'–J model is not particle–hole symmetric, the criterion has been used before in Ref. [57] and other studies. Another criterion is the fact that the quasiparticle step at the Fermi surface leads to a large gradient $|\nabla n(\mathbf{q})|$ for low temperatures, and a third criterion proposed by Randeria *et al.* [58] is that $dn(\mathbf{q})/dT = 0$ on the Fermi surface. We start be examining $n(\mathbf{q})$ along the path $\mathbf{0} \rightarrow \mathbf{Q} \rightarrow \mathbf{M} \rightarrow \mathbf{0}$ as for the magnetic structure factor $S(\mathbf{q})$. Furthermore we assume for the moment that a Fermi surface is present to simplify the discussion of the results, and later discuss this issue in more detail.

Figures 5.17, 5.18, and 5.19 show the momentum distribution function for densities $\rho = 0.95$, 0.80, and 0.60 and next–nearest neighbor hopping values $t' = 1/3$, 0, and $-1/3$. For very high temperatures $n(\mathbf{q})$ is constant and equal to $\rho/2$, and as the temperature is lowered the momentum distribution function develops a $\mathbf{q}$ dependence. In all plots the Fermi surface of tight–binding electrons using the same hopping parameters is shown as a solid vertical line, while the Fermi surface of tight–binding spinless fermions using the same hopping parameters is shown as a dashed vertical line. For the density $\rho = 0.95$ shown in Fig. 5.17 the momentum distribution function has a strong incoherent background. For $t' = 1/3$ a momentum dependence is present in the whole Brillouin zone and the gradient and the change of $n(\mathbf{q})$ as the temperature is lowered indicate a Fermi surface compatible with that of a free–electron system. As t' becomes smaller the momentum dependence of $n(\mathbf{q})$ along the line from $\mathbf{0}$ to $\mathbf{M}$ nearly completely vanishes. For $t' = -1/3$ the maximum of the gradient has been pushed out far and the system does not show any features at the Fermi surface of the corresponding free–electron system. The flattening seems to be due to spectral weight that is transferred from $\mathbf{Q}$ to the surrounding region. Higher densities confirm this general picture. The features of the momentum distribution function of the electron–doped system with $t' = 1/3$ are in general compatible with that of a free–electron system with the same parameters. This is in contrast to the hole–doped system with $t' = -1/3$. Here $n(\mathbf{q})$ increases for points outside of the free–electron Fermi surface down to temperatures of $T = t/2$.

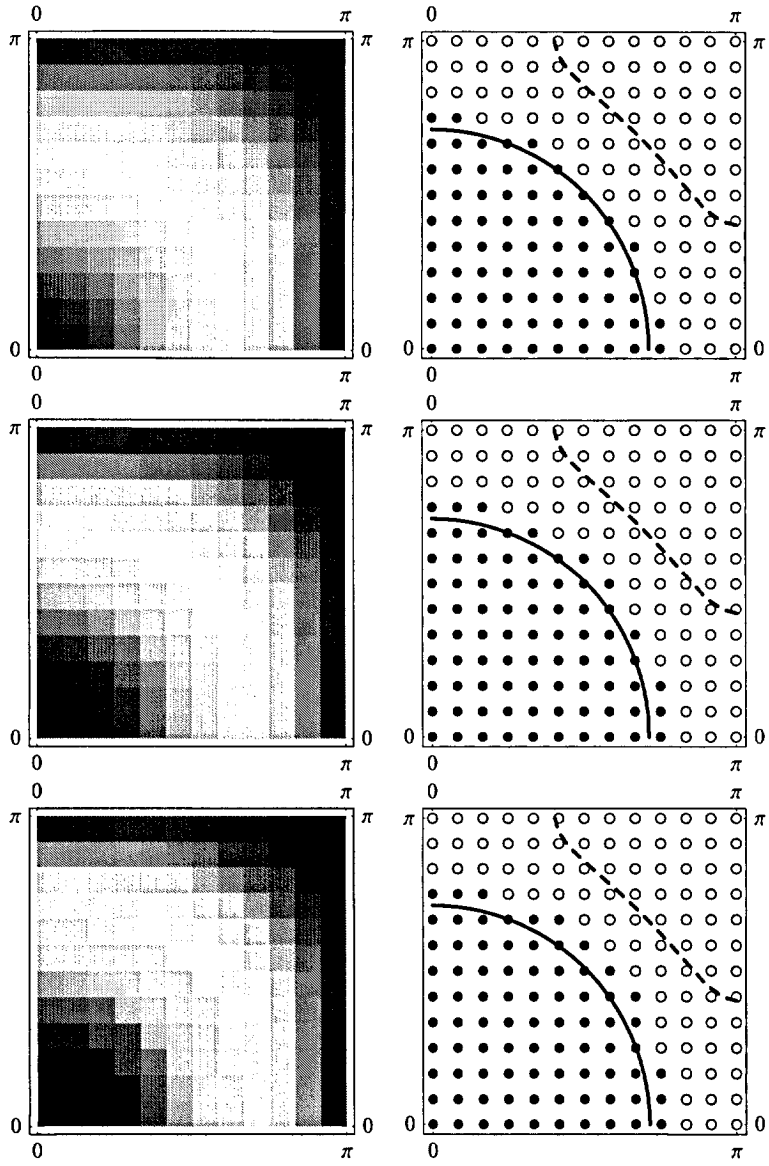

Figure 5.20: Plot of the gradient $|\nabla_{\mathbf{q}} n(\mathbf{q})|$ and the temperature derivative $dn(\mathbf{q})/dT$ for temperatures $T = 2$ (top), $T = 1$ (middle), and $T = 1/2$ (bottom) for parameters $\rho = 0.80$ and $t' = 1/3$. The gradient on the left hand side is plotted in arbitrary units. On the right hand site a filled circle denotes a point with $dn(\mathbf{q})/dT < 0$ while an open circle denotes a point with $dn(\mathbf{q})/dT > 0$. The solid line (dashed) is a plot of the Fermi surface of a free electron (free spinless fermion) system using the same parameters.

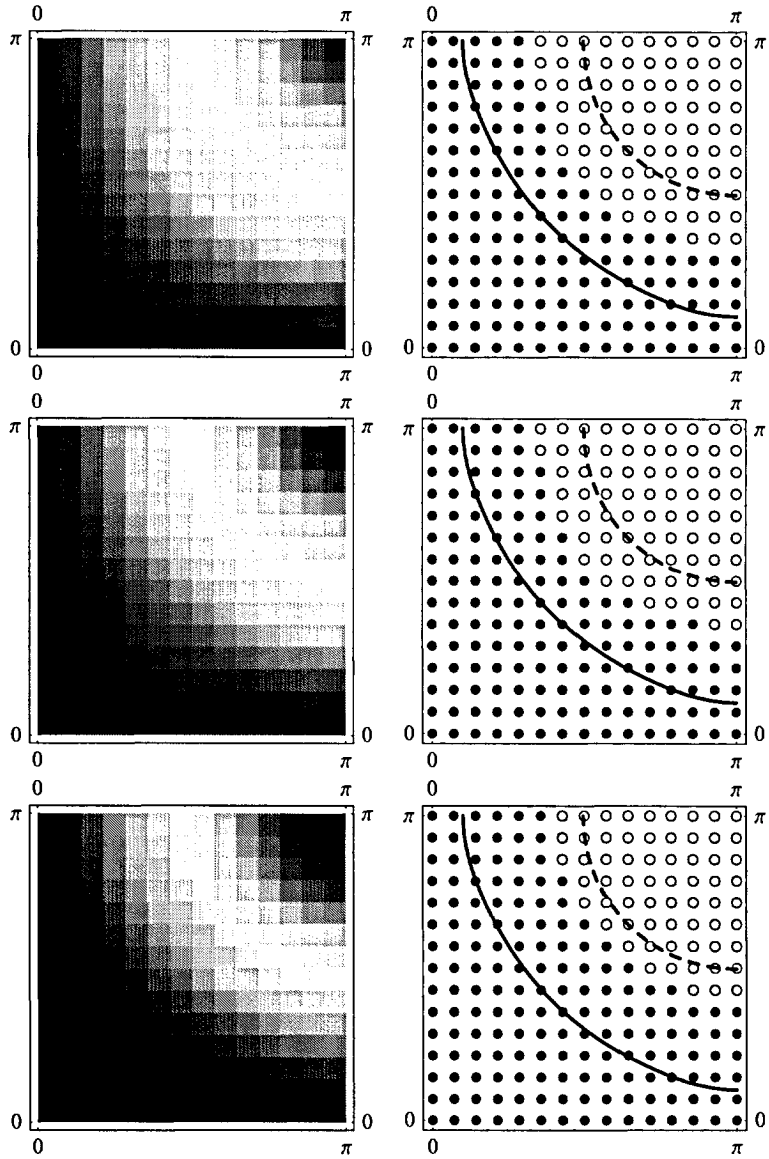

Figure 5.21: Plot of the gradient $|\nabla_{\mathbf{q}} n(\mathbf{q})|$ and the temperature derivative $dn(\mathbf{q})/dT$ for temperatures $T = 2$ (top), $T = 1$ (middle), and $T = 1/2$ (bottom) for parameters $\rho = 0.80$ and $t' = -1/3$. The gradient on the left hand side is plotted in arbitrary units. On the right hand site a filled circle denotes a point with $dn(\mathbf{q})/dT < 0$ while an open circle denotes a point with $dn(\mathbf{q})/dT > 0$. The solid line (dashed) is a plot of the Fermi surface of a free electron (free spinless fermion) system using the same parameters.

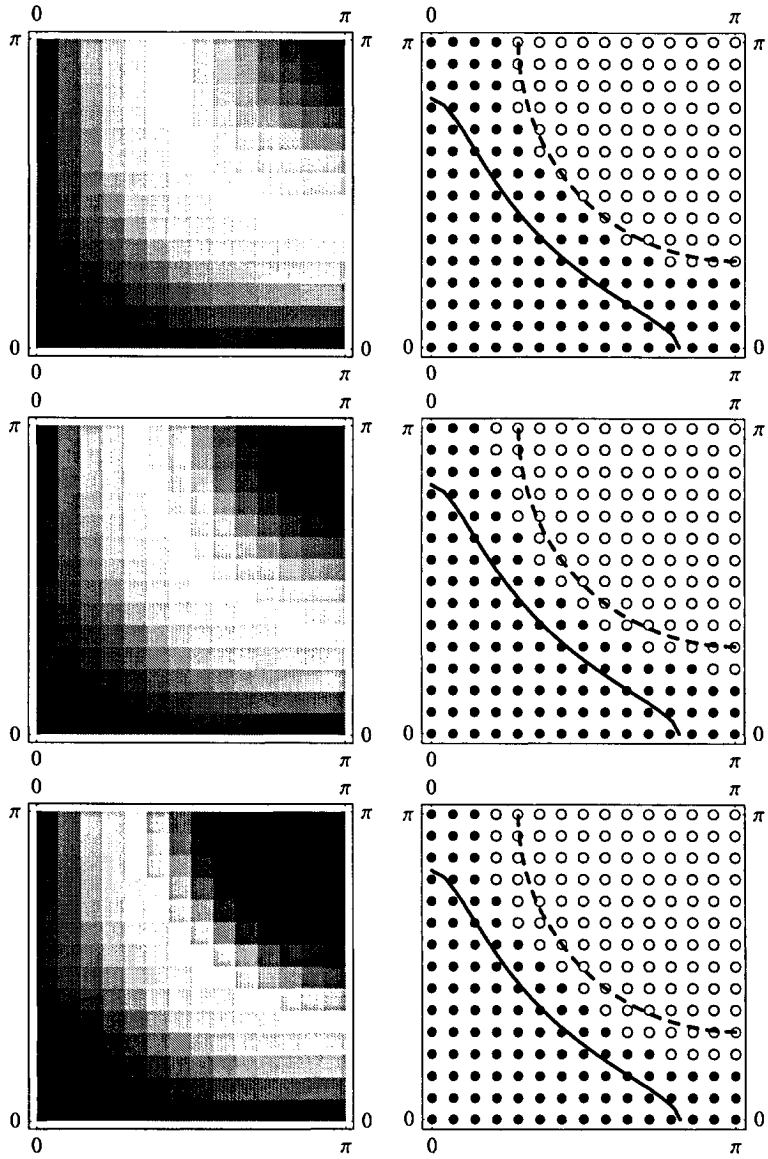

Figure 5.22: Plot of the gradient $|\nabla_{\mathbf{q}} n(\mathbf{q})|$ and the temperature derivative $dn(\mathbf{q})/dT$ for temperatures $T = 2$ (top), $T = 1$ (middle), and $T = 1/2$ (bottom) for parameters $\rho = 0.60$ and $t' = -1/3$. The gradient on the left hand side is plotted in arbitrary units. On the right hand site a filled circle denotes a point with $dn(\mathbf{q})/dT < 0$ while an open circle denotes a point with $dn(\mathbf{q})/dT > 0$. The solid line (dashed) is a plot of the Fermi surface of a free electron (free spinless fermion) system using the same parameters.

To study this behavior in more detail Fig. 5.20, 5.21, and 5.22 show the gradient $|\nabla_{\mathbf{q}} n(\mathbf{q})|$ and the temperature derivative $dn(\mathbf{q})/dT$ for different temperatures. $|\nabla_{\mathbf{q}} n(\mathbf{q})|$ and $dn(\mathbf{q})/dT$ are both calculated as finite differences. Figure 5.20 confirms that the Fermi surface inferred from finite–temperature criteria agrees well with the Fermi surface of a free–electron system with the same hopping parameters for the electron–doped system. Thus a violation of Luttingers theorem as observed in [21] is not an inherent feature of the t–t'–J model due to the projection that is present in the whole parameter range. For the hole–doped system the situation as shown in Fig. 5.21 and Fig. 5.22 is different. The maximum of the gradient seems to be frozen closer to the Fermi surface that one would expect for a system of free spinless fermions. This would be expected, if the system became ferromagnetic but as we discussed, the susceptibility does not indicate any ferromagnetism on the temperature scales considered here. In addition the temperature derivative indicates a Fermi surface that is considerably larger than that of the free–electron system.

5.6 Discussion

As already mentioned, one has to be careful when interpreting the low–temperature behavior obtained from approximants to a series after a linear transformation, or for that matter any other transformation that maps the inverse temperature interval to a compact interval. Although approximants may seem well converged, it can be the limited order of a series that prevents us from extracting features occurring at low–energy scales. Two subjects of interest of this study were the asymmetry of the phase diagram of the cuprates with respect to electron– and hole–doping and the study of the Fermi surface — if present — using finite–temperature criteria.

Our results clearly show that the behavior of the t–t'–J model is asymmetric with respect to a change in t', corresponding to electron– or hole–doping. We observe an enhancement of antiferromagnetism for a positive next–nearest neighbor hopping, consistent with experimental findings, and a Fermi surface that is within our resolution identical to that of free electrons with the same hopping parameters, consistent with experimental findings for moderate to large doping.

This stands in contrast to the behavior of the t–t'–J model for a negative next–nearest neighbor hopping. Here the susceptibility of the system is enhanced and we are unable to resolve any antiferromagnetic peak in the susceptibility. Furthermore the Fermi surface as inferred from finite–temperature criteria is far from the Fermi surface of a free–electron system with the same hopping parameters. While such a behavior could be interpreted as a violation of Luttingers theorem done by Putikka *et al.* [21]. As we were unable to find any violation of Luttingers theorem for positive t', we propose an alternative explanation. Before we mention that we are unable to find any violation of Luttingers theorem, when we apply our analysis and the $dn(\mathbf{q})/dT = 0$ criterion to the 12th–order series of $n(\mathbf{q})$ calculated by Putikka *et al.* The interpretation that we propose is that our results for negative t' are consistent with flat bands close to $\mathbf{M}$ and a weak dispersion along the line from 0 to $\mathbf{M}$ in general, as discussed in Ref. [59, 60]. This flat dispersion leads to a flat magnetic structure factor and a flat momentum distribution along this line. Furthermore any antiferromagnetic ordering is shifted to temperatures below our resolution. Given our results it is unclear if the antiferromagnetic ordering or another instability related to the pseudogap has a stronger influence on the system in this parameter region. In addition we note that the behavior of the t–t'–J model for $t' = -1/3$ is qualitatively different than that of the t–J model. Also we were unable to find any indications of the formation of hole pockets in our results.


Seite Leer /
Blank leaf

Chapter 6

Cluster updates and multicanonical simulations

Since the introduction of importance sampling to the simulation of thermodynamic systems by Metropolis *et. al.* [61] in 1953, Monte Carlo simulations have developed into an indispensable tool for the study of classical and quantum mechanical systems. Advances such as the development of cluster algorithms [62, 63] and multicanonical ensemble simulations [64, 65] have made Monte Carlo simulations the most efficient method available for many systems of interest. The recent development of the Wang–Landau algorithm [66, 67], a simple and scalable implementation of a multicanonical ensemble Monte Carlo simulation, has led to a renewed interest in combining multicanonical ensemble simulations with cluster updates to improve the performance of multicanonical ensemble simulations [68, 69, 70]. Cluster updates have previously been used in multicanonical ensemble simulations of Ising and Potts models [71], but not of continuous spin models, although cluster algorithms for canonical ensemble simulations of these models are known.

In this chapter we demonstrate how cluster updates can be implemented in a multicanonical ensemble simulation of a continuous spin model. To do so, a different representation of the partition function of the system has to be used, and although this representation is not directly related to the connected cluster expansion as introduced in chapter 2, many of the ideas developed in chapter 2 such as the multivariable expansion of a thermodynamic property and the subsequent

identification of the terms in the expansion with multigraphs, have strongly influenced the development of this new algorithm. We start by discussing why Monte Carlo simulations are used to study classical spin systems and give an overview over the problems that different Monte Carlo simulation methods encounter. We discuss which problems are solved by the canonical cluster algorithms and by multicanonical ensemble simulations and then show how they can be combined for a continuous spin system. To simplify the presentation we restrict ourselves to ferromagnetic Ising, Potts [72], and $O(n)$ models although the algorithm can in principle be applied to any other classical lattice system for which a canonical cluster algorithm exists.

6.1 Classical spin models

The Hamiltonian of the ferromagnetic Ising, Potts, and $O(n)$ model on a lattice can be written in the form

$$H[\sigma] = -\sum_{\langle ij \rangle} h_{ij}[\sigma_i, \sigma_j], \tag{6.1}$$

where σ is the configuration of the system, the sum is over all edges $\langle ij \rangle$ of the lattice, and the minus sign is chosen for convenience. For the $O(n)$ model the configuration of the system is given by vectors $\sigma_i \in S_{n-1} = \{x \in \mathbb{R}^n : |x| = 1\}$ of unit length located on the sites of the lattice which interact with an $O(n)$–symmetric exchange

$$h_{ij}[\sigma_i, \sigma_j] = \sigma_i \cdot \sigma_j. \tag{6.2}$$

The $O(1)$ model with $\sigma_i = \pm 1$ and $h_{ij}[\sigma_i, \sigma_j] = \sigma_i \sigma_j$ is also called the Ising model. The configuration of the q–state Potts model is given by an integer number $\sigma_i \in \{1, \ldots, q\}$ at each site of the lattice with an exchange term

$$h_{ij}[\sigma_i, \sigma_j] = \delta_{\sigma_i, \sigma_j}. \tag{6.3}$$

The two–state Potts model with a shifted and rescaled energy is also equivalent to the Ising model. In the canonical ensemble the probability that the system has the configuration σ is given by the Boltzmann distribution [26]

$$p(\sigma) = \frac{\exp\left(-\beta H[\sigma]\right)}{\sum_\sigma \exp\left(-\beta H[\sigma]\right)}, \tag{6.4}$$

where $\beta = 1/k_B T$ is the inverse temperature and we set $k_B = 1$ for the rest of this chapter. The thermodynamic average of a function $A(\sigma)$ is defined by

$$\langle A(\sigma) \rangle = \sum_{\sigma} A(\sigma)\, p(\sigma). \tag{6.5}$$

The sums in Eq. (6.4) and Eq. (6.5) are over all possible configurations of the system and have to be read as integrals $\int d\sigma$ for continuous degrees of freedom. Examples of thermodynamic averages in the canonical ensemble are the internal energy $U = \langle H[\sigma] \rangle$ and the specific heat $C_V = \beta^2 \left(\langle H[\sigma]^2 \rangle - \langle H[\sigma] \rangle^2 \right)$. The canonical probability distribution $p(\sigma)$ defined in Eq. (6.4) and other probability distributions in this chapter are often more conveniently defined by weights $W(\sigma)$, which in the case of the canonical ensemble is the Boltzmann weight $W(\sigma) \propto \exp(-\beta H[\sigma])$. The weights define the probability distribution via the relation $p(\sigma) = W(\sigma)/Z$, and the partition function

$$Z = \sum_{\sigma} W(\sigma) \tag{6.6}$$

acts as a the normalization factor of the probability distribution. Z can be a useful tool to keep track of the states of the system when transformations are applied to the configuration space. We later refer to Eq. (6.6) as the partition function in the spin representation to distinguish it from other representations that we introduce. The weight of a configuration only depends on its energy, and it is natural to define the density of states in the spin representation by

$$g_\sigma(E) = \sum_{\sigma} \delta(E - H[\sigma]). \tag{6.7}$$

The density of states in the spin representation is a function of the energy and counts the number of configurations with a certain energy E. Using the density of states Eq. (6.6) simplifies to

$$Z = \sum_{E} g_\sigma(E)\, \exp(-\beta E), \tag{6.8}$$

and the thermodynamic average of a function that depends on the energy of a configuration only can be written as

$$\langle A(E) \rangle = \sum_{E} A(E)\, \frac{g_\sigma(E)\, \exp(-\beta E)}{Z}. \tag{6.9}$$

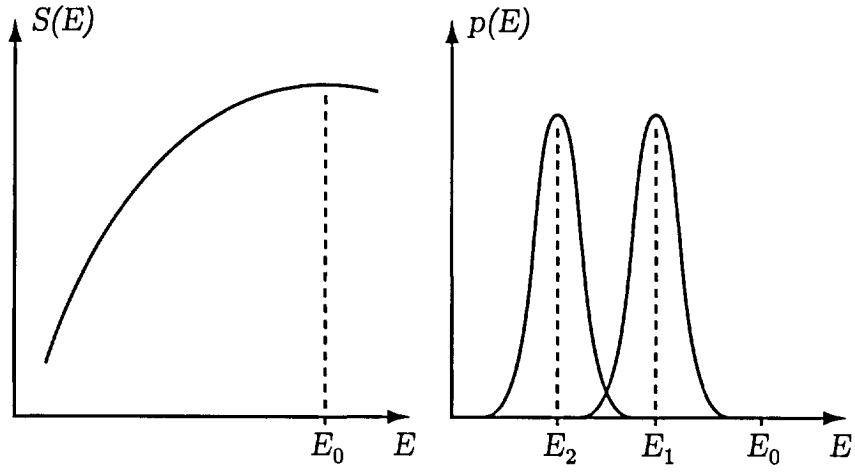

Figure 6.1: *Left:* Sketch of the entropy of a system without a phase transition in the energy range shown. The slope of the entropy is the microcanonical temperature. E_0 corresponds to $T = \infty$. *Right:* Corresponding energy distributions in the canonical ensemble for two different temperatures $T_2 < T_1$ and the average energies E_1 and E_2 at these temperatures.

The density of states also defines the microcanonical entropy of the system by [26]

$$S(E) = \ln\left(g_\sigma(E)\right). \tag{6.10}$$

In practice neither the thermodynamic averages defined in Eq. (6.5) and Eq. (6.9), nor the entropy defined in Eq. (6.10) can be calculated exactly for most systems, so that either approximations or computer simulations have to be used to study such a system.

6.2 Monte Carlo simulations

The idea of a Monte Carlo (MC) simulation is to replace the sum over all configurations in Eq. (6.5) by a sum over N "representative" configurations $\sigma(i)$ $(i = 1, \ldots, N)$ chosen in a random fashion. If the configurations $\sigma(i)$ are selected independently and uniformly distributed in the configuration space, we speak of a simple sampling Monte Carlo simulation. In a simple sampling Monte Carlo simulation the thermodynamic average as defined in Eq. (6.5) can be estimated

by

$$\langle A(\sigma)\rangle \approx \frac{\sum_{i=1}^{N} A(H[\sigma(i)])\,\exp(-\beta H[\sigma(i)])}{\sum_{i=1}^{N}\exp(-\beta H[\sigma(i)])}. \tag{6.11}$$

That this is not an efficient method to sample the configuration space can be seen from the following argument: The left hand side of Fig. 6.1 sketches the behavior of the entropy of a physical system (we assume that the system has no phase transition in the energy range shown). In a simple sampling simulation configurations are selected with equal probability and therefore a configuration with energy E is selected with a probability proportional to $g_\sigma(E)$. Thus configurations with an energy that corresponds to a maximum in the density of states $g_\sigma(E)$ and thereby the entropy $S(E)$ are most likely to be chosen. The maximum of $S(E)$ satisfies the condition $dS(E)/dE = 0$, but $dS(E)/dE$ is on the other hand the inverse temperature β of the system in the microcanonical ensemble. This implies that the simple sampling algorithm samples mostly configurations that are relevant at very high temperatures, which rarely is the temperature region of interest. From the standpoint of the canonical ensemble, the probability that the system has a configuration with energy E is proportional to

$$g_\sigma(E)\exp(-\beta E). \tag{6.12}$$

This distribution has a well defined maximum close to $\langle E\rangle$ with a width of $\sqrt{C_V}/\beta$ for each temperature β, unless there is a phase transition and C_V diverges. This maximum depends on the temperature and the simple sampling algorithm will only be efficient if $\langle E\rangle$ is close to $E_0 = \langle E\rangle_{\beta=0}$, consistent with the microcanonical view. This behavior of the canonical probability distribution is sketched on the right hand side of Fig. 6.1 for two different temperatures $T_1 < T_2 < \infty$.

6.2.1 Importance sampling

The discussion of the simple sampling algorithm in the previous section suggests that the efficiency of the algorithm can be improved if the configurations are selected with their canonical probability (6.4). This is known as importance sampling. It is in general not possible to efficiently draw *independent* configurations from a given probability distribution $p(\sigma)$. Metropolis *et. al.* [61] solved this problem by sampling the configuration space of the system with a sequence of configurations generated by a Markov chain. A Markov chain Monte Carlo

simulation generates a sequence of configurations $\sigma(i)$ with the help of a time independent transition matrix $T(\sigma \to \sigma')$. If the configuration of the Markov chain is $\sigma(i) = \sigma$ at time i, then $T(\sigma \to \sigma')$ is the probability, that $\sigma(i+1) = \sigma'$ is the next configuration. The transition matrix $T(\sigma \to \sigma')$ is a mathematical representation of the algorithm used in the simulation, and before we discuss the general algorithm introduced by Metropolis *et. al.*, we present the central result on which the use of Markov chain Monte Carlo simulations to draw samples from a probability distribution $p(\sigma)$ is based:

> CONVERGENCE THEOREM: If the algorithm specified by $T(\sigma \to \sigma')$ is *ergodic*, that is any state can be reached from any other state in a finite number of steps, and satisfies the *detailed balance* condition
>
> $$p(\sigma)\, T(\sigma \to \sigma') = p(\sigma')\, T(\sigma' \to \sigma), \tag{6.13}$$
>
> then the probability distribution of the $\sigma(i)$ generated by the Markov chain converges to $p(\sigma)$ as $t \to \infty$.

A rigorous yet accessible proof of this result can be be found in [73] and the references therein. As a consequence the thermodynamic average (6.5) can be written as an average over the Monte Carlo time or

$$\langle A(\sigma) \rangle = \lim_{N \to \infty} \frac{1}{N} \sum_{i=1}^{N} A(\sigma(i)). \tag{6.14}$$

In practice only a finite number N of successive states of the Markov chain is generated and $\langle A(\sigma) \rangle$ is estimated by

$$\langle A(\sigma) \rangle \approx \frac{1}{N} \sum_{i=1}^{N} A(\sigma(i)). \tag{6.15}$$

A full presentation of all the aspects of estimators of averages and errors and the speed of convergence of a Markov chain MC simulation would go beyond the scope of this chapter an we refer the interested reader to Ref. [74]. Metropolis *et. al.* not only reasoned that an algorithm that is ergodic and satisfies detailed balance converges to the true probability distribution, but also presented an implementation of such an algorithm. The *Metropolis algorithm* generates the configuration $\sigma(i+1)$ from the configuration $\sigma = \sigma(i)$ by a two step process:

1. Select a new candidate configuration with probability $S(\sigma \to \sigma')$ by (locally) changing the configuration σ.

2. Set $\sigma^{(i+1)} = \sigma'$ with probability

$$P_{\text{accept}}(\sigma \to \sigma') = \min\left[\frac{p(\sigma')\, S(\sigma' \to \sigma)}{p(\sigma)\, S(\sigma \to \sigma')}, 1\right] \tag{6.16}$$

and $\sigma^{(i+1)} = \sigma$ otherwise.

The transition matrix of the Metropolis algorithm is given by

$$T(\sigma \to \sigma') = S(\sigma \to \sigma')\, P_{\text{accept}}(\sigma \to \sigma') \tag{6.17}$$

and satisfies detailed balance. The selection probability S determines if the algorithm is ergodic and is often chosen so that $S(\sigma \to \sigma') = S(\sigma' \to \sigma)$, simplifying the acceptance probability (6.16) to

$$P_{\text{accept}}(\sigma \to \sigma') = \min\left[\frac{p(\sigma')}{p(\sigma)}, 1\right] = \min\left[\frac{W(\sigma')}{W(\sigma)}, 1\right]. \tag{6.18}$$

For the models discussed in this chapter this leads to the *single spin–flip Metropolis algorithm*:

1. Choose a site i at random and propose to flip the spin at the site to a random new direction σ_i'. This is ergodic as any configuration can be reached in a finite number of steps and in addition satisfies $S(\sigma \to \sigma') = S(\sigma' \to \sigma)$.

2. Accept the spin flip with probability

$$P_{\text{accept}} = \min\left[\exp\left(\beta\left(H[\sigma] - H[\sigma']\right)\right), 1\right]. \tag{6.19}$$

While this is in theory a fully sufficient algorithm to simulate any classical spin system, there are some practical obstacles in the application to systems with first and second order phase transitions (we will not discuss frustrated systems such as spin glasses and the problems associated with the simulation of these models). As we have mentioned, the configurations $\sigma(i)$ generated by any Markov chain MC algorithm are not independent. They are correlated in the the simulation or Monte Carlo time i, a fact quantified by the autocorrelation time τ. The

autocorrelation time is the timescale on which an independent sample is generated by the algorithm and is normally measured in Monte Carlo sweeps of the lattice It is related to the second–largest eigenvalue of the transition matrix, and for a system with a second order phase transition scales with the system size L as

$$\tau \sim L^z, \tag{6.20}$$

if the correlation length ξ of the system is larger than L [62]. z is called the dynamical critical exponent of the algorithm and is a measure for its effectiveness. For the two–dimensional Ising model the single spin–flip Metropolis algorithm has a dynamical critical exponent of $z \approx 2$, so that the computational effort to obtain a fixed number of independent samples for this model grows as $O(L^4)$ with the linear system size L, making the study of large system sizes close to the critical point difficult.

6.2.2 Cluster updates

The critical slowing down of the single–spin flip algorithm at a second order phase transition was overcome for the Ising and the Potts model by the development of the Swendsen–Wang cluster algorithm [62] and later extended by Wolff [75] to $O(n)$ models. Using an additional graph variable, these cluster algorithms perform collective changes in the configuration on length scales of the correlation length. In addition they are rejection free, that is a change of the configuration is always accepted. The equivalent development for unfrustrated quantum spin systems was the loop algorithm by Evertz [63]. To see which requirements a system has to satisfy so that a cluster algorithm can be used, we briefly review the construction of the Swendsen–Wang algorithm.

We start from the partition function in the spin representation

$$Z = \sum_{\sigma} W_\sigma(\sigma). \tag{6.21}$$

As the Hamiltonian (6.1) is a sum of bond terms and as $W_\sigma(\sigma) \propto \exp(-\beta H[\sigma])$, the weight of a configuration can be written as a product of bond weights

$$W_{ij}(\sigma_i, \sigma_j) = \exp\left(\beta h_{ij}[\sigma_i, \sigma_j]\right), \tag{6.22}$$

and the partition function (6.22) becomes

$$Z = \sum_{\sigma} \prod_{\langle ij \rangle} W_{ij}(\sigma_i, \sigma_j). \tag{6.23}$$

We now extend the configuration space of the system by introducing an additional graph variable ω on the bonds $\langle ij \rangle$ of the lattice. The graph ω is specified by its adjacency matrix $\omega_{ij} \in \{0, 1\}$. Our aim is to express the partition function as

$$Z = \sum_{\sigma} \sum_{\omega} \prod_{\langle ij \rangle} \Delta_{ij}(\sigma_i, \sigma_j, \omega_{ij})\, V_{ij}(\omega_{ij}), \tag{6.24}$$

where the first sum is over all configurations and the second sum is over all possible graphs. $\Delta_{ij}(\sigma_i, \sigma_j, \omega_{ij}) \in \{0, 1\}$ is an indicator function that tells us if a configuration σ_i, σ_j satisfies the constraints of the bond ω_{ij} or not, and the weight $V_{ij}(\omega_{ij})$ is independent of the configuration σ_i, σ_j. This transfers the weight of a configuration from the spin degrees of freedom to the graph degrees of freedom. We call a spin configuration σ compatible with a graph ω if all bond constraints are satisfies or

$$\Delta(\sigma, \omega) = \prod_{\langle ij \rangle} \Delta_{ij}(\sigma_i, \sigma_j, \omega_{ij}) = 1. \tag{6.25}$$

In the extended phase space the weight of a configuration–graph pair (σ, ω) is given by

$$W_{\sigma\omega}(\sigma, \omega) = \prod_{\langle ij \rangle} \Delta_{ij}(\sigma_i, \sigma_j, \omega_{ij})\, V_{ij}(\omega_{ij}). \tag{6.26}$$

To ensure that the transformed partition function represents the same physical system, the functions $\Delta_{ij}(\sigma_i, \sigma_j, \omega_{ij})$ and $V_{ij}(\omega_{ij})$ have to satisfy

$$W_{ij}(\sigma_i, \sigma_j) = \sum_{\omega_{ij}=0,1} \Delta_{ij}(\sigma_i, \sigma_j, \omega_{ij})\, V_{ij}(\omega_{ij}). \tag{6.27}$$

Before discussing how the functions Δ_{ij} and V_{ij} can be chosen for Ising, Potts, and $O(n)$ models, we demonstrate how a rejection free cluster update of the configuration σ can be constructed, if the weights of the system can be written in the form of Eq. (6.27). We assume for the moment that the functions Δ_{ij} and V_{ij} are independent of the bond $\langle ij \rangle$ and write $\Delta(\sigma_i, \sigma_j, \omega_{ij})$ and $V(\omega_{ij})$, although the cluster update can easily be generalized to bond dependent indicator and weight functions. Starting from a configuration σ, a cluster update is performed by the following steps, which are illustrated in Fig. 6.2:

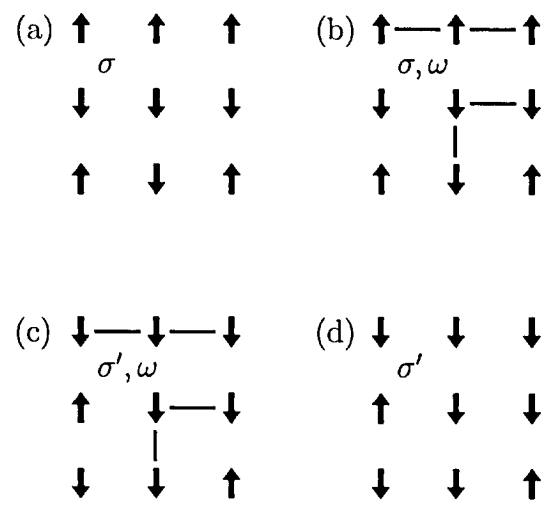

Figure 6.2: Illustration of the Swendsen–Wang cluster update for the ferromagnetic Ising model in the panels (a)→(d). Starting from a configuration σ, we select a graph ω. Then a new configuration σ' compatible with ω is found, and the graph ω is dropped.

1. Select a graph ω with probability $W_{\sigma\omega}(\sigma,\omega)/W_\sigma(\sigma)$.
2. Select a new configuration σ' from all configurations that are compatible with the graph ω at random.
3. Drop the graph ω.

The selection of the graph ω is considerably simplified by the fact that $W_{\sigma\omega}(\sigma,\omega)$ as defined in Eq. (6.26) is given by a product of weights. Therefore the bonds of the graph ω can be selected independently of each other. Consider a bond $\langle ij\rangle$ in the lattice. If the configurations of the spins σ_i and σ_j are so that only one of $\omega_{ij}=0,1$ satisfies Δ_{ij}, then ω_{ij} has to be assigned that value. The only nontrivial case is if both $\omega_{ij}=0$ and $\omega_{ij}=1$ satisfy Δ_{ij}. Then the probability of connecting the spins by a bond is given by

$$P_{\text{connect}} = P(\omega_{ij}=1) = \frac{V(1)}{V(0)+V(1)}, \tag{6.28}$$

while the probability of not connecting the spins by a bond is given by

$$1 - P_{\text{connect}} = P(\omega_{ij}=0) = \frac{V(0)}{V(0)+V(1)}. \tag{6.29}$$

The algorithm described above satisfies detailed balance and its ergodicity depends on the choice of Δ and V. Also it is in principle not necessary to completely drop the graph in the last step. We could keep the graph and update a fixed number of randomly chosen bonds in ω.

We now show how the functions V and Δ can be chosen for Ising, Potts, and $O(n)$ models. For the ferromagnetic Ising model with $\sigma_i = \pm 1$ and $h_{ij}[\sigma_i, \sigma_j] = \sigma_i \sigma_j$, the choices

$$\begin{aligned} V(0) &= \exp(-\beta) && (6.30)\\ V(1) &= \exp(\beta) - \exp(-\beta) && (6.31)\\ \Delta(\sigma_i, \sigma_j, 0) &= 1 && (6.32)\\ \Delta(\sigma_i, \sigma_j, 1) &= \delta_{\sigma_i, \sigma_j} && (6.33) \end{aligned}$$

lead to an ergodic algorithm. Antiparallel spins are always disconnected, while parallel spins are connected with probability

$$P_{\text{connect}} = 1 - \exp(-2\beta). \tag{6.34}$$

Any configuration for which the spins connected by a bond are parallel is compatible with a graph ω, so that each connected component of ω can be assigned one randomly chosen value for its spins once the graph ω is chosen. Choosing a random value for all connected components leads to the Swendsen–Wang algorithm, which has a dynamic critical exponent $z \approx 0.35$ [62] and is therefore considerably more effective than the single spin flip Metropolis algorithm. If only one of the connected components of ω is generated and flipped to a new value, we have the Wolff algorithm [75] for the Ising model. The probability to connect two spins (6.28) can also be directly expressed in terms of the bond weights as

$$P_{\text{connect}} = 1 - \min\left[\frac{W_{ij}(\sigma_i', \sigma_j)}{W_{ij}(\sigma_i, \sigma_j)}, 1\right], \tag{6.35}$$

where $W_{ij}(\sigma_i, \sigma_j) = W_{ij}(\sigma_i', \sigma_j')$ is the weight of the bond if either none or both spins σ_i and σ_j are flipped to new values σ_i' and σ_j', and $W_{ij}(\sigma_i', \sigma_j) = W_{ij}(\sigma_i, \sigma_j')$ is the weight if only one of the spins is flipped. The symmetry of the weights with respect to flipping both spins or either one of the spins reflects the fact that the graph can only "encode" two different weights. For the q–state Potts model with $h_{ij}[\sigma_i, \sigma_j] = \delta_{\sigma_i, \sigma_j}$ we can use the indicator function of the Ising model together

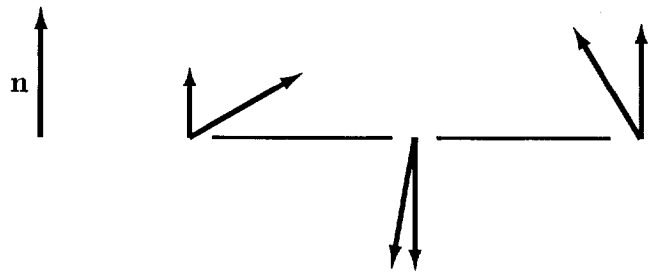

Figure 6.3: Construction of an effective Ising model shown as grey arrows from the XY model shown as black arrows by using a normal vector $\mathbf{n}$.

with $V(0) = 1$ and $V(1) = \exp(-\beta)$ leading to $P_{\text{connect}} = 1 - \exp(-\beta)$ for sites that have the same configuration and $P_{\text{connect}} = 0$ for all others.

To see how a particular choice of the functions Δ and V for the Ising model can result in a nonergodic algorithm, consider

$$V(0) = \exp(-\beta) \tag{6.36}$$

$$V(1) = \exp(\beta) \tag{6.37}$$

$$\Delta(\sigma_i, \sigma_j, 0) = 1 - \delta_{\sigma_i,\sigma_j} \tag{6.38}$$

$$\Delta(\sigma_i, \sigma_j, 1) = \delta_{\sigma_i,\sigma_j}. \tag{6.39}$$

While the resulting cluster update satisfies detailed balance, the configuration σ uniquely specifies the graph ω, and the graph ω specifies the configuration σ up to inversion symmetry so that the resulting algorithm is nonergodic.

To construct the functions Δ and V for the $O(n)$ model with $h_{ij}[\sigma_i, \sigma_j] = \sigma_i \cdot \sigma_j$, we have to generalize the notion of parallel and antiparallel spins to $O(n)$ spins. This has to be done in such a way that the weights satisfy $W_{ij}(\sigma_i, \sigma_j) = W_{ij}(\sigma_i', \sigma_j')$ and $W_{ij}(\sigma_i', \sigma_j) = W_{ij}(\sigma_i, \sigma_j')$ under the update or flip operation as mentioned in the construction of the cluster algorithm for the Ising model. Using a global reference vector $\mathbf{n} \in S_{n-1}$ as shown in Fig. 6.3, we define two spins to be parallel if their scalar product with $\mathbf{n}$ has the same sign, and we define a flip operation by mirroring a spin with respect to the plane defined by the normal vector $\mathbf{n}$. Writing $\sigma_{i,\mathbf{n}}$ for the projection of a spin σ_i onto $\mathbf{n}$ and $\sigma_{i,\mathbf{n}}^{\perp}$ for the orthogonal

complement, we call two spins σ_i and σ_j parallel if $\sigma_{i,\mathbf{n}}\,\sigma_{j,\mathbf{n}} > 0$ and define

$$\Delta_{\mathbf{n}}(\sigma_i, \sigma_j, 0) = 1 \tag{6.40}$$

$$\Delta_{\mathbf{n}}(\sigma_i, \sigma_j, 1) = \Theta(\sigma_{i,\mathbf{n}}\,\sigma_{j,\mathbf{n}}). \tag{6.41}$$

A flip of a spin corresponds to the change of sign of $\sigma_{i,\mathbf{n}}$ and the corresponding weight function is in analogy to the Ising model given by

$$V_{\mathbf{n},ij}(0) = \exp(-J_{\mathbf{n},ij}\,\beta) \tag{6.42}$$

$$V_{\mathbf{n},ij}(1) = \exp(J_{\mathbf{n},ij}\,\beta) - \exp(-J_{\mathbf{n},ij}\,\beta), \tag{6.43}$$

where $J_{\mathbf{n},ij} = |\sigma_{i,\mathbf{n}}\,\sigma_{j,\mathbf{n}}|$ is the effective exchange constant between the spins for a flip with respect to the normal vector $\mathbf{n}$. The probability to connect two spins is given by Eq. (6.35) as before. To obtain an ergodic algorithm the reference vector $\mathbf{n}$ has to be chosen at random for each cluster update.

The most important aspects of the construction of the cluster algorithms can be summarized as follows: If the weight of a configuration of the system can be written in a product form of bond weights $W_{ij}(\sigma_i, \sigma_j)$, and we can find an ergodic update or flip operation $\sigma_i \rightarrow \sigma_i'$ under which the weights have the symmetry properties $W_{ij}(\sigma_i, \sigma_j) = W_{ij}(\sigma_i', \sigma_j')$ and $W_{ij}(\sigma_i', \sigma_j) = W_{ij}(\sigma_i, \sigma_j')$, then we can construct a cluster algorithm by collectively updating clusters of spins, and the probability that two spins are be connected by a bond in the graph specifying the clusters for the update is given by Eq. (6.35).

6.2.3 Multicanonical ensemble simulations

While cluster algorithms solve the problem of critical slowing down for second order phase transitions, the simulation of a system with a first order phase transitions in a canonical ensemble simulation faces a different obstacle. The entropy of a finite system with a first order phase transition is shown schematically in the left panel of Fig. 6.4. Over an energy range given by the latent heat, the system favors a mixture of states with energy E_1 and E_2 over a pure state of energy $E_1 < E < E_2$ to maximize the entropy. The slope of the effective entropy given by a Maxwell construction is constant over this energy range and its value is called the pseudocritical temperature β_c for a finite system. In the canonical ensemble at β_c this results in a bimodal energy distribution with peaks at E_1 and

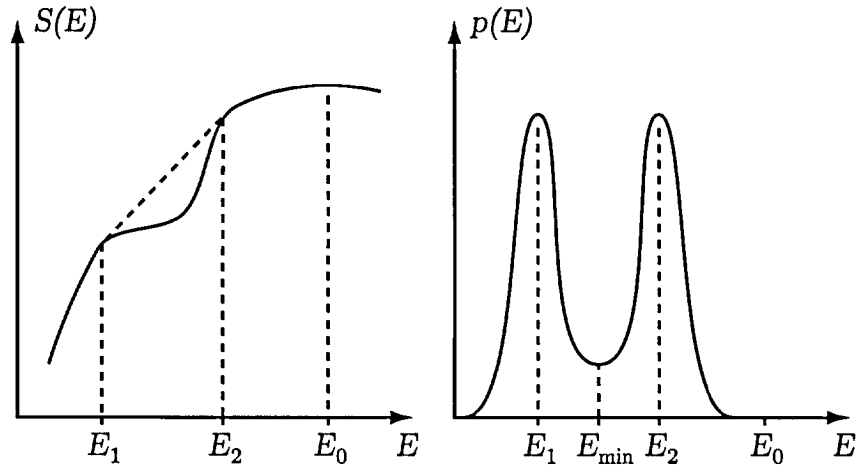

Figure 6.4: *Left:* Density of states of a system with a first order phase transition. The dashed line is a Maxwell construction maximizing the entropy and its slope is the pseudocritical temperature β_c. The latent heat of the first order transition is given by $\Delta Q = E_2 - E_1$. *Right:* Canonical energy distribution at the pseudocritical temperature β_c. The distribution is bimodal an has a minimum between E_1 and E_2 at $E_{\min}$.

E_2 of equal height. Between E_1 and E_2 the probability distribution $p(E)$ has a minimum, whose magnitude $p(E_{\min})$ scales as

$$p(E_{\min}) \sim \exp(-L^{d-1}) \tag{6.44}$$

with the linear size L of the system [64]. To go from a configuration with energy E_1 to a configuration with energy E_2 this free energy barrier has to be crossed by a canonical Monte Carlo simulation. The time an algorithm takes to go from a state with energy $E \approx E_1$ to a state with energy $E \approx E_2$ and vice versa is called the tunneling time τ of the algorithm. Due to Eq. (6.44) the tunneling time of a canonical ensemble simulation of such a model is expected to scale as

$$\tau \sim \exp(L^{d-1}), \tag{6.45}$$

irrespective of the use of either single–spin or cluster updates. This exponential growth of the tunneling time in a canonical simulation at the critical point is sometimes referred to as supercritical slowing down. As the system size grows, the tunneling time will become the dominant timescale in the system and therefore also become the autocorrelation time.

The tunneling problem in a canonical ensemble simulation was solved by the multicanonical ensemble introduced by Berg and Neuhaus [64, 65]. Similar methods based on the same principles are known under names such as broad histogram sampling, umbrella sampling or entropic sampling [65]. The idea of a multicanonical ensemble simulation is to reweight the configurations in such a way that configurations with an energy $E_1 < E < E_2$ are as likely to be visited as configurations with energy E_1 and E_2. In the multicanonical ensemble, this is done by sampling the configuration space with a single spin flip Metropolis algorithm with weights

$$W_{\mathrm{MC}}(\sigma) = \frac{1}{g_\sigma(H[\sigma])}, \tag{6.46}$$

where we have added the subscript "MC" to distinguish the weight used in the simulation from the canonical weight of the configuration. Note that the weights used in the simulation are independent of the temperature, so that configurations have to be reweighted to obtain finite temperature results. If the configurations are sampled by a Monte Carlo algorithm using the weights given by Eq. (6.46), each energy E has the same probability of being visited. Counting the number of times an energy E has been visited in a histogram $H(E)$, the histogram will become flat as the simulation progresses. In practice the density of states $g_\sigma(E)$ is of course not known exactly and has to be approximated by a function $\hat{g}_\sigma(E)$ which is improved during the simulation. Different methods to estimate $\hat{g}_\sigma(E)$ have been developed [65]. With the Wang–Landau algorithm [66, 67] a scalable and straightforward implementation of such an algorithm has become available, and we briefly review how the algorithm works.

We start with $\hat{g}_\sigma(E) = 1$ for all energies E and perform single spin flip Metropolis updates with weights given by

$$W_{\mathrm{MC}}(\sigma) = \frac{1}{\hat{g}_\sigma(H[\sigma])}. \tag{6.47}$$

Each time an energy level E is visited, $\hat{g}_\sigma(E)$ is multiplied by a factor $f > 1$ and a histogram of all visited energies is kept. If the histogram is sufficiently flat by some criterion, then f is reduced (e. g. $f \to \sqrt{f}$) and the histogram is reset. This is repeated until f is sufficiently small. An example for the flatness criterion is to require that the maximum and the minimum of the energy histogram collected during the simulation differ by no more than 30%. Because of the flatness criterion the Wang–Landau algorithm is also sometimes called a flat histogram

algorithm. In a practical implementation, the logarithm of $\hat{g}_\sigma(E)$ is stored and updated by $\ln(\hat{g}_\sigma(E)) \to \ln(\hat{g}_\sigma(E)) + \ln(f)$. By multiplying $\hat{g}_\sigma(E)$ with a factor the algorithm can model the exponential differences in the density of states at different energies. It is important to note that this algorithm does *not satisfy detailed balance*, unless $f = 1$. Although one can argue that the algorithm satisfies detailed balance approximately if f is sufficiently small, it should be viewed as an empirical algorithm to calculate $\hat{g}_\sigma(E)$. In fact if f is sufficiently small, the effect of multiplying $\hat{g}_\sigma(E)$ with f is smaller than the effect of the actual encounter with a state of energy E in the histogram [76] and a multicanonical ensemble simulation with $\hat{g}_\sigma(E)$ fixed (and which satisfies detailed balance) can be performed to obtain measurements.

To discuss the performance of the Wang–Landau algorithm and multicanonical ensemble simulations in general, we assume that a well converged estimate $\hat{g}_\sigma(E)$ has been obtained and set $\hat{g}_\sigma(E) = g_\sigma(E)$ in the following discussion. The tunneling time τ in a multicanonical ensemble simulation is often measured from the energy minimum of the system to either the energy maximum of the system or to the average energy at $\beta = 0$. Under the assumption that any critical or supercritical slowing down of the simulation is due to phase transitions and free energy barriers, this should lead to the same scaling of the tunneling time with the system size as for the original definition. It has been shown that the multicanonical ensemble simulation of a system with a first order phase transition removes the supercritical slowing down [64]. We can estimate the scaling of the tunneling time with the system size by a simple random walk argument. If the multicanonical ensemble simulation performs an unbiased random walk in energy space, we expect that the tunneling time for an Ising model in d dimensions scales as

$$\tau \sim L^{2d} \tag{6.48}$$

with the system size as the number of energy levels in the system is proportional to L^{2d}. Here the tunneling time is measured in single spin updates. In practice the tunneling time for the multicanonical ensemble simulation with single spin flips for the ferromagnetic Ising model is found [64, 77] to scale as

$$\tau \sim L^{2d+z}, \tag{6.49}$$

where the critical exponent z is analogous to the dynamical critical exponent of canonical simulations and has the value $z \approx 0.74$ [77] in 2 dimensions. Although

the multicanonical ensemble removes the supercritical slowing down at the first order phase transition of for example a 10-state Potts model, the scaling of the algorithm is not optimal and a critical slowing down remains for systems with first and second order phase transitions. This raises the question if a combination of cluster updates and multicanonical ensemble simulations can reduce the exponent z to a smaller value or to zero.

To answer this question we first have to discuss how multicanonical ensemble simulations can be combined with cluster updates. In the spin representation this is difficult as one requirement for the existence of a cluster algorithm was the fact that the weight of a configuration can be written as a product of bond weights. This is clearly not the case in the multicanonical ensemble for the spin representation. Reynal and Diep [69] have proposed to use the microcanonical temperature $\beta(E) = dS(E)/dE$ to build up clusters in a multicanonical simulation in the spin representation, but the resulting algorithm is not rejection free.

6.2.4 Multicanonical ensembles for different representations

An alternative approach first taken by Janke and Kappler [71] is to simulate a different representation of the Ising or Potts model by a multicanonical ensemble simulation. The canonical partition function of the Ising or Potts model in the spin representation was given by

$$Z = \sum_{\sigma} W_{\sigma}(\sigma), \tag{6.50}$$

where the weight of a configuration is

$$W_{\sigma}(\sigma) = \exp\left(-\beta H[\sigma]\right). \tag{6.51}$$

Using an additional graph variable we wrote the partition function of the Ising and the Potts model in the derivation of the canonical cluster algorithms as

$$Z = \sum_{\sigma} \sum_{\omega} W_{\sigma\omega}(\sigma, \omega). \tag{6.52}$$

We call this the spin–bond representation, and using Δ and V as defined in section 6.2.2 for the Ising and Potts model, $W_{\sigma\omega}(\sigma,\omega)$ as defined in Eq. (6.26) simplifies to

$$W_{\sigma\omega}(\sigma,\omega) = \Delta(\sigma,\omega)\, p^{n(\omega)}\, (1-p)^{n_b - n(\omega)}. \tag{6.53}$$

Here n_b is the total number of bonds in the lattice, $n(\omega)$ the number of bonds in the graph ω and the bond density parameter p is given by P_{connect}. Integrating over all possible configurations while keeping the graph fixed leads to a representation of the Ising or q–state Potts model in terms of graphs only. The partition function in this bond or graph representation is

$$Z = \sum_{\omega} W_{\omega}(\omega), \tag{6.54}$$

and the weight of a graph ω is given by

$$W_{\omega}(\omega) = q^{c(\omega)}\, p^{n(\omega)}\, (1-p)^{n_b - n(\omega)}, \tag{6.55}$$

where $c(\omega)$ the number of connected components of the graph ω (counting isolated sites). For each of the three representations a density of states can be defined in natural variables as we have done for the spin representation in Eq. (6.7). For the spin representation in terms of the energy E

$$g_{\sigma}(E) = \sum_{\sigma} \delta(H[\sigma] - E), \tag{6.56}$$

for the spin–bond representation in terms of the number of occupied bonds n

$$g_{\sigma\omega}(n) = \sum_{\sigma} \sum_{\omega} \delta(n(\omega) - n)\, \Delta(\sigma,\omega), \tag{6.57}$$

and for the bond representation in terms of the number of occupied bonds n and the number of connected components or clusters c

$$g_{\omega}(n,c) = \sum_{\omega} \delta(n(\omega) - n)\, \delta(c(\omega) - c). \tag{6.58}$$

Using these densities of states the corresponding forms of the partition function are

$$Z = \sum_{E} g_{\sigma}(E)\, e^{-\beta E}, \tag{6.59}$$

$$Z = \sum_{n} g_{\sigma\omega}(n)\, p^{n}\, (1-p)^{n_b - n}, \tag{6.60}$$

$$\text{and } Z = \sum_{n,c} g_{\omega}(n,c)\, q^{c}\, p^{n}\, (1-p)^{n_b - n}. \tag{6.61}$$

The Wang–Landau algorithm or any other multicanonical ensemble simulation can be applied to all three representations. The bond representation generally requires a two–dimensional histogram. Only in one dimension, the number of clusters and the number of bonds are related so that a histogram in one variable is sufficient. It was shown that the tunneling time of the one dimensional Ising model in the multicanonical ensemble simulation of the bond representation with

$$W_{\mathrm{MC}}(\omega) = \frac{1}{g_\omega(n(\omega), c(\omega))} \tag{6.62}$$

using single–bond Metropolis updates scales as $L^2 \log(L)$ and thus $z = 0$, while a multicanonical ensemble simulation of the spin representation of the same system shows a critical slowing down with an exponent $z \approx 1.81$ [78]. Integrating out the spin degrees of freedom has changed the scaling behavior of the multicanonical ensemble simulation although only single bond Metropolis updates are performed on the graph variable ω in the graph representation.

In higher dimensions it is easier to use the spin–bond representation. Janke and Kappler used the spin–bond representation of the Potts model to perform a multicanonical ensemble simulation in the number of bonds in the graph with weights

$$W_{\mathrm{MC}}(\sigma, \omega) = \frac{\Delta(\sigma, \omega)}{g_{\sigma\omega}(n(\omega))}. \tag{6.63}$$

This multibondic ensemble of Janke and Kappler uses local Metropolis updates on the graph variable ω, while the configuration σ is updated with a cluster algorithm. At fixed ω all configurations compatible with ω have the same finite weight, while all configurations not compatible with ω have zero weight as can be seen from Eq. (6.63). Thus any connected component of ω can be assigned a randomly chosen spin value as it was the case for the canonical cluster algorithm. Yamaguchi and Kawashima [68] extended the method by showing that a global and rejection free update of the graph variable is also possible and Fig. 6.5 shows the scaling of the tunneling time from a disordered state to the ground state in the number spin updates for the multicanonical ensemble simulation of the two dimensional Ising model using the method of Yamaguchi and Kawashima. The tunneling time shows a $L^4 \log(L)$ behavior and thus again $z = 0$. This scaling behavior remains if local updates are used for the graph variable [78]. Thus to remove the critical slowing down of a multicanonical ensemble simulation it seems to be sufficient to find an algorithm that performs cluster updates on the spin

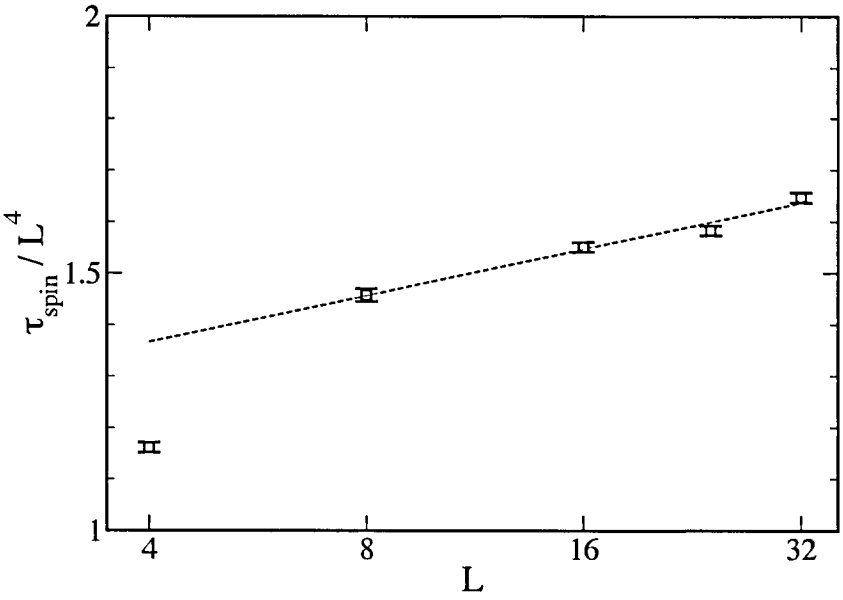

Figure 6.5: Plot of the tunneling time for the simulation of the two dimensional Ising model using the multibondic algorithm (□) with global graph updates of Yamaguchi and Kawashima [68]. Line is drawn as a guide to the eye.

degrees of freedom, while a global update of the graph variable does not seem to be a necessary ingredient to obtain an algorithm with optimal scaling.

6.3 Spin–multigraph representation

The methods of the previous section are not easily generalized to to continuous spin models, as no equivalent representation to the spin–bond or bond representation exists for these models. While we can write the partition function in a spin–bond representation similar to the one for the Ising model, this can only be done for a fixed normal vector $\mathbf{n}$, while we used the fact that $\mathbf{n}$ can be chosen at random for each update in a canonical cluster updates of an $O(n)$ models to obtain an ergodic algorithm. To combine cluster updates with the multicanonical ensemble simulation of a continuous spin model we now examine another representation of the partition function. Like the spin–bond representation it has a configuration and a graph variable, but in contrast to the spin–bond representation, the graph variable is a multigraph and does not automatically specify the

spins that form a connected component in a step of the cluster update. As this representation is related to the high temperature series of the partition function, we briefly review how a simple high temperature series representation can be sampled in a multicanonical ensemble simulation. We write the partition function as a series

$$Z = \sum_n g_\beta(n)\beta^n \tag{6.64}$$

in the inverse temperature. The corresponding density of states is given by

$$g_\beta(n) = \sum_\sigma \frac{(-H[\sigma])^n}{n!}, \tag{6.65}$$

and if $H[\sigma] \leq 0$, then the weight of a configuration–order pair

$$W_\beta(\sigma, n) = \frac{(-H[\sigma])^n}{n!}, \tag{6.66}$$

is always positive, and we can perform a multicanonical simulation in the extended (σ, n)–phase space using updates on the configuration σ the order n. Assuming that the σ and n updates are performed independently of each other and that single spin flip Metropolis updates are used, an update of the order $n \to n'$ (for example $n' = n \pm 1$) is accepted with probability

$$P_{n\to n'} = \min\Big[(-H[\sigma])^{n'-n}\frac{n!}{n'!}\frac{g_\beta(n)}{g_\beta(n')}, 1\Big]. \tag{6.67}$$

A single spin flip configuration update $\sigma \to \sigma'$ at fixed n is accepted with probability

$$P_{\sigma\to\sigma'} = \min\Big[\Big(\frac{H[\sigma']}{H[\sigma]}\Big)^n, 1\Big]. \tag{6.68}$$

In a practical computation n is truncated at some cutoff Λ, restricting the largest inverse temperature that can be reached to $\beta_{\max} \sim \Lambda/V$ [70], where V is the volume of the system.

Because the weight of a configuration as defined in Eq. (6.66) is not a product of bond weights on the lattice, the (σ, n)–representation cannot be directly used to implement cluster updates. To obtain such a representation we start from

$$\exp\left(-\beta H[\sigma]\right) = \prod_{\langle ij\rangle} \exp\left(\beta h_{ij}[\sigma_i, \sigma_j]\right) \tag{6.69}$$

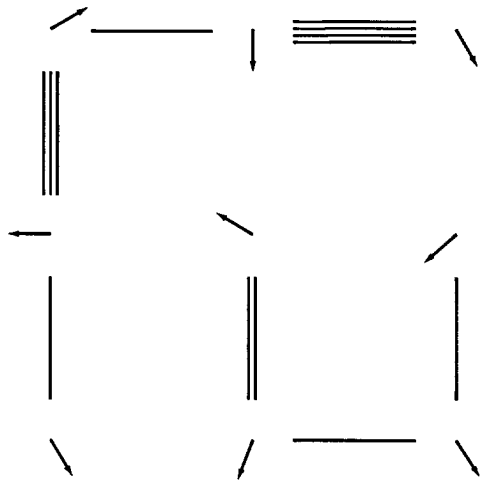

Figure 6.6: Example of a spin–multigraph configuration with $n = 13$ for an XY–model on a 3 by 3 square lattice.

and expand each exponential term in β with a separate integer variable γ_{ij}

$$\exp\left(\beta h_{ij}[\sigma_i, \sigma_j]\right) = \sum_{\gamma_{ij}=0}^{\infty} \frac{h_{ij}[\sigma_i, \sigma_j]^{\gamma_{ij}} \beta^{\gamma_{ij}}}{\gamma_{ij}!}. \tag{6.70}$$

We identify each set of γ_{ij} on the lattice with a multigraph γ that has γ_{ij} bonds between site i and site j as illustrated in Fig. 6.6. If we write $n(\gamma) = \sum_{\langle ij \rangle} \gamma_{ij}$ for the total number of bonds in the multigraph γ, $g_\beta(n)$ as defined in Eq. (6.65) is given by

$$g_\beta(n) = \sum_{\sigma} \sum_{\gamma} \delta(n(\gamma) - n) \prod_{\langle ij \rangle} \frac{h_{ij}[\sigma_i, \sigma_j]^{\gamma_{ij}}}{\gamma_{ij}!}. \tag{6.71}$$

The sum is over all spin configurations σ and all multigraphs γ on the lattice. Equation (6.71) should be compared to Eq. (6.57) of the spin–bond representation. The corresponding partition function is given by Eq. (6.64), and the weight of a configuration–multigraph pair is given by

$$W_\beta(\sigma, \gamma) = \prod_{\langle ij \rangle} W_{ij}(\sigma_i, \sigma_j, \gamma_{ij}), \tag{6.72}$$

where $W_{ij}(\sigma_i, \sigma_j, \gamma_{ij}) = h_{ij}[\sigma_i, \sigma_j]^{\gamma_{ij}}/\gamma_{ij}!$ is the weight of a bond $\langle ij \rangle$. The energies in the system have to be shifted so that $h_{ij}[\sigma_i, \sigma_j] \geq 0$ to ensure that all weights are positive. As for the simple high temperature series representation two types of updates, one in the multigraph γ and one the configuration σ are required.

As the weight of a configuration at fixed multigraph γ is now a product of bond weights, it is possible to use cluster updates to update the configuration when γ is fixed.

In a multicanonical ensemble simulation in the order n a local multigraph update $\gamma \to \gamma'$ such as $\gamma'_{ij} = \gamma_{ij} \pm 1$ for one randomly chosen bond $\langle ij \rangle$ will be accepted with Metropolis probability

$$P_{\gamma \to \gamma'} = \min \Big[\frac{g_\beta(n(\gamma))}{g_\beta(n(\gamma'))} \prod_{\langle ij \rangle} \frac{W_{ij}(\sigma_i, \sigma_j, \gamma'_{ij})}{W_{ij}(\sigma_i, \sigma_j, \gamma_{ij})}, 1 \Big]. \tag{6.73}$$

The configuration update can either be implemented as a cluster update or as a single spin flip Metropolis update. For the cluster update we choose the same flip operation as for the canonical cluster algorithms. The probability of connecting two spins is then given by Eq. (6.35), which for the spin–multigraph ensemble simplifies to

$$P_{\text{connect}} = 1 - \min \Big[\Big(\frac{h_{ij}[\sigma_i, \sigma'_j]}{h_{ij}[\sigma_i, \sigma_j]} \Big)^{\gamma_{ij}}, 1 \Big]. \tag{6.74}$$

Note that the multigraph γ does not directly correspond to the graph ω that determines the connected connected components of the cluster update. However using Eq. (6.74) we see that only sites that are connected by at least one bond of the multigraph can be added to the cluster and that parallel spins are more likely to be connected if γ_{ij} is large. In a local update scheme, a configuration update $\sigma \to \sigma'$ at fixed γ will be accepted with Metropolis probability

$$P_{\sigma \to \sigma'} = \min \Big[\prod_{\langle ij \rangle} \Big(\frac{h_{ij}[\sigma'_i, \sigma'_j]}{h_{ij}[\sigma_i, \sigma_j]} \Big)^{\gamma_{ij}}, 1 \Big]. \tag{6.75}$$

We now apply the spin–multigraph representation to two different models for which the exact density of states $g_\beta(n)$ can be calculated and compare the efficiency of cluster updates to the efficiency of single–spin updates in this representation.

6.3.1 2–dimensional Ising model

We start by applying the spin–multigraph representation to the two dimensional Ising model. For the Ising or q–state Potts model with $h_{ij}[\sigma_i, \sigma_j] = \delta_{\sigma_i, \sigma_j}$, the

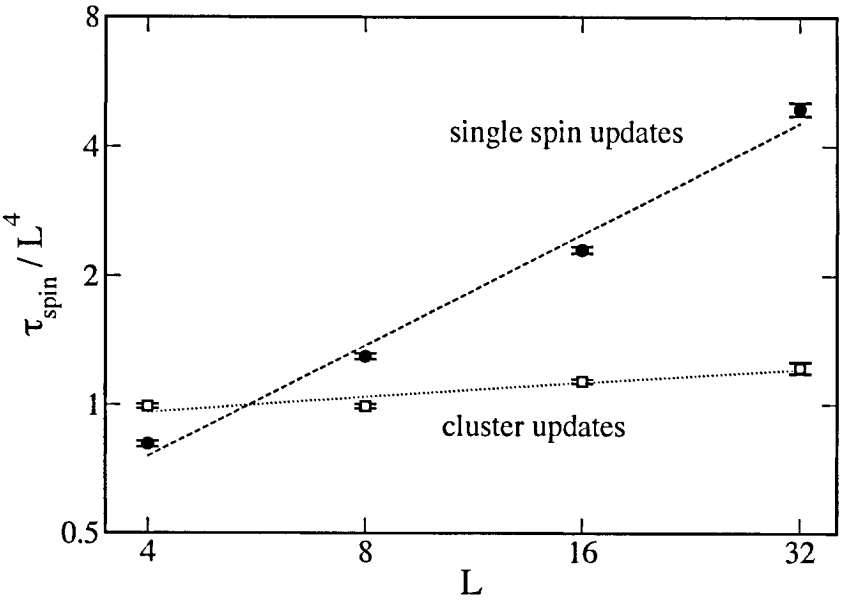

Figure 6.7: Scaling of the tunneling time for the $d = 2$ Ising model using the simple high temperature representation with single spin updates (•) and using the spin–multigraph representation with Swendsen–Wang cluster updates (□). The lines are drawn as a guide to the eye.

weight of a spin–multigraph configuration as defined by Eq. (6.72) simplifies to

$$W_\beta(\sigma, \gamma) = \Delta(\sigma, \gamma) \frac{\beta^{n(\gamma)}}{\prod_{\langle ij \rangle} \gamma_{ij}!}, \tag{6.76}$$

where $\Delta(\sigma, \gamma) = 1$ if all bonds in the multigraph γ are satisfied and 0 otherwise. Thus the weights of all configurations that are compatible with a multigraph are the same and the multigraph γ uniquely determines the graph ω of the cluster update. Given a multigraph γ any connected component of gamma can be assigned a random value for its spins, resulting in an algorithm that is very similar to the cluster updates for the Ising model in the spin–bond representation.

To compare the effectiveness of the cluster updates to single spin flip updates, we measure the tunneling time τ from a random state σ at $n = 0$, which is equivalent to $\gamma_{ij} = 0$ for all $\langle ij \rangle$, to the ground state of the system. At $n = 0$ all configurations σ are equally probable so that we are starting from an equilibrium configuration at $n = 0$. We perform a fixed ratio of spin to multigraph updates. To extract the asymptotic behavior of the tunneling time we measure the tun-

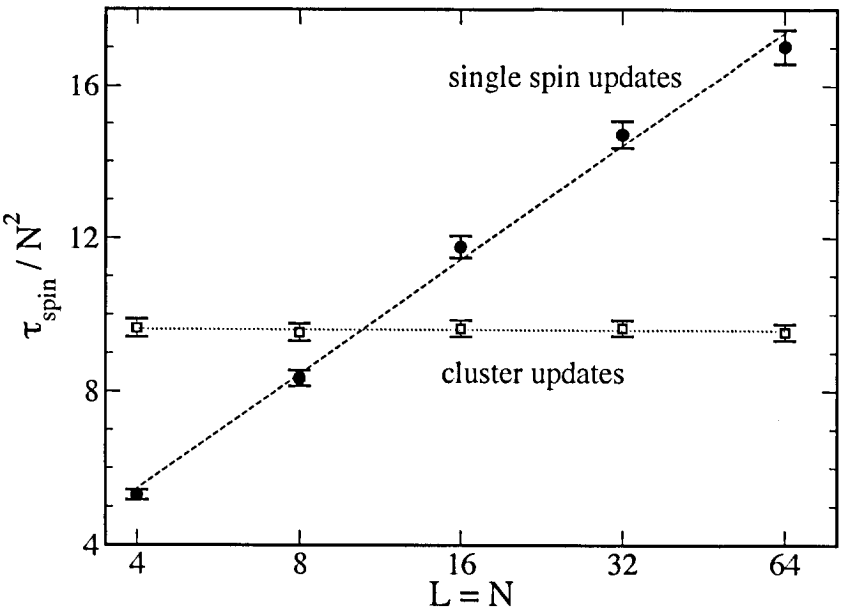

Figure 6.8: Scaling of the mean first-passage time to reach a low energy state for the $d = 1$ XY model using single spin updates (•) and Swendsen–Wang cluster updates (□) in the spin–multigraph. Lines are drawn as a guide to the eye.

neling time in the number of spin updates only for different ratios of multigraph to configuration updates. With an increasing fraction of multigraph updates the tunneling time converges to a limiting value τ_{spin}. The cutoff Λ is chosen in such a way that the average n for which the ground state is reached is much smaller than Λ. Figure 6.7 shows the scaling of τ_{spin} for the $d = 2$ Ising model for single spin flip Metropolis updates in the simple high temperature representation given by Eq. (6.66) and for the spin–multigraph representation using Swendsen–Wang cluster updates. The single spin flip updates show a power law behavior with a dynamical critical exponent of $z = 0.85 \pm 0.06$, while the cluster updates can be fitted by a logarithmic behavior or a power law with $z = 0.10 \pm 0.02$. Thus the cluster updates of the configurations in the spin–multigraph representation are able to remove the critical slowing down for the Ising model.

6.3.2 1–dimensional XY model

To examine if cluster updates and single–spin updates in the spin–multigraph representation have a different scaling behavior, we apply the spin–multigraph representation to the one dimensional XY model with open boundary conditions. The cluster update is performed with respect to a randomly chosen normal vector $\mathbf{n}$ and the probability to connect two spins by a Swendsen–Wang cluster bond is given by Eq. (6.74). The tunneling time is measured by the same method as for the Ising model. The only difference is that we measure the time the algorithm takes to reach a state which is within 2.5% of the total width of the spectrum to the ground state. Figure 6.8 shows the scaling of τ_{spin} for the $d = 1$ XY model using single spin updates and Swendsen–Wang cluster updates in the spin–multigraph representation. The single spin updates show a $L^2 \log(L)$ scaling of the tunneling time with the system size, while the cluster updates show a L^2 scaling.

6.4 Conclusion

In this chapter we have introduced a new representation that can be used to combine cluster updates with the multicanonical simulation of continuous spin systems. The spin–multigraph representation can be considered a generalization of the spin–bond representation and we obtain similar cluster updates for the spin degrees of freedom for the Ising model in both representations. The spin–multigraph representation can also be viewed as the classical limit of the stochastic series expansion method for quantum systems [79]. The order of the operators in the operator–string used in the stochastic series expansion is unimportant for a classical system, so that only the number of occurrences of an operator $h_{ij}[\sigma_i, \sigma_j]$ in the operator string has to be counted. This is done by the number of edges γ_{ij} connecting site i and j in the spin–multigraph representation. We have demonstrated that the method removes the critical slowing down associated with single spin updates for the two dimensional Ising model and that the method improves the scaling of the tunneling time for the one dimensional XY model. Due to the nature of the system examined, we were not able to demonstrate the removal of any critical slowing down for a continuous system. A promising complementary

approach to overcome the critical slowing down of the single spin flip algorithm is to use an optimized ensemble that tries to maximize the diffusivity of the random walker in energy space [80].

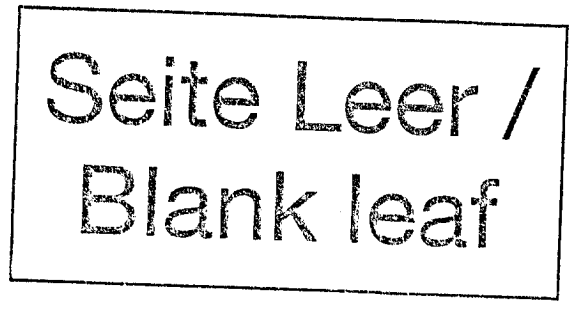
Seite Leer /
Blank leaf

Chapter 7

Energy fluctuations in spin glasses

7.1 Introduction

There has been a renewed interest in ground–state energy fluctuations for the mean–field Sherrington–Kirkpatrick (SK) spin–glass model [81, 82], as well as for short–range spin glasses [83]. Sample–to–sample fluctuations in disordered systems, quantified by their limiting distribution P_∞, play an important role in the understanding of their properties. Previous studies have focused either on the mean–field model [81, 82] for which the analytical form of the limiting distribution remains unclear, or on short–range spin glasses [83] in two and three dimensions for which a Gaussian limiting distribution is suggested by data obtained for small system sizes. Here we attempt to consolidate the limiting cases of short–range and long–range interactions by studying a disordered one–dimensional Ising spin chain with power–law interactions [84, 85, 86, 87, 88]. Its advantage over conventional models is that by tuning the power–law exponent several universality classes ranging from mean–field to short–range behavior can be probed. We complement this with results obtained for a two–leg spin ladder with short–range interactions for which an exact transfer–matrix algorithm can be applied, in order to compute relevant moments of the energy distributions for large system sizes and compare the results to short–range spin glasses.

Our results show clearly for a large range of system sizes that mean–field spin–glass models have a non–Gaussian limiting distribution with a finite skewness in the thermodynamic limit. In particular, the limiting distribution of the mean–field Sherrington–Kirkpatrick model, which is a special case of the one–dimensional Ising chain with power–law interactions, seems to be well described by a modified Gumbel distribution, a behavior that has not been explained so far. A similar behavior of a non–Gaussian limiting distribution has been observed for the ground–state energy distribution of the 1+1–dimensional directed polymer in a random medium [89, 90]. In contrast, the limiting distribution of non–mean–field spin–glass models is well described in the thermodynamic limit by a Gaussian distribution.

In general we expect the ground–state energy of a disordered system to be a random variable that can be characterized by the mean $\langle E \rangle$, the standard deviation σ_E, and the skewness ζ_E [91]. In this work we study the size–dependence of the aforementioned observables. In particular, we surmise that the mean ground–state energy of a (one–dimensional) random system scales as

$$\langle E_L \rangle / L = e_\infty + a L^{-\omega} \,, \tag{7.1}$$

where L represents the system size (and number of spins). We keep the extra factor of L in Eq. (7.1), as well as in the following definitions in order to be able to compare to the exponent estimates of Ref. [81]. The standard deviation of the ground–state energy of a general disordered system can be expected to scale as

$$\sigma_E / L = b L^{-\rho} \,. \tag{7.2}$$

Following previous results by Ref. [83] we expect the skewness to decay as

$$\zeta_E = c_1 + c_2 L^{\gamma} \tag{7.3}$$

with $\gamma < 0$. As we shall see later, $c_1 = 0$ for the short–range models. We also want to test if the scaled probability distribution functions $P_L(\epsilon_L)$ with $\epsilon_L = (E_L - \langle E_L \rangle)/\sigma_E$ converge to a limiting form $P_\infty(\epsilon_L)$ for $L \to \infty$. If this is the case, then data for the ground–state energies should scale via

$$P_L(E_L) = \frac{1}{\sigma_E} P_\infty \left(\frac{E_L - \langle E \rangle}{\sigma_E} \right) \,. \tag{7.4}$$

We do not attempt to make a prediction regarding the exact functional form of the limiting distribution for an arbitrary spin–glass model. Bouchaud *et al.* [83]

have shown for small L that typical short–range spin glass models have a Gaussian limiting distribution. For the case of the mean–field model a modified Gumbel distribution [92, 93, 81] with $m = 6$ has been found empirically to fit the data of the SK model best. As the ground–state energy distribution is not a minimum of independent random variables, is not surprising that its distribution does not belong to one of the standard three universality classes for the minimum of uncorrelated variables [94], but it remains an unsettled issue if the modified Gumbel distribution is the exact limiting–distribution, or only the best fitting function available.

For finite values of the power–law exponent we show that a product of the modified Gumbel distribution with a Gaussian distribution describes the observed data well. This ansatz reflects the view, that for non–mean–field models the skewness of the distribution of small systems is averaged out as the system size is increased. Using this ansatz, we find that the Gaussian distribution dominates the modified Gumbel distribution as the system size is increased in the non–mean–field universality class, thus showing that in the thermodynamic limit a Gaussian distribution is recovered.

7.2 Two–leg spin–glass ladder

In order to compare results for a one–dimensional Ising spin chain with long–range interactions to a simple benchmark model for which large system sizes can be studied, we first examine the Ising model on a two–leg ladder (see Fig. 7.1) with couplings J_{ij} between nearest–neighbor spins chosen from a Gaussian distribution with zero mean and unit standard deviation. A system of length L is described by the following Hamiltonian:

$$H = \sum_{l=1}^{L} J_{(l,a),(l,b)}\, S_{(l,a)}\, S_{(l,b)} + \sum_{l=1}^{L-1} \sum_{i=a,b} J_{(l,i),(l+1,i)}\, S_{(l,i)}\, S_{(l+1,i)}. \qquad (7.5)$$

The first summation in Eq. (7.5) runs over all rungs l, while the second summation runs over all exchanges between the rungs, and $S_{(l,i)} = \pm 1$ is the value of the (Ising) spin on the i–th leg of the l–th rung of the ladder. The ground–state energy of the system can be efficiently calculated with a transfer matrix algorithm [95, 96]. The transfer matrix algorithm computes the ground–state energy of a system

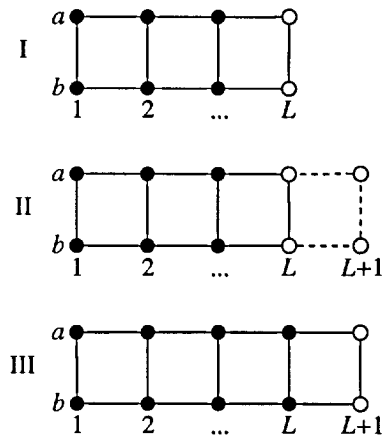

Figure 7.1: Illustration of a step in the transfer matrix calculation. Starting with a system of size L (panel I) whose ground–state energy is known as a function of the spins shown as open circles, we add another rung and calculate the change in energy $\Delta_{\rm E}$ given by the dashed line [see panel II and Eq. (7.7)]. The ground–state energy of the system as a function of the spins in the $L+1$–th rung is then calculated by taking the minimum of $E_{\rm g}+\Delta_{\rm E}$ over all configurations of the L–th rung [see panel III and Eq. (7.6)].

of size L with fixed couplings in $O(L)$ time so that large systems can be studied. A disorder average has to be taken explicitly by repeating the algorithm for a number of disorder realizations of the bonds.

7.2.1 Numerical method: transfer matrices

We can explain the transfer matrix algorithm by starting with a ladder of length L and assuming that the ground–state energy $E_{\rm g}(L,\{S_{(L,i)}\})$ of the ladder is known as a function of the spin configuration $\{S_{(L,i)}\}$ of the L–th rung. We add the spins of the $L+1$–th rung to the system as illustrated in Fig. 7.1 and use the relation

$$E_{\rm g}(L+1,\{S_{(L+1,i)}\}) = \min_{\{S_{(L,i)}\}} \left[E_{\rm g}(L,\{S_{(L,i)}\}) + \Delta_{\rm E}(\{S_{(L,i)}\},\{S_{(L+1,i)}\})\right] \quad (7.6)$$

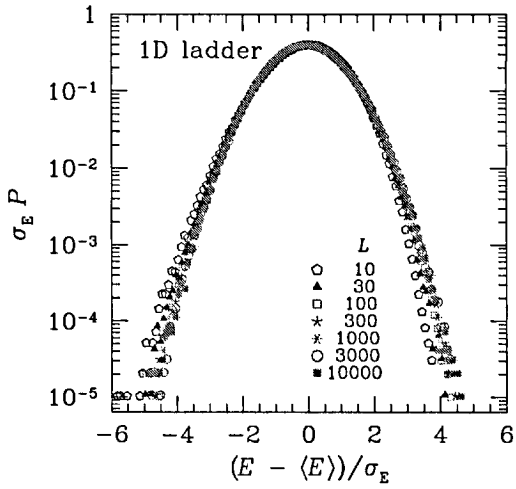

Figure 7.2: Scaling of the ground–state energy according to Eq. (7.4) for the ladder system. The data scale well, although deviations in the tails suggest that that the skewness of the function is changing with system size L.

to integrate out the spins of the L–th rung and to obtain E_g as a function of the spins of the $L+1$–th rung. Here

$$\Delta_E(\{S_{(L,i)}\},\{S_{(L+1,i)}\}) = \sum_{i=a,b} J_{(L,i),(L+1,i)} S_{(L,i)}\, S_{(L+1,i)} + J_{(L+1,a),(L+1,b)} S_{(L+1,a)}\, S_{(L+1,b)} \qquad (7.7)$$

is the exchange energy of the spins added on the $L+1$–th rung with themselves and with the spins of the L–th rung. Starting with two spins we iterate this procedure until the system has the desired size and repeat the calculation until a desired number of disorder realizations is obtained.

7.2.2 Results

In Fig. 7.2 we scale the data for the energy of the ladder system according to Eq. (7.4) for system sizes up to $L = 10^4$. For each system size we compute 10^6 samples. The data scale well, although deviations are present in the tails. In particular, for small L the distribution is clearly skewed. For the short–ranged

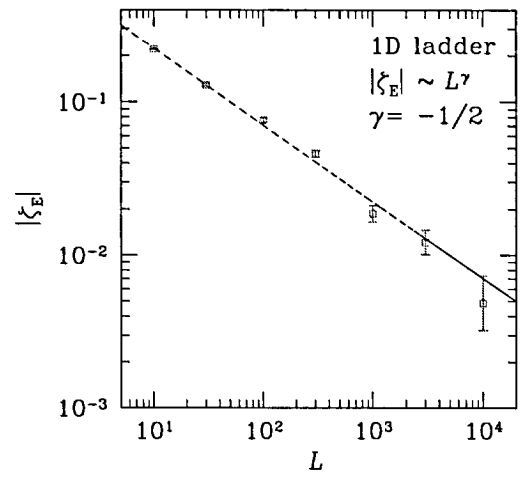

Figure 7.3: Skewness of the energy distributions as a function of system size L for the ladder system. The skewness can be well fitted to a power–law decay with an exponent $\sim -1/2$. This suggests that in the thermodynamic limit the limiting distribution is Gaussian (zero skewness).

ladder system we obtain a clear power–law decay of the skewness according to Eq. (7.3) with $\gamma \approx -0.5$ (and $c_1 = 0$), as can be seen in Fig. 7.3. This suggests that in the thermodynamic limit the ground–state energies have a Gaussian distribution. For completeness, we quote the results for the size–dependence of the mean and standard deviation. We obtain for the mean energy

$$\langle E_L \rangle = -2.12582(8) - 0.801(8) L^{-0.996(4)} \tag{7.8}$$

and for the fluctuations

$$\sigma_E = 0.976(5) L^{0.497(8)} \, . \tag{7.9}$$

Our results show that $\sigma_E \sim L^{1/2}$ and $\langle E_L \rangle / L - e_\infty \sim 1/L$, a results which agrees with data on the one–dimensional Ising chain in the short–range universality class.

The results on the one–dimensional ladder for very large system sizes already suggest that for short–ranged systems the skewness of the distributions vanish in the thermodynamic limit. This is in contrast to recent results [81] for the mean–field Sherrington–Kirkpatrick model [97], where the limiting distribution

P_∞ seems to have a finite skewness and thus cannot be properly described by a Gaussian distribution.

7.3 One–dimensional Ising chain

The Hamiltonian for the one–dimensional long–range Ising spin glass with power–law interactions is given by

$$H = -\sum_{i,j} J_{ij} S_i S_j \,, \tag{7.10}$$

where $S_i = \pm 1$ represent Ising spins evenly distributed on a ring of length L in order to ensure periodic boundary conditions. The sum is over all spins on the chain and the couplings J_{ij} are given by [87]

$$J_{ij} = c(\sigma)\frac{\epsilon_{ij}}{r_{ij}^{\sigma}} \,, \tag{7.11}$$

where the ϵ_{ij} are chosen according to a Gaussian distribution with zero mean and standard deviation unity

$$\mathcal{P}(\epsilon_{ij}) = \frac{1}{\sqrt{2\pi}} \exp(-\epsilon_{ij}^2/2) \tag{7.12}$$

and $r_{ij} = (L/\pi)\sin[(\pi|i-j|)/L]$ represents the *geometric* distance between the spins on the ring. The power–law exponent σ determines the range of the interactions and thus the universality class of the model, as described in the next section. The constant $c(\sigma)$ in Eq. (7.11) is chosen to give a mean–field transition temperature $T_c^{\mathrm{MF}} = 1$, where

$$\left(T_c^{\mathrm{MF}}\right)^2 = \sum_{j\neq i,\, i \text{ fixed}} [J_{ij}^2]_{\mathrm{av}} = c(\sigma)^2 \sum_{j\neq i,\, i \text{ fixed}} \frac{1}{r_{ij}^{2\sigma}} \,. \tag{7.13}$$

Here $[\cdots]_{\mathrm{av}}$ denotes an average over disorder.

In this work we compute unscaled energies for the one–dimensional Ising chain. Thus we find the optimal configuration of spins $\{S_i\}$ which minimizes the Hamiltonian in Eq. (7.10) for a given set of interactions $\{J_{ij}\}$, i.e.

$$E_L = \min_{\{S_i\}} H_{\{J_{ij}\},\{S_i\}} \,. \tag{7.14}$$

The (commonly used) energy per degree of freedom e_L is then given by $e_L = E_L/L$.

7.3.1 Phase diagram

The long–range Ising spin glass with power–law interactions has a very rich phase diagram in the d–σ plane. This is summarized in Fig. 7.4, which is based on work performed by Bray *et al.* [84] and by Fisher and Huse [85], who present a detailed analysis of the role of long–range interactions within the droplet model. Spin–glass behavior is controlled by the long–range part of the interaction if σ is sufficiently small, and by the short–range part if σ is sufficiently large. More precisely, one has long–range behavior if the stiffness exponent of the long–range (LR) universality class, $\theta_{\rm LR}$, is greater than that of the short–range (SR) universality class, $\theta_{\rm SR}$, and vice versa. In addition, there is an exact result for $\theta_{\rm LR}$, namely [84, 85]

$$\theta_{\rm LR} = d - \sigma, \tag{7.15}$$

so long–range behavior occurs if

$$\sigma < \sigma_c(d) = d - \theta_{\rm SR}(d)\ . \tag{7.16}$$

Equation (7.15) indicates that critical exponents depend continuously on σ in the long–range region, even though they are independent of σ in the region controlled by the short–range part of the interaction. Thus we expect to be able to tune the different universality classes by changing the exponent σ. The condition for a finite–temperature transition is $\theta > 0$, where θ refers here to the greater of $\theta_{\rm SR}$ and $\theta_{\rm LR}$. For the short–range model, there is a finite–temperature transition (i.e., $\theta_{\rm SR} > 0$) for d larger than the lower critical dimension d_l, which is found numerically to lie between 2 and 3 [98, 99, 100, 101, 102]. For $d = 1$, as in the present study, we obtain a finite transition temperature for $\sigma < 1$.

For $\sigma < d/2$ the model does not have a thermodynamic limit ($T_{\rm c}$ diverges) unless the interactions are scaled with an appropriate (inverse) power of L, i.e., $c(\sigma) \to 0$ for $L \to \infty$. Note that $\sigma = 0$ corresponds to the SK model.

7.3.2 Numerical methods

Ground–state energies for the one–dimensional Ising chain are computed using the parallel tempering Monte Carlo method [103, 104, 105, 87] when the power–law exponent σ is small, and the branch, cut & price (BCP) algorithm when σ is

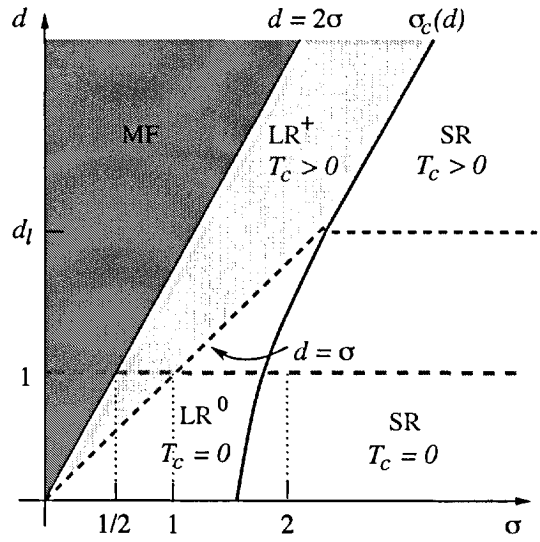

Figure 7.4: Sketch of the phase diagram in the d–σ plane for the spin–glass state of the disordered long–range Ising model with power–law interactions following Ref. [85]. The light shaded region (LR^+) is where there is both a finite T_c and the spin–glass state is controlled by the long–range part of the interaction. The thick solid line separates the region of short–range behavior (SR) from that of long–range behavior and is denoted by $\sigma_c(d)$. The thick dashed line separates regions where $T_c = 0$ (e.g., LR^0) from regions where $T_c > 0$, i.e. it corresponds to a zero stiffness exponent. The dark shaded region (MF) is where there is no thermodynamic limit unless the interactions are scaled appropriately by system size. The calculations are performed for $d = 1$ (marked by a horizontal dashed red line), for which $\sigma_c(d) = 2$ and the thermodynamic limit does not exist for $\sigma < 1/2$ (unless the interactions are scaled by a power of the system size). These values of σ are marked. (Figure adapted from Ref. [87])

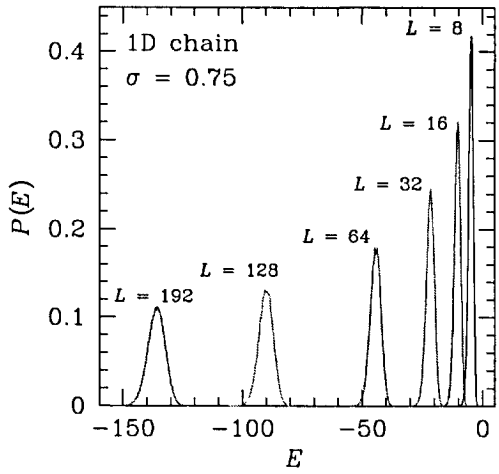

Figure 7.5: Unscaled energy distributions for several system sizes for the one–dimensional Ising chain with $\sigma = 0.75$ (LR^+ phase).

large. As reported in Ref. [88], the time to compute a ground–state instance using the parallel tempering Monte Carlo method scales with a power of the system size for $\sigma \lesssim 1.25$, whereas for large values of σ the time to compute a ground state scales $\sim \exp(aL)$, with a a constant. In this case we use the BCP algorithm which performs best for short–range interactions, thus perfectly complementing the parallel tempering method. Details about the algorithms used and simulation parameters can be found in Ref. [106].

7.3.3 Results

For each system size we compute 10^5 ground–state realizations for system sizes up to $L = 192$ (see Table 7.1 for details). In Fig. 7.5 we show a representative set of the unscaled data for $\sigma = 0.75$ in the LR^+-phase for several system sizes. Data for other values of σ show a similar qualitative behavior. The data in Fig. 7.5 can be scaled according to Eq. (7.4). The result is displayed in Fig. 7.6. The data are clearly skewed, the tails indicating that the skewness depends on the system size. In Fig. 7.7 we show scaled data for the ground–state energy distributions for $\sigma = 0.00$ (SK limit, MF phase). The data also show a clear asymmetry, but the spread in the tails is noticeably smaller than for larger values of σ (see Figs. 7.6

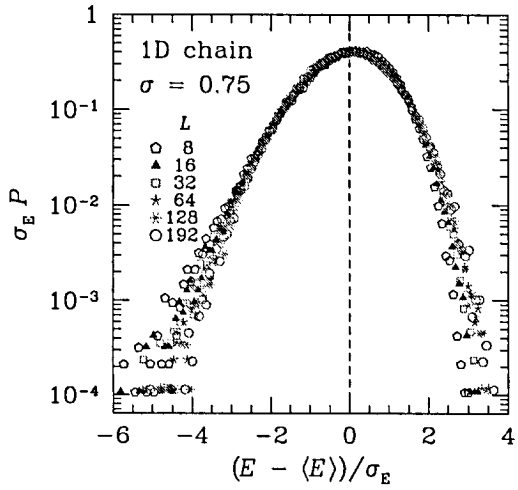

Figure 7.6: Scaled ground–state energy distributions for several system sizes for the one–dimensional Ising chain with $\sigma = 0.75$ (LR^+ phase). The dashed vertical line is a guide to the eye to illustrate the skewness of the distribution. The spread of the data in the tails suggests that the skewness changes with system size.

and 7.8) suggesting a smaller dependence of the skewness of the distribution on the system size.

In order to better quantify the aforementioned behavior, in Fig. 7.9 we present data for the skewness as a function of system size for several values of the power–law exponent σ. The data show that for $\sigma > 0.5$ the skewness of the ground–state energy distributions decays algebraically, $|\zeta_E| \sim L^\gamma$, with $\gamma \approx -0.5$ in the SR phase, whereas for $\sigma \leq 0.5$ (MF phase) the skewness is well fitted by Eq. (7.3) with $c_1 > 0$ thus tending to a constant in the thermodynamic limit. This means that the mean–field models present a singular behavior in which the ground–state energy fluctuations are non–Gaussian in the thermodynamic limit. This is not the case for the non–mean–field universality class where a limiting Gaussian behavior is obtained for $L \to \infty$. Note that $\gamma \approx -0.5$ for $\sigma > 1$ for which $T_c = 0$, in agreement with the results for the ladder system studied in Sec. 7.2.

We also study the size–dependence of the mean energy as a function of σ. For the mean–field Sherrington–Kirkpatrick model [97] ($\sigma = 0$) it is known that $\omega \sim 2/3$ [107, 81, 83, 82]. Our results agree well with this prediction, i.e. $\omega = 0.64(1)$ (the quality of fit probability [91] is $Q = 0.51$; the fit is performed for $L \geq 64$).

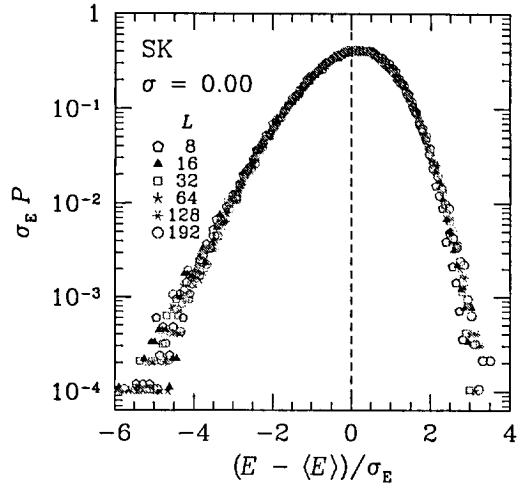

Figure 7.7: Scaled ground–state energy distributions for several system sizes for the one–dimensional Ising chain with $\sigma = 0.00$ (MF phase, SK model). The dashed vertical line is a guide to the eye to illustrate the skewness of the distribution. The data show little spread in the tails suggesting a weaker dependence on L than for larger values of σ.

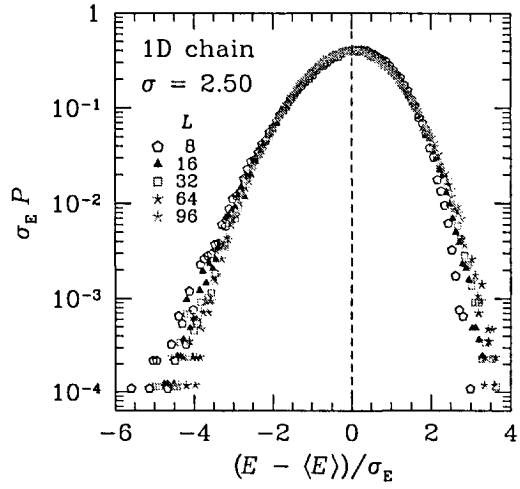

Figure 7.8: Scaled ground–state energy distributions for several system sizes for the one–dimensional Ising chain with $\sigma = 2.50$ (SR phase). The dashed vertical line is a guide to the eye to illustrate the skewness of the distribution. The data show a moderate dependence on the system size.

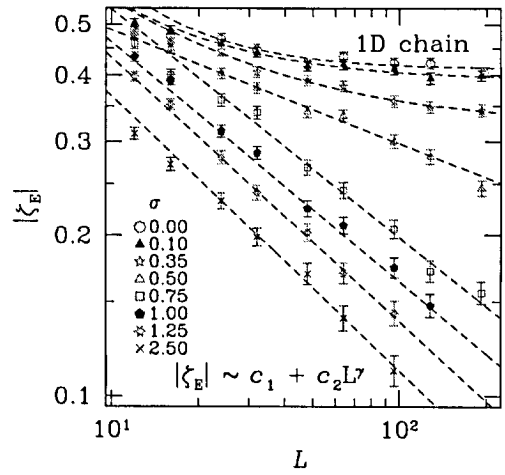

Figure 7.9: Skewness ζ_E as a function of system size L for several values of σ. For $\sigma < 0.5$ (MF phase) the data scale as $\zeta_E \sim c_1 + c_2 L^\gamma$ with $c_1 > 0$ [Eq. (7.3)] thus tending to a constant in the thermodynamic limit. For $\sigma \geq 0.5$ the skewness decays with a power–law behavior, i.e., $c_1 = 0$ (fits done for $L \geq 64$). Note that for $\sigma > 1$, for which $T_c = 0$, $\gamma \approx -0.5$ in agreement with the results for the ladder system presented in Sec. 7.2.

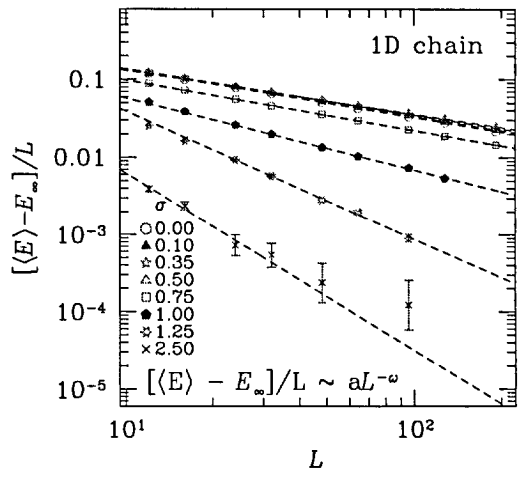

Figure 7.10: Mean $[\langle E\rangle - E_\infty]/L$ as a function of system size L for several values of σ. The data are expected to decay as a power of the system size with an exponent ω. Note that for the SK limit $\omega \approx 2/3$ in agreement with other predictions[107, 81, 83, 82]. [See Fig. 7.11 for $\omega(\sigma)$].

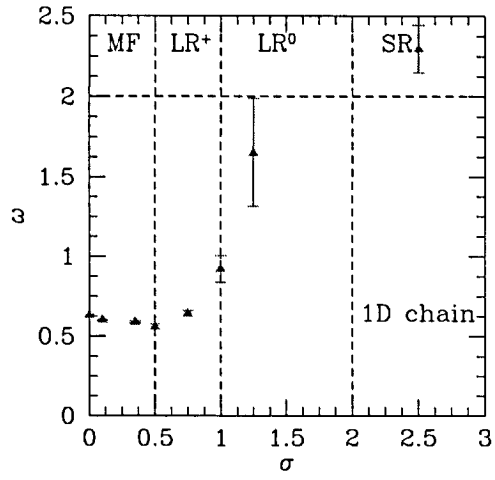

Figure 7.11: Exponent of the mean energy (ω) as a function of σ, according to Eq. (7.1). ω increases from the SK value ($\sim 2/3$) for increasing σ and saturates at $\omega \approx 2$ in the short–range phase (SR). The exponents are only estimated for the four largest system sizes studied for a given value of σ. See Tab. 7.1 for details. In this and following figures, the boundaries between the different universality classes are denoted by vertical dashed lines.

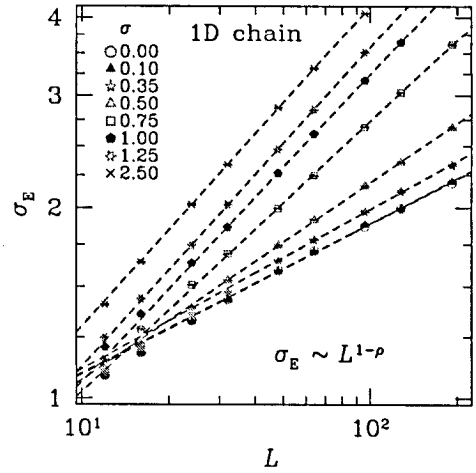

Figure 7.12: Standard deviation σ_E as a function of system size L for several values of σ. The data are expected to decay as a power of the system size with an exponent ρ. Note that for the SK limit $\rho \approx 3/4$ in agreement with other predictions [109, 81, 83]. [See Fig. 7.13 for $\rho(\sigma)$].

Unfortunately, there are no predictions for the different exponents for $\sigma > 0$, thus we will mainly compare the present results to data for the SK model. In Fig. 7.10 we show data for all values of σ studied. For increasing σ, ω increases rapidly and then saturates at $\omega \approx 2$. This behavior can be seen in details in Fig. 7.11 where we show the behavior of ω [see Eq. (7.1)] in detail for the different universality classes.

The behavior of the energy fluctuations is shown in Fig. 7.12 as a function of system size L for several values of σ. In the SK limit there are contradicting predictions regarding the power–law exponent ρ of the energy fluctuations σ_E. While Crisanti *et al.* [108] find $\rho = 5/6$, Bouchaud *et al.* [83] and Aspelmeier *et al.* [109] find $\rho = 3/4$. In this work we obtain $\rho = 0.775(2)$ ($Q = 0.58$; fits done for $L \geq 64$), which is also in agreement with the work by Palassini [81]. In Fig. 7.13 we show the σ-dependence of ρ. It is noteworthy that ρ decreases from the mean–field value $\sim 3/4$ to $1/2$ in the short–range universality class. This is to be expected as for $\sigma \to \infty$ the central limit theorem predicts that $\rho = 1/2$. Note that again the results found agree with the prediction of the short–range ladder system in Sec. 7.2.2.

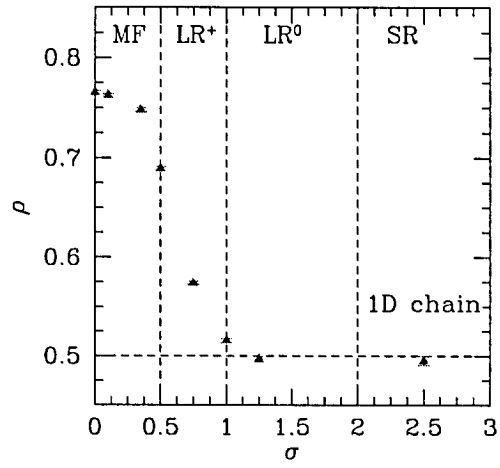

Figure 7.13: Exponent for the energy fluctuations ρ as a function of σ [see Eq. (7.2)]. For $\sigma \to 0$ $\rho \approx 3/4$ in agreement with Refs. [109], [83], and [81]. For $\sigma \to \infty$, $\rho \to 1/2$, as predicted by the central limit theorem, and in agreement with the results on the ladder system presented in Sec. 7.2.2.

7.3.4 Limiting distribution

In order to further strengthen the conjecture that ground–state energy distributions remain skewed in the thermodynamic limit for the mean–field phase, in this section we study the area deviation of the energy distributions in comparison to a Gaussian distribution $P_{\rm G}(E)$ "best fit." We define the area difference Δ via

$$\Delta = \int_E |P(E) - P_{\rm G}(E)| dE \,, \tag{7.17}$$

where $P(E)$ are the actual data. In Fig. 7.14 we show the area difference between the energy distributions and a Gaussian "best fit" as a function of system size L for several values of σ. The data for $\sigma < 0.5$ can be well fitted by a functional form $\sim a + b/L^c$, i.e., the area difference tends to a nonzero constant in the thermodynamic limit. This is not the case for $\sigma \geq 0.5$ where the area difference decays with a power–law of the system size therefore showing that the difference between the data and a Gaussian limiting distribution becomes smaller for increasing L.

Palassini [81] has fit the data for the scaled probability distribution functions of the SK model, Eq. (7.4), to a modified Gumbel distribution [94, 92, 93] $g_m(x)$

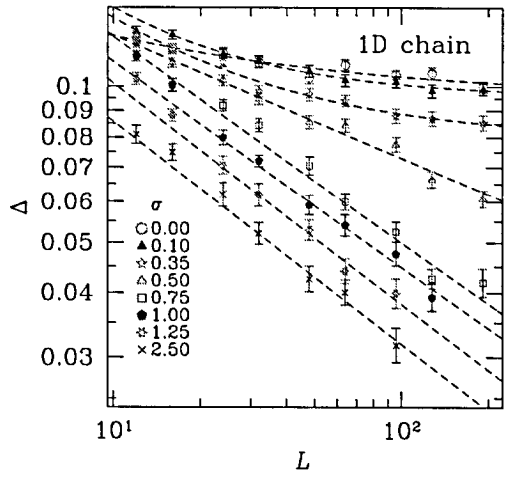

Figure 7.14: Difference in area between the actual data for the energy probability distributions of the one–dimensional Ising chain to a Gaussian limiting distribution as a function of system size L for several values of σ [see Eq. (7.17)]. In the MF phase ($\sigma < 0.5$) the area difference tends to a constant for increasing system size, whereas for $\sigma \geq 0.5$ the area difference decays with a power of the system size. Note the close resemblance to the behavior found for the skewness of the distribution, Fig. 7.9.

finding good agreement between the data and the fit. In addition, Palassini shows that the best fit seems to be obtained for $m = 6$. The choice of the modified Gumbel distribution is empirical, and its relation to the extreme value theory of independent random variables is very likely a coincidence. Furthermore we do not know of any a priori reason why the aforementioned value of m fits the data best. Because outside the MF universality class the limiting distribution functions seem to converge to a Gaussian distribution, we make the ansatz:

$$g'_{m,m_2}(x) = w' \exp\left[m_2 y^2\right] g_m(y) , \tag{7.18}$$

where

$$y = \frac{x - \mu}{\nu} \tag{7.19}$$

and

$$g_m(y) = w \exp\left[my - me^y\right] \tag{7.20}$$

is the modified Gumbel distribution [110]. Here μ plays the role of a mean, ν a standard deviation, and w and w' are normalization factors. We can fix $m = 6$ and study the behavior of the coefficient m_2 as a function of system size for different values of σ. Note that $g'_{m,0}(x) = g_m(x)$. In Fig. 7.15 we show data for m_2 vs L for a few representative values of σ. Our results show that for $\sigma = 0.0$ (SK model) $m_2 \to 0$ for $\sigma \to \infty$. For $0 < \sigma \leq 0.5$ the limiting distribution is non–Gaussian, yet m_2 is small, but finite. For $\sigma > 0.5$ the Gaussian contribution via m_2 dominates in the thermodynamic limit, as can be seen in Fig. 7.15. This shows that only the energy distributions in the SK model can be fitted in the thermodynamic limit by a modified Gumbel distribution with $m = 6$. For all other values of $\sigma < 0.5$ there are Gaussian corrections to the Gumbel distribution, whereas for $\sigma \geq 0.5$ the data in the thermodynamic limit are well described by a Gaussian limiting distribution. This could be due to the fact that there are no length–scales associated with the mean–field model. Thus any length–scale associated effects will scale with the system size. This is not the case in the short–range models where a length–scale will not necessarily scale with the system size, therefore yielding a Gaussian distribution in the thermodynamic limit.

7.3.5 Finite temperatures

We want to test if the fact that the ground–state energy distribution of the SK model is skewed in the thermodynamic limit is a unique property of the

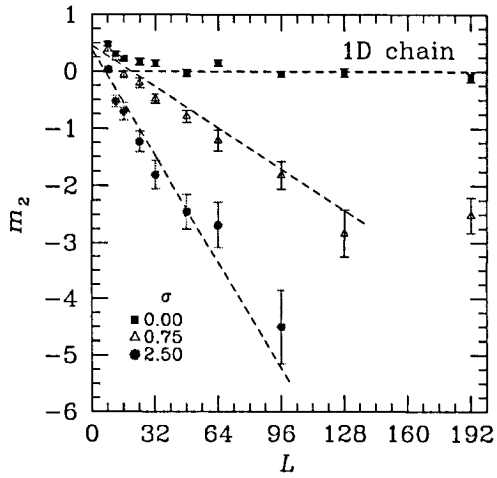

Figure 7.15: Coefficient m_2 to the quadratic term in the modified Gumbel distribution with $m = 6$, Eq. (7.18), as a function of system size for several values of the power–law exponent σ. The data show that m_2 vanishes for the SK limit in the thermodynamic limit thus suggesting that the energy distributions of the SK model are well described by a modified Gumbel function in agreement with results from Ref. [81]. For all $\sigma > 0$ m_2 tends to a nonzero negative value in the thermodynamic limit. For large values of σ, m_2 dominates thus showing that in the SR universality class the limiting probability distribution is well described by a Gaussian. The lines are guides to the eye.

ground state, or if similar effects can be observed at finite temperatures. Because the parallel tempering Monte Carlo method used to compute the ground–state energies of the one–dimensional Ising chain at small values of σ requires the system to be simulated at several temperatures ranging to values well above the spin–glass transition (for the SK model $T_c = 1$), we have also studied the behavior of the internal energy distributions in the mean–field limit as a function of temperature. The internal energy U for a given disorder realization $\{J_{ij}\}$ is given by

$$U = \frac{1}{L} \left\langle H_{\{J_{ij}\},\{S_i\}} \right\rangle \ , \tag{7.21}$$

where the Hamiltonian H is given by Eq. (7.10). Here $\langle \cdots \rangle$ represents a thermal average over t_{eq} Monte Carlo steps which we perform after equilibrating the system for a time t_{eq} (see Tab. 7.1 for details).

Figure 7.16 shows data for the skewness of the internal energy distributions as a function of the system size for several temperatures ranging from the ground–state to well above the critical temperature. The results show that the skewness of the distributions tend to a constant value in the thermodynamic limit for $T \leq T_c$ (curved fitting functions in a log–log plot, Fig. 7.16) thus showing that skewed energy distributions seem to persist for any temperature below the critical temperature. For temperatures above the critical temperature, the skewness shows again a power–law behavior thus suggesting that for $T > T_c$ the limiting distribution is Gaussian, as one would naively expect. Therefore, the limiting probability distribution is a modified Gumbel distribution for all temperatures below the critical point.

The inset of Fig. 7.16 shows the skewness of the probability distribution function of the internal energy of the SK model for $L = 192$ as a function of temperature. The data show a peak around $T_c = 1$. We expect the functional form of the skewness to remain approximatively the same for $L \to \infty$ when $T < T_c$, whereas for $T > T_c$ we expect for the skewness $\zeta_E \to 0$ in the thermodynamic limit. It would be interesting to understand the origins of this behavior of the mean–field model analytically.

For nonzero values of σ we find finite–temperate results in agreement with the data presented in Sec. 7.3.3: the distributions become Gaussian in the thermodynamic limit.

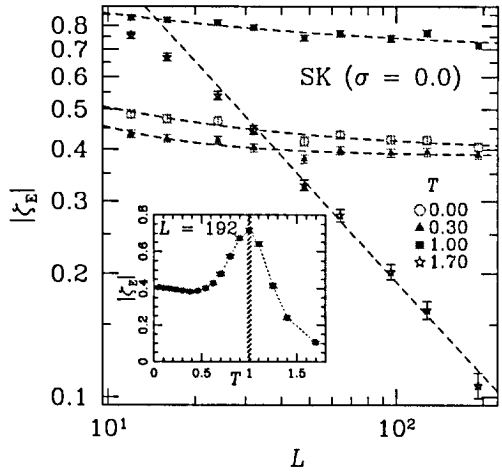

Figure 7.16: Skewness of the internal energy probability distribution functions of the SK model as a function of system size for different temperatures. The data show a curvature for $T \leq T_c$ in a log–log scale thus suggesting that the skewness converges to a constant value in the thermodynamic limit. For $T > T_c$ the skewness decays with a power of the system size (Gaussian limiting probability distribution function). The inset shows the skewness of the internal energy distribution of the SK model for $L = 192$ (largest system size studied) as a function of temperature. The data show that for finite system sizes the skewness seems to peak at the transition ($T_c = 1$).

7.4 Conclusion

We have studied in detail the probability distribution function of the ground–state energy of the one–dimensional Ising spin chain with random power–law interactions for several values of the power–law exponent σ. For the SK limit, when $\sigma = 0$, our results agree with previous numerical results by Palassini [81]. We find by studying different moments of the distribution, that the SK model has a skewed probability distribution function in the thermodynamic limit which is well described by a modified Gumbel distribution with $m = 6$. This behavior is not only valid for the ground–state energy, but for all energies below the critical temperature.

By varying the power–law exponent σ we scan several universality classes and show that for the non–mean–field regime when $\sigma > 0.5$ the probability distribution functions converge to a Gaussian distribution in the thermodynamic limit, in agreement with a short–range spin–glass ladder. Thus a skewed probability distribution function is a characteristic property of the mean–field spin–glass model. This behavior again poses the question, if the mean–field description of spin glasses is adequate for non–mean–field models.

σ	$8, 12, 16$	$24, 32$	$48, 64$	$96, 128$	192
0.00	2×10^3	4×10^3	8×10^3	4×10^4	12×10^4
0.10	2×10^3	4×10^3	8×10^3	4×10^4	12×10^4
0.35	2×10^3	4×10^3	8×10^3	4×10^4	12×10^4
0.50	2×10^3	4×10^3	8×10^3	4×10^4	12×10^4
0.75	2×10^3	4×10^3	8×10^3	4×10^4	12×10^4
1.00	2×10^3	4×10^3	8×10^3	8×10^4	6×10^5
1.25	2×10^3	4×10^3	6×10^4	6×10^5	
2.50	2×10^3	4×10^3	2×10^5		

Table 7.1: Parameters of the parallel tempering Monte Carlo simulations. The table shows the total number of Monte Carlo steps $t_{\rm eq}$ used for each value of σ and L. We use between 10 and 17 temperatures, depending on the system size, to ensure that the acceptance ratios of the parallel tempering moves are larger than ~ 0.30. The lowest temperature used is 0.50, the highest 1.70. For the internal energy distributions (Sec. 7.3.5) we compute thermally averaged values of the internal energy for a given disorder realization after equilibrating for $t_{\rm eq}$ Monte Carlo steps. The averages are done over $t_{\rm eq}$ Monte Carlo steps. For $\sigma = 2.50$ and $L = 96$ the calculations have been done using the BCP algorithm (see Ref. [106]).

Chapter 8

Outlook

In chapter 4 and chapter 5, we have applied the high–temperature series expansion to two problems related to the study of strongly–correlated electron systems. We found that for fermionic systems such as the t–t'–J model the temperatures that can be reached are only of moderate order and quantum Monte Carlo simulations with a sign problem as in Ref. [111] and exact diagonalizations [112] provide a much more detailed picture of the physical behavior of these systems and especially of the dynamical properties of the system. Furthermore we are often unable to resolve the low–temperature behavior unless the approximants are biased to a known functional low–temperature form. While lower temperatures can be reached for models with a simpler lattice graph such as the t–J model by computing the series to higher order, the computational effort quickly becomes prohibitive due to the exponential scaling of the algorithm with the system size. Here new algorithms mapping the imaginary time evolution of the system to a stochastic differential equation [113] seem to be a promising approach. Systems for which high–temperature series expansions remain more efficient than quantum Monte Carlo methods are frustrated magnets such as the J_1–J_2 model [114].

On the other hand the high–temperature expansion is a viable method if one is interested in the study of the static properties of a system as a function of the coupling constants. The high–temperature series can be calculated symbolically in the coupling constants so that different parameters can be quickly studied. Here a future subject of research would be the use of multivariable approximants such as partial differential approximants or multivariable Padé approximants [30] to make a more efficient use of the known expansion coefficients.

Bibliography

[1] J. G. Bednorz and Müller K. A. *Z. Phys. B*, 64, 1986.

[2] P. Dai, B. C. Chakoumakos, G. F. Sun, K. W. Wong, D. F. Lu, and Y. Xin. Synthesis and neutron powder diffraction study of the superconductor $HgBa_2Ca_2Cu_3O_{8+}$ by Tl substitution. *Physica C Superconductivity*, 243:201–206, February 1995.

[3] P. W. Anderson. The resonating valence bond state in La_2CuO_4 and superconductivity. *Science*, 235:1196–1198, March 1987.

[4] C. N. R. Rao, editor. *Chemistry of high temperature superconductors.* World Scientific Publishing, 1991.

[5] V. J. Emery. Theory of high-T_c superconductivity in oxides. *Phys. Rev. Lett.*, 58:2794–2797, June 1987.

[6] M. S. Hybertsen, E. B. Stechel, M. Schluter, and D. R. Jennison. Renormalization from density-functional theory to strong-coupling models for electronic states in CuO materials. *Phys. Rev. B*, 41:11068–11072, June 1990.

[7] F. C. Zhang and T. M. Rice. Effective Hamiltonian for the superconducting Cu oxides. *Phys. Rev. B*, 37:3759–3761, March 1988.

[8] E. Dagotto. Correlated electrons in high-temperature superconductors. *Rev. Mod. Phys.*, 66:763–840, July 1994.

[9] P. Fazekas. *Lectures on Electron Correlation and Magnetism.* World Scientific Publishing, 1999.

[10] E. Manousakis. The spin-1/2 Heisenberg antiferromagnet on a square lattice and its application to the cuprous oxides. *Rev. Mod. Phys.*, 63:1–62, January 1991.

[11] A. Damascelli, Z. Hussain, and Z. Shen. Angle-resolved photoemission studies of the cuprate superconductors. *Rev. Mod. Phys.*, 75:473–541, April 2003.

[12] T. Timusk and B. Statt. The pseudogap in high-temperature superconductors: an experimental survey . *Rep. Prog. Phys.*, 62:61–122, January 1999.

[13] M. P. Gelfand, R. R. P. Singh, and D. A. Huse. Perturbative Expansions for Quantum Many-Body Systems. *J. Stat. Phys.*, 59:1093, 1990.

[14] M. Imada, A. Fujimori, and Y. Tokura. Metal-insulator transitions. *Rev. Mod. Phys.*, 70:1039–1263, October 1998.

[15] N. Elstner, R. L. Glenister, R. R. P. Singh, and A. Sokol. Scaling regimes, crossovers, and lattice corrections in two-dimensional Heisenberg antiferromagnets. *Phys. Rev. B*, 51:8984–8995, April 1995.

[16] R. R. P. Singh and R. L. Glenister. Magnetic poperties of the lightly doped t-J model: A study through high-temperature expansions. *Phys. Rev. B*, 46:11871–11883, 1992.

[17] R. R. P. Singh and R. L. Glenister. Momentum distribution function for the two-dimensional t-J model. *Phys. Rev. B*, 46:14313–14316, December 1992.

[18] W. O. Putikka, M. U. Luchini, and T. M. Rice. Aspects of the phase diagram of the two-dimensional t-J model. *Phys. Rev. Lett.*, 68:538–541, January 1992.

[19] W. O. Putikka, M. U. Luchini, and M. Ogata. Ferromagnetism in the two-dimensional t-J model. *Phys. Rev. Lett.*, 69:2288–2291, October 1992.

[20] W. O. Putikka, R. L. Glenister, R. R. P. Singh, and H. Tsunetsugu. Indications of spin-charge separation in the two-dimensional t-J model. *Phys. Rev. Lett.*, 73:170–173, July 1994.

[21] W. O. Putikka, M. U. Luchini, and R. R. P. Singh. Violation of Luttinger's Theorem in the Two-Dimensional t-J Model. *Phys. Rev. Lett.*, 81:2966–2969, October 1998.

[22] W. O. Putikka and M. U. Luchini. Limits on phase separation for two-dimensional strongly correlated electrons. *Phys. Rev. B*, 62:1684–1687, July 2000.

[23] L. P. Pryadko, S. A. Kivelson, and O. Zachar. Incipient Order in the t-J Model at High Temperatures. *Phys. Rev. Lett.*, 92(6):067002–+, February 2004.

[24] C. Domb and M. S. Green. *Phase Transitions and Critical Phenomena*, volume 3. Academic Press, 1974.

[25] R. Diestel. *Graph Theory.* Springer Verlag, 2nd ed., 2000.

[26] K. Huang. *Statistical mechanics.* New York: Wiley, 2nd ed., 1987.

[27] Lars Ahlfors. *Complex Analysis.* McGraw-Hill, 3rd Ed., 1979.

[28] G. A. Baker and P. Graves-Morris. *Padé approximants*, volume 59 of *Encyclopedia of mathematics and its applications.* Cambridge University Press, 2nd edition, 1996.

[29] Jr. G. A. Baker. *Quntitative Theory of Critical Phenomena.* Academic Press, 1990.

[30] A. J. Guttmann. Asymptotic Analysis of Power-Series Expansions. In Domb, editor, *Phase Transition and Critical Phenomena*, volume 13, chapter 1, pages 1–234. Academic Press, 1989.

[31] Jr. G. A. Baker. Application of the Padé Approximant Method to the Investigation of Some Magnetic Properties of the Ising Model. *Phys. Rev.*, 124:768–774, 1961.

[32] S. L. Sondhi, S. M. Girvin, J. P. Carini, and D. Shahar. Continuous quantum phase transitions. *Rev. Mod. Phys.*, 69:315–333, January 1997.

[33] S. Sachdev. *Quantum Phase Transitions.* Cambridge University Press, 2000.

[34] S. Sachdev. Colloquium: Order and quantum phase transitions in the cuprate superconductors. *Rev. Mod. Phys.*, 75:913–932, July 2003.

[35] M. Vojta. Quantum phase transitions. *Rep. Prog. Phys.*, 66:2069–2110, December 2003.

[36] S. Sachdev. Quantum Criticality: Competing Ground States in Low Dimensions. *Science*, 288:475–480, April 2000.

[37] S. Chakravarty, B. I. Halperin, and D. R. Nelson. Low-temperature behavior of two-dimensional quantum antiferromagnets. *Phys. Rev. Lett.*, 60:1057–1060, March 1988.

[38] S. Chakravarty, B. I. Halperin, and D. R. Nelson. Two-dimensional quantum Heisenberg antiferromagnet at low temperatures. *Phys. Rev. B*, 39:2344–2371, February 1989.

[39] A. V. Chubukov, S. Sachdev, and J. Ye. Theory of two-dimensional quantum Heisenberg antiferromagnets with a nearby critical ground state. *Phys. Rev. B*, 49:11919–11961, May 1994.

[40] A. W. Sandvik and D. J. Scalapino. Order-Disorder Transition in a Two-Layer Quantum Antiferromagnet. *Phys. Rev. Lett.*, 72:2777–2780, 1994.

[41] A. W. Sandvik, A. V. Chubukov, and S. Sachdev. Quantum critical behavior in a two-layer antiferromagnet. *Phys. Rev. B*, 51:16483–16486, June 1995.

[42] M. Troyer, M. Imada, and K. Ueda. *J. Phys. Soc. Jpn.*, 66:2957, 1997.

[43] Z. Weihong. Various series expansions for the bilayer $S = 1/2$ Heisenberg antiferromagnet. *Phys. Rev. B*, 55:12267–12275, May 1997.

[44] N. Elstner and R. R. P. Singh. Strong-coupling expansions at finite temperatures: Application to quantum disordered and quantum critical phases. *Phys. Rev. B*, 57:7740–7748, April 1998.

[45] P. V. Shevchenko, A. W. Sandvik, and O. P. Sushkov. Double-layer Heisenberg antiferromagnet at finite temperature: Brueckner theory and Quantum Monte Carlo simulations. *Phys. Rev. B*, 61:3475–3487, 2000.

[46] S. Sachdev, C. Buragohain, and M. Vojta. Quantum Impurity in a Nearly Critical Two-Dimensional Antiferromagnet. *Science*, 286:2479–2482, December 1999.

[47] S. Sachdev, M. Troyer, and M. Vojta. Spin Orthogonality Catastrophe in Two-Dimensional Antiferromagnets and Superconductors. *Phys. Rev. Lett.*, 86:2617–2620, March 2001.

[48] M. Vojta, C. Buragohain, and S. Sachdev. Quantum impurity dynamics in two-dimensional antiferromagnets and superconductors. *Phys. Rev. B*, 61:15152–15184, June 2000.

[49] S. Sachdev and M. Vojta. Quantum impurity in an antiferromagnet: Nonlinear sigma model theory. *Phys. Rev. B*, 68:064419, 2003.

[50] K. H. Höglund and A. W. Sandvik. Susceptibility of the 2D Spin-1/2 Heisenberg Antiferromagnet with an Impurity. *Phys. Rev. Lett.*, 91:077204, 2003.

[51] O. P. Sushkov. Spin-1/2 magnetic impurity in a two-dimensional magnetic system close to a quantum critical point. *Phys. Rev. B*, 62:12135–12140, November 2000.

[52] P. W. Anderson. Experimental constraints on the theory of high-T_c superconductivity. *Science*, 256:1526–1531, June 1992.

[53] C. Honerkamp, M. Salmhofer, N. Furukawa, and T. M. Rice. Breakdown of the Landau-Fermi liquid in two dimensions due to umklapp scattering. *Phys. Rev. B*, 63(3):035109–+, January 2001.

[54] S. Sorella, G. B. Martins, F. Becca, C. Gazza, L. Capriotti, A. Parola, and E. Dagotto. Superconductivity in the Two-Dimensional t-J Model. *Phys. Rev. Lett.*, 88(11):117002–+, March 2002.

[55] T. K. Lee, C. T. Shih, Y. C. Chen, and H. Q. Lin. Comment on "Superconductivity in the Two-Dimensional t-J Model". *Phys. Rev. Lett.*, 89(26):A269702+, December 2002.

[56] S. Sorella, A. Parola, F. Becca, L. Capriotti, C. Gazza, E. Dagotto, and G. Martins. Sorella *et al.* Reply:. *Phys. Rev. Lett.*, 89(26):A269703+, December 2002.

[57] W. Stephan and P. Horsch. Fermi surface and dynamics of the t-J model at moderate doping. *Phys. Rev. Lett.*, 66:2258–2261, April 1991.

[58] M. Randeria, H. Ding, J.-C. Campuzano, A. Bellman, G. Jennings, T. Yokoya, T. Takahashi, H. Katayama-Yoshida, T. Mochiku, and K. Kadowaki. Momentum Distribution Sum Rule for Angle-Resolved Photoemission. *Phys. Rev. Lett.*, 74:4951–4954, June 1995.

[59] E. Dagotto, A. Nazarenko, and M. Boninsegni. Flat quasiparticle dispersion in the 2D t-J model. *Phys. Rev. Lett.*, 73:728–731, August 1994.

[60] R. Putz, R. Preuss, A. Muramatsu, and W. Hanke. Conserving approximation for the three-band Hubbard model: Flat quasiparticle dispersion. *Phys. Rev. B*, 53:5133–5136, March 1996.

[61] N. Metropolis, A. W. Rosenbluth, M. N. Rosenbluth, A. H. Teller, and E. Teller. Equation of State Calculations by Fast Computing Machines. *J. Chem. Phys.*, 21:1087–1092, 1953.

[62] R. H. Swendsen and J. Wang. Nonuniversal critical dynamics in Monte Carlo simulations. *Phys. Rev. Lett.*, 58:86–88, January 1987.

[63] H. G. Evertz, G. Lana, and M. Marcu. Cluster algorithm for vertex models. *Phys. Rev. Lett.*, 70:875–879, February 1993.

[64] B. A. Berg and T. Neuhaus. Multicanonical ensemble: A new approach to simulate first-order phase transitions. *Phys. Rev. Lett.*, 68:9–12, January 1992.

[65] B. A. Berg. Introduction to Multicanonical Monte Carlo Simulations. *ArXiv Condensed Matter e-prints*, September 1999.

[66] F. Wang and D. P. Landau. Efficient, Multiple-Range Random Walk Algorithm to Calculate the Density of States. *Phys. Rev. Lett.*, 86:2050–2053, March 2001.

[67] F. Wang and D. P. Landau. Determining the density of states for classical statistical models: A random walk algorithm to produce a flat histogram. *Phys. Rev. E*, 64(5):056101–+, November 2001.

[68] C. Yamaguchi and N. Kawashima. Combination of improved multibondic method and the Wang-Landau method. *Phys. Rev. E*, 65(5):056710–+, May 2002.

[69] S. Reynal and H. Diep. Simulation of Spin Models in Multicanonical Ensemble with Collective Updates. *ArXiv Condensed Matter e-prints*, September 2004.

[70] Matthias Troyer, Stefan Wessel, and Fabien Alet. Flat Histogram Methods for Quantum Systems: Algorithms to Overcome Tunneling Problems and Calculate the Free Energy. *Phys. Rev. Lett.*, 90:120201–+, 2003.

[71] W. Janke and S. Kappler. Multibondic Cluster Algorithm for Monte Carlo Simulations of First-Order Phase Transitions. *Phys. Rev. Lett.*, 74:212–215, January 1995.

[72] F. Y. Wu. The Potts model. *Rev. Mod. Phys.*, 54:235–268, January 1982.

[73] O. Narayan and A. P. Young. Convergence of Monte Carlo simulations to equilibrium. *Phys. Rev. E*, 64(2):021104–+, August 2001.

[74] A. M. Ferrenberg, D. P. Landau, and R. H. Swendsen. Statistical errors in histogram reweighting. *Phys. Rev. E*, 51:5092–5100, May 1995.

[75] U. Wolff. Collective Monte Carlo updating for spin systems. *Phys. Rev. Lett.*, 62:361–364, January 1989.

[76] C. Zhou and R. N. Bhatt. Understanding and Improving the Wang-Landau Algorithm. *ArXiv Condensed Matter e-prints*, June 2003.

[77] P. Dayal, S. Trebst, S. Wessel, D. Würtz, M. Troyer, S. Sabhapandit, and S. N. Coppersmith. Performance Limitations of Flat-Histogram Methods. *Phys. Rev. Lett.*, 92(9):097201–+, March 2004.

[78] Y. Wu, M. Koerner, L. Colonna-Romano, S. Trebst, H. Gould, J. Machta, and M. Troyer. Overcoming the critical slowing down of flat-histogram Monte Carlo simulations: Cluster updates and optimized broad-histogram ensembles. *ArXiv Condensed Matter e-prints*, December 2004.

[79] A. W. Sandvik. Stochastic series expansion method with operator-loop update. *Phys. Rev. B*, 59:R14157, 1999.

[80] S. Trebst, D. A. Huse, and M. Troyer. Optimizing the ensemble for equilibration in broad-histogram Monte Carlo simulations. *Phys. Rev. E*, 70(4):046701–+, October 2004.

[81] Palassini. Ground-state energy fluctuations in the Sherrington-Kirkpatrick model. 2003. (cond-mat/0307713).

[82] A. Andreanov, F. Barbieri, and O. C. Martin. Large deviations in spin-glass ground-state energies. *European Physical Journal B*, 41:365, 2004.

[83] J.-P. Bouchaud, F. Krzakala, and O. C. Martin. Energy exponents and corrections to scaling in Ising spin glasses. *Phys. Rev. B*, 68:224404, 2003.

[84] A. J. Bray, M. A. Moore, and A. P Young. Lower critical dimension of metallic vector spin-glasses. *Phys. Rev. Lett*, 56:2641, 1986.

[85] D. S. Fisher and D. A. Huse. Equilibrium behavior of the spin-glass ordered phase. *Phys. Rev. B*, 38:386, 1988.

[86] L. Leuzzi. Critical behaviour and ultrametricity of ising spin-glass with long-range interactions. *J. Phys. A*, 32:1417, 1999.

[87] H. G. Katzgraber and A. P. Young. Monte Carlo studies of the one-dimensional Ising spin glass with power-law interactions. *Phys. Rev. B*, 67:134410, 2003.

[88] H. G. Katzgraber and A. P. Young. Geometry of large-scale low-energy excitations in the one-dimensional Ising spin glass with power-law interactions. *Phys. Rev. B*, 68:224408, 2003.

[89] J. M. Kim, M. A. Moore, and A. J. Bray. Zero-temperature directed polymers in a random potential. *Phys. Rev. A*, 44:2345, 1991.

[90] T. Halpin-Healy. Directed polymers in random media: Probability distributions. *Phys. Rev. A*, 44:3415, 1991.

[91] W. H. Press, S. A. Teukolsky, W. T. Vetterling, and B. P. Flannery. *Numerical Recipes in C.* Cambridge University Press, Cambridge, 1995.

[92] S. T. Bramwell, J.-Y. Fortin, P. C. Holdsworth, S. Peysson, J.-F. Pinton, B. Portelli, and M. Sellitto. Magnetic fluctuations in the classical XY

model: The origin of an exponential tail in a complex system. *Phys. Rev. E*, 63:041106, 2001.

[93] B. Portelli, P. C. W. Holdsworth, M. Sellitto, and S. T. Bramwell. Universal magnetic fluctuations with a field-induced length scale. *Phys. Rev. E*, 64:036111, 2001.

[94] E. J. Gumbel. *Large deviations techniques in decision, simulation, and estimation.* John Wiley and Sons, New York, 1958.

[95] I. Morgenstern and K. Binder. Magnetic correlations in two-dimensional spin-glasses. *Phys. Rev. B*, 22:288, 1980.

[96] Y. Ozeki. Ground State Properties of the $\pm J$ Ising Model in Two Dimensions. *J. Phys. Soc. Jpn.*, 59:3531, 1990.

[97] D. Sherrington and S. Kirkpatrick. Solvable model of a spin glass. *Phys. Rev. Lett.*, 35:1792, 1975.

[98] A. J. Bray and M. A. Moore. Lower critical dimension of Ising spin glasses: a numerical study. *J. Phys. C*, 17:L463, 1984.

[99] W. L. McMillan. Domain-wall renormalization-group study of the three-dimensional random Ising model. *Phys. Rev. B*, 30:476, 1984.

[100] W. L. McMillan. Domain-wall renormalization-group study of the two-dimensional random Ising model. *Phys. Rev. B*, 29:4026, 1984.

[101] N. Kawashima and A. P. Young. Phase transition in the three-dimensional $\pm J$ Ising spin glass. *Phys. Rev. B*, 53:R484, 1996.

[102] H. G. Ballesteros, A. Cruz, L. A. Fernandez, V. Martin-Mayor, J. Pech, J. J. Ruiz-Lorenzo, A. Tarancon, P. Tellez, C. L. Ullod, and C. Ungil. Critical behavior of the three-dimensional Ising spin glass. *Phys. Rev. B*, 62:14237, 2000.

[103] K. Hukushima and K. Nemoto. Exchange Monte Carlo method and application to spin glass simulations. *J. Phys. Soc. Jpn.*, 65:1604, 1996.

[104] E. Marinari, G. Parisi, J. J. Ruiz-Lorenzo, and F. Ritort. Numerical evidence for spontaneously broken replica symmetry in 3d spin glasses. *Phys. Rev. Lett.*, 76:843, 1996.

[105] J. J. Moreno, H. G. Katzgraber, and A. K. Hartmann. Finding low-temperature states with parallel tempering, simulated annealing and simple Monte Carlo. *Int. J. Mod. Phys. C*, 14:285, 2003.

[106] H. G. Katzgraber, M. Körner, F. Liers, and A. K. Hartmann. Energy fluctuations in spin glasses. *to be published*, 2005.

[107] S. Boettcher. Numerical results for ground states of spin glasses on Bethe lattices. *Eur. Phys. J. B*, 31:29, 2003.

[108] A. Crisanti, G. Paladin, and H.-J. S. A. Vulpiani. Replica trick and fluctuations in disordered systems. *Journal de Physique I*, 2:1325–1332, 1992.

[109] T. Aspelmeier, M. A. Moore, and A. P. Young. Interface energies in Ising spin glasses. *Phys. Rev. Lett.*, 90:127202, 2002.

[110] A. K. Hartmann. Sampling rare events: Statistics of local sequence alignments. *Phys. Rev. E*, 65:056102, 2002.

[111] R. Preuss, W. Hanke, C. Gröber, and H. G. Evertz. Pseudogaps and Their Interplay with Magnetic Excitations in the Doped 2D Hubbard Model. *Phys. Rev. Lett.*, 79:1122–1125, August 1997.

[112] T. Tohyama. Asymmetry of the electronic states in hole- and electron-doped cuprates: Exact diagonalization study of the t-t'-t''-J model. *Phys. Rev. B*, 70(17):174517–+, November 2004.

[113] J. F. Corney and P. D. Drummond. Gaussian Quantum Monte Carlo Methods for Fermions and Bosons. *Phys. Rev. Lett.*, 93(26):260401–+, December 2004.

[114] R. R. Singh, W. Zheng, J. Oitmaa, O. P. Sushkov, and C. J. Hamer. Symmetry Breaking in the Collinear Phase of the J_1-J_2 Heisenberg Model. *Phys. Rev. Lett.*, 91(1):017201–+, June 2003.

[115] M. P. Gelfand, R. R. P. Singh, and D. A. Huse. Zero-temperature ordering in two-dimensional frustrated quantum Heisenberg antiferromagnets. *Phys. Rev. B*, 40:10801–10809, December 1989.

[116] P. Chandra, P. Coleman, and A. I. Larkin. Ising transition in frustrated Heisenberg models. *Physical Review Letters*, 64:88–91, January 1990.

[117] G. Misguich, B. Bernu, and L. Pierre. Determination of the exchange energies in Li_2VOSiO_4 from a high-temperature series analysis of the square-lattice J_1-J_2 Heisenberg model. *Phys. Rev. B*, 68(11):113409–+, September 2003.

[118] R. R. Singh, W. Zheng, J. Oitmaa, O. P. Sushkov, and C. J. Hamer. Symmetry Breaking in the Collinear Phase of the $J_1 - J_2$ Heisenberg Model. *Physical Review Letters*, 91(1):017201–+, June 2003.

Seite Leer /
Blank leaf

Appendix A

Frustrated quantum magnets

As we have seen in chapter 4 and chapter 5, it is either very difficult or impossible to obtain the same resolution with high–temperature series expansion as with quantum Monte Carlo simulations, even for systems with a sign problem such as the t–t'–J model. The simulation of strongly frustrated magnets on the other hand, such as the spin–1/2 square lattice $J_1 - J_2$ model, remains an area of application, where series expansions show considerable advantages over quantum Monte Carlo simulations.

The spin–1/2 square lattice $J_1 - J_2$ model is defined by the Hamiltonian

$$H_{J_1-J_2} = J_1 \sum_{\langle ij \rangle} \mathbf{S}_i \cdot \mathbf{S}_j + J_2 \sum_{\langle\langle ik \rangle\rangle} \mathbf{S}_i \cdot \mathbf{S}_k, \tag{A.1}$$

where the $\mathbf{S}_i$ are spin–1/2 operators on the sites of a square lattice and the sums are over nearest–neighbor sites $\langle ij \rangle$ and next–nearest neighbor sites $\langle\langle ik \rangle\rangle$ of the square lattice. For $J_2 = 0$ it corresponds to the square lattice Heisenberg antiferromagnet. As J_2 is increased, the strength of the quantum fluctuations in the system increases due to the frustration induced by the next–nearest neighbor coupling and the antiferromagnetic order vanishes. For large values of J_2 the system orders in a collinear phase [115, 116]. The model is relevant for materials such as Li_2VOSiO_4 [117], but is difficult to treat numerically due to a strong sign problem in the region of the phase transition from antiferromagnetic order to collinear order at $J_1/J_2 \approx 1/2$. Furthermore symmetry arguments predict the collinear phase to have a finite temperature phase transition of the Ising

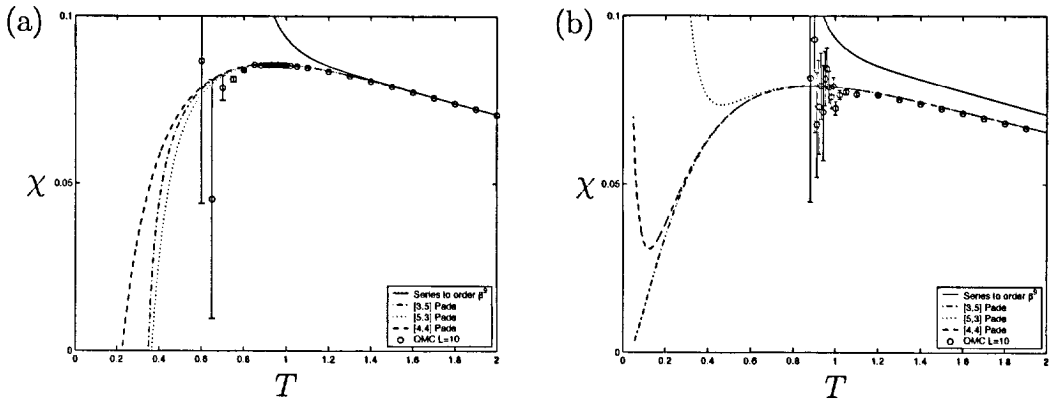

Figure A.1: The uniform susceptibility χ of the $J_1 - J_2$ model for $J_2 = 1$ and $J_1 = 1/4$ (a) and $J_1 = 1/2$ (b).

type as the collinear phase breaks a discrete symmetry, which in this case is the rotational symmetry. Yet this phase transition has not been observed in numerical experiments [118].

Here we briefly report the calculation of the uniform susceptibility of the $J_1 - J_2$ model to 8th–order with a high temperature series expansion. The connected clusters are the same as the clusters for the t–t'–J model discussed in chapter 5. For each cluster the uniform susceptibility was calculated and the weights were constructed with the help of the computer algebra program `Mathematica`. The series was analyzed using Padé approximants and the results and a comparison with results obtained from quantum Monte Carlo simulations are shown in Fig. A.1.

While the high–temperature series expansion can access the region below $T = 1$, the quantum Monte Carlo simulations break down at $T \approx 1$, especially for the strongly frustrated case ($J_1/J_2 = 1/2$) shown in (b). Additionally we examined the specific heat and the uniform susceptibility for signs of a finite temperature phase transition, but no such transition could be detected with a series of order 8.

Curriculum Vitae

Name, First Name:	Körner, Mathias
Date of Birth:	January 15th, 1974 in Dudweiler, Germany
Nationality:	German

1980 – 1984:	Grundschule (primary school) in Homburg–Jägersburg, Germany.
1984 – 1993:	Gymnasium Johanneum (high school) in Homburg, Germany.
1993:	Abitur.
July 1993 – July 1994:	Military service.
Oct. 1994 – Mar. 1999:	Undergraduate studies in physics at ETH Zürich.
Oct. 1996 – May 1997:	Exchange year at Kings College London, UK.
Nov. 1998 – May 1999:	Diploma thesis in theoretical physics on "Shot Noise in Percolation Networks" under the supervision of Prof. G. Blatter at the Institute of Theoretical Physics at ETH Zürich.
May 1999:	Diploma in theoretical physics with distinction.
May 1999 – Sep. 1999:	Work at Inalp networks in Niederwangen, Switzerland as a developer and person responsible for trademark and patent applications.
Sep. 1999 – May 2005:	Graduate studies at the Institute of Theoretical Physics at ETH Zürich under the supervision of Prof. M. Troyer.

Acknowledgements

First and foremost, I would like to express my deep gratitude to my supervisor Matthias Troyer. He gave me the opportunity to do this work as his first PhD student, and his constant support and knowledge helped me considerably during this research project. I also thank Gianni Blatter for being my pro–forma supervisor for the first year of this thesis while allowing me to work with Matthias Troyer, and Manfred Sigrist for being the co–examiner of this thesis and his dedication to helping me finish this thesis.

In connection with my research on the t–J model I greatly profited from the discussions with Maurice Rice and Carsten Honerkamp at the Intitute of Theoretical Physics, and from the discussions and email exchanges with Rajiv Singh, Steven Kivelson, Leonid Pryadko, and Bill Putikka. I also thank Pascal Bünzli for the good work he performed as a Diploma student under my — often imperfect — supervision.

Furthermore I thank Helmut Katzgraber for supporting my interest in spin glasses and Monte Carlo simulations and the many discussions and arguments originating in this research. The work we did in collaboration with Alexander Hartmann and Frauke Liers was fun and enlightening. Other collaborators that I would like to thank are Yong Wu, Luis Colonna–Romano, Jon Machta, Simon Trebst, and especially Harvey Gould, who managed seven authors on a paper.

Special thanks go to Naoki Kawashima for offering me a place to stay in Tokyo, and George Sigut, the system administrator of the Asgard and Hreidar clusters at ETHZ. It was always a great pleasure and delight to work with him, no matter what part of the fileserver crashed or what part of my data I deleted. I also

thank all members of the Institute of Theoretical Physics for making the institute a place as nice and pleasant as it is. Among the many people that I'd like to mention are Hans Peter Büchler, Andreas Läuchli, Synge Todo, Arno Candel, Jérôme Koopmann, Samuel Wehrli, Igor Milat, Alvise de Col, Alban Fauchere, Rolf Heeb, Malek Bou-Diab, Diethelm Würtz, Fabien Alet, Sebastian Huber, Fabian Hassler, Philippe Corboz, Simon Trebst, and Prakash Dayal, with apologies to everyone that I forgot on this list. In addition I always enyojed the lunch and coffee discussions with Dominic Rau, Gerald Wigger, René Monnier, Jorge Gavilano, and other people of the Ott group.

Last but not least I thank my parents for their love and endless support and my friends for their support and the good and bad times we had during the time of this thesis. In particular I want to thank Ueli Teuscher for pushing me at the right time.